ANL-7527

Argonne National Laboratory

REACTOR DEVELOPMENT PROGRAM PROGRESS REPORT

December 1968

The facilities of Argonne National Laboratory are owned by the United States Government. Under the terms of a contract (W-31-109-Eng-38) between the U. S. Atomic Energy Commission, Argonne Universities Association and The University of Chicago, the University employs the staff and operates the Laboratory in accordance with policies and programs formulated, approved and reviewed by the Association.

MEMBERS OF ARGONNE UNIVERSITIES ASSOCIATION

The University of Arizona
Carnegie-Mellon University
Case Western Reserve University
The University of Chicago
University of Cincinnati
Illinois Institute of Technology
University of Illinois
Indiana University
Iowa State University
The University of Iowa
Kansas State University
The University of Kansas
Loyola University
Marquette University
Michigan State University
The University of Michigan
University of Minnesota
University of Missouri
Northwestern University
University of Notre Dame
The Ohio State University
Ohio University
The Pennsylvania State University
Purdue University
Saint Louis University
Southern Illinois University
University of Texas
Washington University
Wayne State University
The University of Wisconsin

Printed in the United States of America
Available from
Clearinghouse for Federal Scientific and Technical Information
National Bureau of Standards, U. S. Department of Commerce
Springfield, Virginia 22151
Price: Printed Copy $3.00; Microfiche $0.65

ANL-7527
Reactor Technology

ARGONNE NATIONAL LABORATORY
9700 South Cass Avenue
Argonne, Illinois 60439

REACTOR DEVELOPMENT PROGRAM PROGRESS REPORT

December 1968

Robert B. Duffield, Laboratory Director
Stephen Lawroski, Associate Laboratory Director

Division	Director
Chemical Engineering	R. C. Vogel
EBR-II Project	M. Levenson
Metallurgy	M. V. Nevitt
Reactor Engineering	L. J. Koch
Reactor Physics	R. Avery

Report coordinated by
L. B. Fosdick and A. Glassner

Issued January 29, 1969

FOREWORD

The Reactor Development Program Progress Report, issued monthly, is intended to be a means of reporting those items of significant technical progress which have occurred in both the specific reactor projects and the general engineering research and development programs. The report is organized in accordance with budget activities in a way which, it is hoped, gives the clearest, most logical overall view of progress. Since the intent is to report only items of significant progress, not all activities are reported each month. In order to issue this report as soon as possible after the end of the month editorial work must necessarily be limited. Also, since this is an informal progress report, the results and data presented should be understood to be preliminary and subject to change unless otherwise stated.

The issuance of these reports is not intended to constitute publication in any sense of the word. Final results either will be submitted for publication in regular professional journals or will be published in the form of ANL topical reports.

The last six reports issued in this series are:

June 1968	ANL-7460
July 1968	ANL-7478
August 1968	ANL-7487
September 1968	ANL-7500
October 1968	ANL-7513
November 1968	ANL-7518

REACTOR DEVELOPMENT PROGRAM

Highlights of Project Activities for December 1968

EBR-II

The reactor was operated for 1188 MWd during December and had accumulated 22,666 MWd by the end of the month. All runs during December were at 50 MWt. The performance of the fission-product monitoring systems of the reactor was checked by inserting a control rod containing two bare Mark-IA fuel pins into the reactor and measuring the change in signals resulting from the insertion.

The acceptance rate for vendor-produced Mark-IA fuel elements increased from an original rate of less than 75% to a current rate of about 90% after the vendor instituted a postbonding step. A total of 4097 elements were received from the vendor, of which 3398 were acceptable. Four subassemblies containing vendor fuel have been fabricated, three of which are being irradiated in EBR-II as part of the vendor-fuel surveillance program.

During a "rehearsal test" of the instrumented subassembly in the reactor mockup at ANL-Illinois, all equipment and instrumentation functioned properly.

ZPR-3

The experimental program with Assembly 55, a null-reactivity experiment in which a $k_\infty = 1$ zone was used to determine the capture-to-fission ratio in ^{239}Pu, has been completed. Assembly 55A was identical with the preceding one except that a central region of 22% ^{240}Pu was incorporated in the $k_\infty = 1$ zone and measurements were made which may permit the evaluation of the capture-to-fission ratio for ^{240}Pu.

Assembly 56 was made critical near the end of the month with a loading of 374.1 kg of total plutonium. This assembly, the first of the FTR Resumed Phase-B Experiments, required an amount of fuel well below the 430-kg facility limit.

ZPPR

In-place tests of the radial perturbation-sample-drive mechanism and adjustments to the sample-changer mechanism have been made. Installation of the automated data-acquisition system and counting-room equipment is continuing.

ZPPR review of the qualifications of the operator and supervisor startup team has been completed.

ZPR-6 and -9

Conversion of the ZPR-6 and -9 facilities to plutonium operation continues with the contractor's installation of electrical wiring and controls for the cell-exhaust fan system and the reactor cooling system. It is expected that the contractor's work will be completed by the end of January.

TABLE OF CONTENTS

TABLE OF CONTENTS

TABLE OF CONTENTS

I. LIQUID METAL FAST BREEDER REACTORS--CIVILIAN

A. Fuel Development--LMFBR

1. Oxide

a. Fuel Studies

(i) Fuel Element Performance (L. A. Neimark, F. L. Brown, W. F. Murphy, and R. Natesh)

Last Reported: ANL-7518, pp. 1-3 (Nov 1968).

Preliminary analysis of axial fuel relocation in elements SOV-3, SOV-7, and HOV-15 indicates that the fuel columns increased in effective density below their midplanes. Elements SOV-3 and SOV-7 also showed increased densities above the midplane, whereas the center regions of these elements decreased in density. Of the three elements, the greatest increase in density below the midplane was found in HOV-15, which was the only element that showed a decrease in effective density in both the center and top regions. These observations are illustrated in Fig. I.A.1.

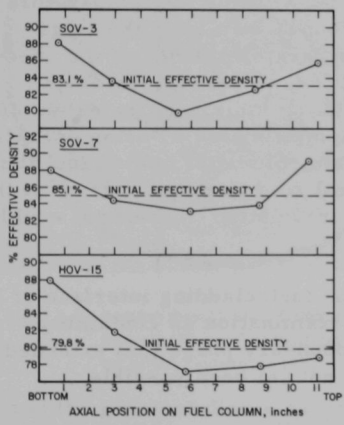

Fig. I.A.1. Changes in Effective Density along Oxide Fuel Columns Operated with Center Melting

The analysis of fuel relocation was made from metallographic sections along the length of each element. Initially, arbitrary densities of 96 and 93% of the theoretical fuel density were assigned to the columnar-grain and equiaxed-grain regions, respectively. Regions of nonsintered particles were assumed to have the as-fabricated smear density of the element. A mass balance of the resulting axial distribution of fuel indicated that the assumed densities for the various fuel regions were too high, probably because fuel cracking was not considered. More realistic values for the effective densities of relocated fuel were obtained by making the mass balance correspond to the original as-fabricated element density. This was accomplished by assuming the following percentages of theoretical density for each of the fuel regions:

Element	Columnar Grains (%)	Equiaxed Grains (%)
SOV-3	94	90
SOV-7	93	90
HOV-15	91	86

Measured changes in the centers of gravity of these elements are in qualitative agreement with the results of the relocation analysis. The center of gravity of SOV-3 shifted downward 0.03 in., that of SOV-7 shifted upward 0.03 in., and that of HOV-15 shifted downward 0.06 in. An increase in fuel density at the bottom of the elements can be attributed to fuel "slumping" as the fuel solidified from a molten condition. However, no reason is now offered for fuel relocating to the top of the elements.

Examination of the microstructures in HOV-15 appeared to indicate that fuel restructuring occurred after a molten structure was present in the center regions of the fuel. This molten structure, evidenced by large columnar grains that are free of gamma-emitting fission products but enhanced in alpha emitters, was clearly evident at the bottom of the element. However, at higher regions in the element, fine columnar grains were found growing into the large columnar-grain region next to the central void. At the axial midplane, restructuring was complete, and fine columnar grains extended completely from the outer periphery of the element to the central void. This restructuring was accompanied by the movement of some small particles of solid fission products and spherical voids up the temperature gradient; a concentration of these voids was found adjacent to the large central void. This restructuring tended to obliterate evidence of the once-molten region and made identification difficult. However, by using the general location of the solid fission products as an indicator, the extent of melting at all elevations in the element was approximated. During operation at the maximum rated power of the element, the volume of molten fuel thus obtained would likely completely fill the central void that was present at the end of the irradiation. Fuel slumping during irradiation, therefore, would not have occurred.

The white phase present at the fuel-cladding interface of SOV-3 has been identified by electron-probe examination as containing cesium; however, identification of the grain-boundary phase that extended 0.003 in. into the stainless steel cladding has not yet been possible.

2. Carbide

a. Fabrication and Evaluation

(i) Fuel Element Performance (L. A. Neimark and T. W. Latimer)

Last Reported: ANL-7518, p. 6 (Nov 1968).

The examinations of mixed-carbide fuel elements SMV-2, HMV-5, and NMV-11 following irradiation in EBR-II Subassembly XG05 to an estimated maximum burnup of 7.2 a/o are in progress. The design and operating parameters of these elements were reported previously (see Progress Report for October 1968, ANL-7513, Table I.A.1, p. 3). Visual examination has revealed a failure in NMV-11; the other two elements were intact.

For Element SMV-2, clad in Type 304 stainless steel, a maximum diametral increase of 2.1 mils or 0.73% occurred at 44% of the distance from the bottom to the top of the fueled section. The average percent diametral increases over 2.8-in. (20%) intervals along the length of the 14-in. fueled section were as follows:

0-2.8 in. (Bottom)	2.8-5.6 in.	5.6-8.4 in.	8.4-11.2 in.	11.2-14 in. (Top)
0.42	0.65	0.63	0.65	0.39

Fission-gas analysis from Element SMV-2 indicated a release of 15.8%. This amount approximates the 13.4% gas release found for the same type of fuel after irradiation to a burnup of 2.6 a/o (see Progress Report for April 1967, ANL-7329, p. 45). Figure I.A.2 shows an as-polished transverse section of SMV-2 taken at the midplane of the fueled section. As has been observed in the low-burnup carbide elements, the PuC particles swelled into adjacent void spaces between UC particles. The PuC particles appear to have reacted with the UC particles in the center 60% of the diameter of the transverse section. Outside this region there is evidence of PuC particles bonded to UC particles, but very little evidence of interdiffusion.

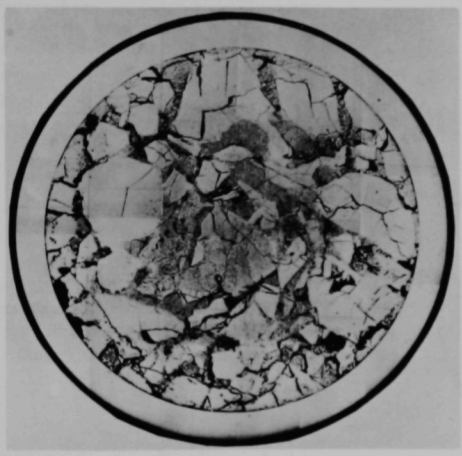

Fig. I.A.2. Section through SMV-2 Showing Reaction between UC and PuC Particles in the Center of the Element (~10X)

The maximum diametral increase of HMV-5 (clad in Hastelloy-X) was 5.1 mils or 1.7%, and the greatest diametral increases were found over the upper fuel region; the maximum increase occurred at 72% of the distance from the bottom to the top of the fuel. The average percent diametral increases over 2.8-in. (20%) intervals along the length of the 14-in. fueled section were as follows:

0-2.8 in. (Bottom)	2.8-5.6 in.	5.6-8.4 in.	8.4-11.2 in.	11.2-14 in. (Top)
0.30	0.72	1.26	1.62	0.37

Fission gases from this element have not yet been analyzed.

Only 1.5% of the calculated amount of fission gas generated in failed NMV-11 was recovered from the capsule. The gas recovered from the capsule plenum did not contain all of the helium fill-gas that was originally

in both the capsule and element plenums. Therefore, we suspect that all of the fission gas released from the fuel during irradiation was not collected by sampling the capsule plenum.

Figure I.A.3 shows an as-polished transverse section of NMV-11 taken at the midplane of the fueled section. Although some sintering appears to have occurred in the center of the element, the outlines of the original (U,Pu)C particles are clearly visible in the outer three-quarters of the radius. Because of a passivating technique (acids used during polishing to prevent quick oxidation of the surface), the microstructure in the large particles is evident. These particles contain $(U,Pu)_2C_3$ as a second phase. The dendritic appearance of this phase in the outer particles indicates no change in microstructure from the original rapidly cooled, arc-melted material.

Fig. I.A.3

Section through NMV-11 Showing Sintering in the Center of the Element. Cladding failure is shown at the bottom. Fine particles were lost from the periphery during specimen preparation. (~10X)

B. Physics Development--LMFBR

1. Theoretical Reactor Physics

a. General Fast Reactor Physics

(i) Multigroup Methods (H. H. Hummel)

Last Reported: ANL-7518, pp. 7-11 (Nov 1968).

(a) New Formulation of Broad-group Microscopic Cross Sections. The principles which have led to a new definition of the microscopic transport cross sections for use in fast breeder reactors* have been extended and used to derive a set of parallel definitions for the other microscopic cross sections. The definitions are based on the assumption that the logarithmic derivative of the transport collision density with respect to the concentration of the isotope of interest is constant over the energy range of any broad group considered in the collapsing operation.

A logical procedure analogous to that outlined by Travelli* leads to the following definitions for the most important cross sections used in the MC^2 code:**

$$\sigma_{tr_I}^{m,bg} = \frac{1}{\phi_I^{bg}} \sum_i^I \left\{ \left[2\left(\frac{\Sigma_{tr_I}^{bg}}{\Sigma_{tr_i}^{ufg}}\right)^2 - \left(\frac{\Sigma_{tr_I}^{bg}}{\Sigma_{tr_i}^{ufg}}\right) \right] \sigma_{tr_i}^{m,ufg} \phi_i^{ufg} \right\}; \quad (1)$$

$$\sigma_{t_I}^{m,bg} = \frac{1}{\phi_I^{bg}} \sum_i^I \left\{ \left[\sigma_{t_i}^{m,ufg} + \left(\Sigma_{t_I}^{bg} - \Sigma_{t_i}^{ufg}\right) \frac{\sigma_{tr_i}^{m,ufg}}{\Sigma_{tr_i}^{ufg}} \right] \phi_i^{ufg} \right\}; \quad (2)$$

$$(\nu\sigma_f)_I^{m,bg} = \frac{1}{\phi_I^{bg}} \sum_i^I \left\{ \left[(\nu\sigma_f)_i^{m,ufg} + \left(\nu\Sigma_{f_I}^{bg} - \nu\Sigma_{f_i}^{ufg}\right) \frac{\sigma_{tr_i}^{m,ufg}}{\Sigma_{tr_i}^{ufg}} \right] \phi_i^{ufg} \right\}; \quad (3)$$

$$\sigma_{so_{J\to I}}^{m,bg} = \frac{1}{\phi_J^{bg}} \sum_i^I \sum_j^J \left\{ \left[\sigma_{so_{j\to i}}^{m,ufg} + \left(\frac{\Sigma_{so_{J\to I}}^{bg}}{\Delta E_I} - \Sigma_{so_{j\to i}}^{ufg}\right) \frac{\sigma_{tr_j}^{m,ufg}}{\Sigma_{tr_j}^{ufg}} \right] \phi_j^{ufg} \right\}, \quad (4)$$

* Travelli, A., Trans. ANS 11, 532 (1968).

** Toppel, B. J., et al., ANL-7318 (1967).

where

ϕ_i^{ufg} = neutron flux in the ultrafine group i;

$\phi_I^{bg} \equiv \sum_i^I \phi_i^{ufg}$ = neutron flux in the broad group I;

$\Sigma_{tr_i}^{ufg}$ = macroscopic transport cross section over the ultrafine group i;

$\Sigma_{tr_I}^{bg} \equiv \dfrac{\phi_I^{bg}}{\sum_i^I \left(\dfrac{\phi_i^{ufg}}{\Sigma_{tr_i}^{ufg}}\right)}$ = macroscopic transport cross section over the broad group I;

$\Sigma_{t_i}^{ufg}$ = macroscopic total cross section over the ultrafine group i;

$\Sigma_{t_I}^{bg} \equiv \dfrac{1}{\phi_I^{bg}} \sum_i^I \left(\Sigma_{t_i}^{ufg} \phi_i^{ufg}\right)$ = macroscopic total cross section over the broad group I;

$(\nu\Sigma_f)_i^{ufg}$ = average number of neutrons emitted per fission times the microscopic fission cross section over the ultrafine group i;

$(\nu\Sigma_f)_I^{bg} = \dfrac{1}{\phi_I^{bg}} \sum_i^I \left[(\nu\Sigma_f)_i^{ufg} \phi_i^{ufg}\right]$ = average number of neutrons emitted per fission times the macroscopic fission cross section over the broad group I;

$\Sigma_{so_{j\to i}}^{ufg}$ = macroscopic scattering cross section from the ultrafine group j to the ultrafine group i per unit final energy;

$\Sigma_{so_{J\to I}}^{bg} \equiv \dfrac{1}{\phi_J^{bg}} \sum_i^I \sum_j^J \left(\Sigma_{so_{j\to I}}^{ufg} \phi_j^{ufg}\right)$ = macroscopic scattering cross section from the broad group J to the broad group I per unit final energy.

The symbols "σ" refer to the corresponding microscopic cross sections, related to the macroscopic cross section by the expression

$$\sigma^m = \frac{\partial \Sigma}{\partial N^m}, \tag{5}$$

with N^m the atomic concentration of the isotope m.

The definitions generally in use in cross-section collapsing codes for $\sigma_{t_I}^{m,bg}$, $(\nu\sigma_f)_I^{m,bg}$, and $\sigma_{so_{J\to I}}^{m,bg}$ can be obtained from Eqs. (2), (3), and (4), respectively, simply by letting $\sigma_{tr_j}^{m,ufg}$ vanish in the expressions. It can be shown, however, that the definitions obtained in this way can be derived from the assumption that the logarithmic derivative of the neutron flux with respect to the concentration of the isotope m be constant over the broad group I. Preliminary calculations have shown that this is a much poorer assumption than the assumption that has led to the new definitions, and that use of the traditional definitions leads to broad-group cross sections which satisfy Eq. (5) much less satisfactorily than the new set of definitions represented by Eqs. (1), (2), (3), and (4).

The improvement due to use of the new definitions is expected to be more noticeable for the transport cross section than for the other cross sections, because its traditional definition implies an assumption concerning the neutron current which is even less realistic. However, use of the improved definitions also for the other cross sections will be useful to calculate more accurate macroscopic broad-group sections for compositions other than the standard composition used in the MC^2 code. The calculation of distributed material worths should also be improved by using the new definitions.

2. Experimental Reactor Physics

a. Fast Critical Experiments--Experimental Support (Idaho) (W. G. Davey)

Last Reported: ANL-7518, pp. 12-13 (Nov 1968).

(i) Neutron Spectrometry. The data from the repeat of the proton-recoil spectrum measurement in ZPR-3 Assembly 55 have been analyzed and are shown in Fig. I.B.1. These data are identical (within statistics) to the data from the first run on Assembly 55 in the energy

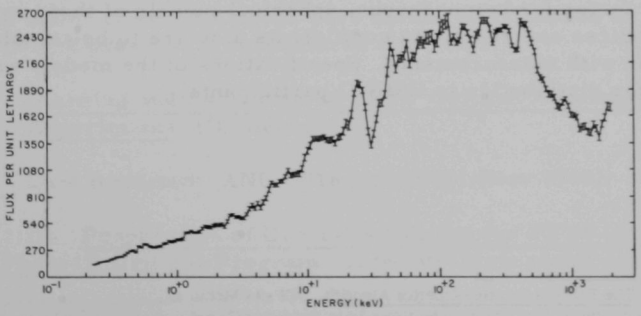

Fig. I.B.1. Neutron Spectrum in ZPR-3 Assembly 55

region above 10 keV. Below 10 keV, the original data were distorted by a count rate-sensitive amplifier in the discrimination electronics system.

With the exception of a relatively flat region between 80 and 500 keV, this spectrum is very similar to that of Assembly 53. The only recognizable structure is a depression at 31 keV due to an iron resonance.

(ii) Experimental Techniques

(a) Techniques of Control-rod Calibration. The method outlined by Cohn* has been revised to include a source correction and programmed for the CDC-1604. The results obtained by its use compare favorably with those of the similar inverse-kinetics technique currently in use at ZPR-3. Test cases run using data from rod calibrations in Assembly 51 gave source values differing from previous determinations by an average of less than 1%.

(iii) Integral Studies of Cross Sections. In the framework of the Data Testing Subcommittee of the Cross Section Evaluation Working Group (CSEWG), a selection of ten fast reactor critical experiments has been proposed for the integral data testing of the Evaluated Nuclear Data File B (ENDF/B). An initial objective of the data testing was the operation of the file with its various processing codes and reactor codes to uncover obvious errors, omissions of data, format errors, code problems, etc. A further specific objective has now been formulated as the immediate testing of the ENDF/B data for the prime reactor constituents ^{239}Pu, ^{235}U, and ^{238}U. Consequently, simple fast-critical cases which emphasize separately these three materials have been selected for analysis using ENDF/B; four of the benchmark cases are plutonium-fueled systems, three are high-enrichment uranium systems, and three are fueled with low-enrichment uranium.

In addition to the emphasis of the particular assemblies on the data for either plutonium, ^{235}U, or ^{238}U, the selection is intended to test the ENDF/B and associated codes on the systems with "hard"-, "medium"-, and "soft"-neutron-spectrum systems. The analyses are to determine the criticality factor for homogeneous, spherical models of these systems. Spectral indices and reactivity coefficients also are to be calculated for comparison with measurements. Specifications of the models are being drawn up for distribution to CSEWG participants.

*Cohn, C. E., The DDP-24 Inverse-Kinetics Algorith, DDP-24 Memo 48.

b. Fast Critical Experiments--Experimental Support (Illinois)

Last Reported: ANL-7478, p. 7 (July 1968).

(i) Detector Development (R. Gold)

(a) Automatic Live-timer Correction in Precision Counting. In counting experiments for which results of high precision are required, a number of computed corrections are usually applied to the raw counting data, including a correction for electronic-channel deadtime for which several somewhat different formulae are currently in vogue. On the other hand, automatic (on-line) deadtime correction by the live-timer method is very readily implemented with available components.* To ascertain the applicability of this method to precision work, the theoretical precision of live-timer-on-line correction was examined. It turned out to be identical with the precision obtained from a standard correction formula which assumes nonextendable deadtime.

In practice, on-line correction may claim to be superior since it does not rely on the absolute stability of the imposed paralysis and further saves the labor of making precise measurements of this paralysis at intervals. Moreover, it delivers corrected counts as the experiment proceeds and thus facilitates control. With a slight modification, the discriminator can be made to suppress certain pileup effects appearing at very high input rates, which the usual formula correction cannot satisfactorily treat.

The live-timer method is sometimes believed to fail for the case of sources that decay appreciably during the count. It can be shown, however, that a certain ratio of the timing-channel blocking gate to the count-channel paralysis will effectively correct for decay during the count interval. Finally, live-timer correction of coincidence counting is found to be, in fact, more precise than correction through the application of usual formulae, since such formulae only account for first-order effects in paralysis. A series of practical tests were made and found to verify these predictions under conditions which were deliberately chosen to be at the extreme limit of practically encountered situations.

c. Planning and Evaluation of FFTF Critical Assembly Experiments (D. Meneghetti)

Last Reported: ANL-7518, pp. 19-21 (Nov 1968).

(i) Preparation of Cross-section Set for FFTF Assembly I of Resumed Phase-B Critical Program. A twenty-nine-group cross-section

*Porges, K. G., and Rudnick, S. J., Live-Timer Method of Automatic Deadtime Correction for Precision Counting, Rev. Sci. Instr. (in press).

set, designated 29004, has been prepared for the neutronic computations associated with Assembly I of the Resumed Phase-B Critical Experiments in support of the FFTF Program. The nominal core and reflector compositions were given in ANL-7518. The ENDF/B Category I basic cross-section data were entered into the MC^2 code.

The heterogeneous treatment was used in a fundamental-mode spectrum for the core cross sections, while the homogeneous zero-buckling spectrum associated with each reflector was used for separately averaging the radial and axial cross sections. The upper energy boundary of the first group was 10 MeV. The lower energy boundary of each group and the corresponding lethargy is given in Table I.B.1.

TABLE I.B.1. Group Boundaries of Cross-section Set 29004

Group	Lower Energy Limit	Lethargy	Group	Lower Energy Limit	Lethargy
1	6.065 MeV	0.5	16	3.355	8.0
2	3.679	1.0	17	2.035	8.5
3	2.231	1.5	18	1.234 keV	9.0
4	1.353 MeV	2.0	19	748.5 eV	9.5
5	820.8 keV	2.5	20	454.0	10.0
6	497.9	3.0	21	275.4	10.5
7	302.0	3.5	22	167.0	11.0
8	183.2	4.0	23	101.3	11.5
9	111.1	4.5	24	61.44	12.0
10	67.38	5.0	25	37.27	12.5
11	40.87	5.5	26	13.71	13.5
12	24.79	6.0	27	5.043	14.5
13	15.03	6.5	28	1.855	15.5
14	9.119	7.0	29	0.6826 eV	16.5
15	5.531	7.5			

TABLE I.B.2. ^{10}B Rod Worths per Kilogram at Various Radial Positions

Radial Position (cm)	%Δk/k per kg ^{10}B
0.50	-4.23
4.50	-4.19
9.50	-4.04
14.80	-3.72
20.75	-3.26
26.85	-2.78
31.66	-2.38
37.68	-1.91
43.70	-1.65
49.11	-1.74

(ii) Calculation of Radial ^{10}B Worths for Assembly I of Resumed Phase B. Scoping estimates were needed to facilitate the positioning of B_4C safety blades for the Resumed Phase-B Assembly I construction in ZPPR.

The small-sample worths for ^{10}B channels having the height of the core are given in Table I.B.2 for various radial positions. For this analysis the core-reflector interface has been assumed to be 51.1 cm. The cross-section set used was 29004. Calculations were made with the perturbation option for the MACH I program.

3. ZPR-3 Operations and Analysis (W. G. Davey and R. L. McVean)

Last Reported: ANL-7518, pp. 21-25 (Nov 1968).

a. Basic Studies of Plutonium Systems

(i) Assemblies 53 and 54. Analyses of hydrogen content of the chromium perturbation samples in Assemblies 53 and 54 have been completed; the samples were found to contain 200 ± 5 ppm hydrogen. The worth of this amount of hydrogen was determined to be +5.84 ± 0.31 Ih. Subtraction of this worth from the average specific worth of the two samples gives the chromium worth listed in Table I.B.3. The uncertainties given are the sums of the uncertainties of the components of the corrected reactivities. The major source of uncertainty was reactor noise.

TABLE I.B.3. Central Perturbation Measurements of Chromium in Assemblies 50 and 53

Sample	Wt (g)	Stainless Steel Wt (g)	Assembly 50 (Ih/kg)	Assembly 53 (Ih/kg)
0.42-in.-dia cyl	15.36	6.412	-13.06 ± 0.57	-
0.42-in.-dia cyl	16.73*	6.78*	-	-10.10 ± 0.45

*Average of 2 samples.

(ii) Assembly 55. The experimental program with Assembly 55, the $k_\infty = 1$ experiment to determine the capture-to-fission ratio in ^{239}Pu, was completed. Final measurements in this program included fission-track foil measurements, fission ratios ($^{238}U/^{239}Pu$), and central reactivity worths of high ^{240}Pu fuel, ^{6}Li, ^{7}Li, carbon, stainless steel, ^{239}Pu, and depleted uranium.

An experiment to determine the effectiveness of polyethylene-boral shielding was also performed during Assembly 55. The purpose of this experiment was to evaluate this type of shield for possible use in a high-power core planned for the future on ZPR-3. The data from Assembly 55 have not been completely reduced yet and will appear in future reports.

(iii) Assembly 55A. Assembly 55A was a repeat of Assembly 55 except for the addition of a high ^{240}Pu zone in the center of the $k_\infty = 1$ region. The same measurements were performed in both assemblies. The data obtained from Assemblies 55 and 55A, when taken together, may permit the determination of the capture-to-fission ratios for both ^{239}Pu and ^{240}Pu.

b. Heterogeneity. Efforts have primarily been directed toward data collection and processing of foils used to determine the neutron economy in Assemblies 55 and 55A. Counting has included five sets of monitor foils (gold and manganese), and twenty plutonium and depleted uranium foils. Analyses of monitor foils are nearly complete. Analyses of the remaining foils continue.

c. Mockup Studies. With the completion of the unloading of Assembly 55A, the preloading of Assembly 56 began. Assembly 56 is a loading in which the core and inner part of the radial reflector contain the same plate arrangement as the FTR Resumed Phase-B Critical Program, Assembly I being built on ZPPR. This assembly is being constructed in parallel to the ZPPR experiment to provide an estimate of the critical mass of such a loading and to determine if the critical mass is within the 430-kg total plutonium limit of ZPR-3. It is predicted that the critical mass will be within ZPR-3 limits, and the experimental program for Assembly I could proceed on ZPR-3 after the entire radial reflector is loaded to Assembly-I specifications.

For the determination of critical mass, the core and reflector compositions are listed in Table I.B.4. These compositions are based upon the ZPPR compositions adjusted to the ZPR-3 void fraction and matrix-drawer stainless steel content. The axial reflector is 27.9 cm thick, and the

TABLE I.B.4. FTR Assembly I of ZPR-3: Nominal Compositions by Zone

Units of 10^{24}/cc

Core

Material	Cell Average	Material	Cell Average
O	0.0150061	^{235}U	0.0000139
Na	0.0089557	^{238}U	0.0062205
Fe	0.0125927	^{239}Pu	0.0013346
Cr	0.0026777	^{240}Pu	0.0001818
Ni	0.0013332	^{241}Pu	0.0000248
Mn	0.0002299	C	0.0011487
Mo	0.0003434		

Ni-Na Reflector

	Axial Reflector		Radial Reflector	
Material	N x 10^{24}	Volume Fraction	N x 10^{24}	Volume Fraction
Na	0.013900	54.7	0.006759	26.6
Ni	0.020033	21.9	0.048081	52.6
Fe	0.008665	10.2	0.007373	8.6
Cr	0.002459	3.0	0.002104	2.6
Void	-	10.2	-	9.6

inner and outer radial reflectors are each nominally 15 cm thick. A portion of the inner reflector is loaded directly in the matrix for the initial mass confirmation. The core zone is being preloaded to a volume which would contain 380 kg total plutonium with a core height of 91.59 cm.

4. ZPR-6 and -9 Operations and Analysis

a. Heterogeneity Effects (C. E. Till)

Last Reported: ANL-7478, pp. 27-30 (July 1968).

Two main types of heterogeneity effects are associated with fast criticals loaded in plate geometries: (1) fast effect, and (2) resonance effect. The fast effect depends on (a) the physical shape of the fissile materials, i.e., thickness and length of column, and (b) the physical separation between the fissile and fertile plates. It gives a positive contribution to the reactivity of the system.

The resonance heterogeneity effect is a self-shielding effect. Resonance neutrons are readily absorbed at the surface of the plate. This process allows fewer such neutrons to reach the interior of the plate, and the overall effect is that the average reaction rates per atom in the plate are lowered. Self-shielding contributes negatively through the fission and positively through the capture processes. Self-shielding in the scattering process can have positive or negative effects on the system; the sign is determined by the relative importance of the neutron before and after scattering.

Three different types of experiments, designed to yield data on the heterogeneity effects, were conducted on a 4000-liter UO_2 core, Assembly 6 of ZPR-6. These experiments comprised the following:

(1) Measurement of the reactivity change associated with two changes of loading patterns and the fine structure of the fluxes in the unit cell of each of the loading patterns;

(2) Measurement and comparison of the relative reactivity worth at the center of the core of homogeneous, rodded-type heterogeneous and plate-type heterogeneous samples; also, measurement of the fine structure of the fluxes in the rodded samples;

(3) Measurement of the reactivity worths of ^{235}U and ^{238}U as a function of sample thickness.

(i) Loading-pattern Effects. The effect of changing the drawer-loading pattern on the reactivity of the system provides a convenient means by which methods used to account for heterogeneity effects can be tested.

Calculations of σ_p for ^{238}U for various loading patterns show that a considerable change in σ_p^{238} takes place when the normal loading pattern (shown in Fig. I.B.2a) is rearranged to the bunched loading pattern of Fig. I.B.2b. Calculations also showed that when the appropriate amount of stainless steel in the matrix and drawer is homogenized with the two $^{238}U_3O_8$ plates in two adjacent cells, the value of σ_p^{238} is increased by 5-10%. For this reason a loading pattern in which the stainless steel was isolated (see Fig. I.B.2c) was used. Table I.B.5 shows the calculated average values of σ_p^{238} and the corresponding capture cross sections for the three loading patterns and for the homogeneous case.

The measured reactivity change associated with the change in loading pattern from that shown in Fig. I.B.2a to that shown in Fig. I.B.2b, in a central region of the core comprising 76 drawers per half (see Fig. I.B.3), was 93.06 Ih (0.203% $\Delta k/k$). The same measurement performed with nine central drawers per half gave 11.53 Ih. The reactivity change associated with such changes in loading pattern was also calculated by a procedure discussed elsewhere.* The calculated values were 63.81 and 8.07 Ih for the change in the 76 and in the 9 drawers per half, respectively.

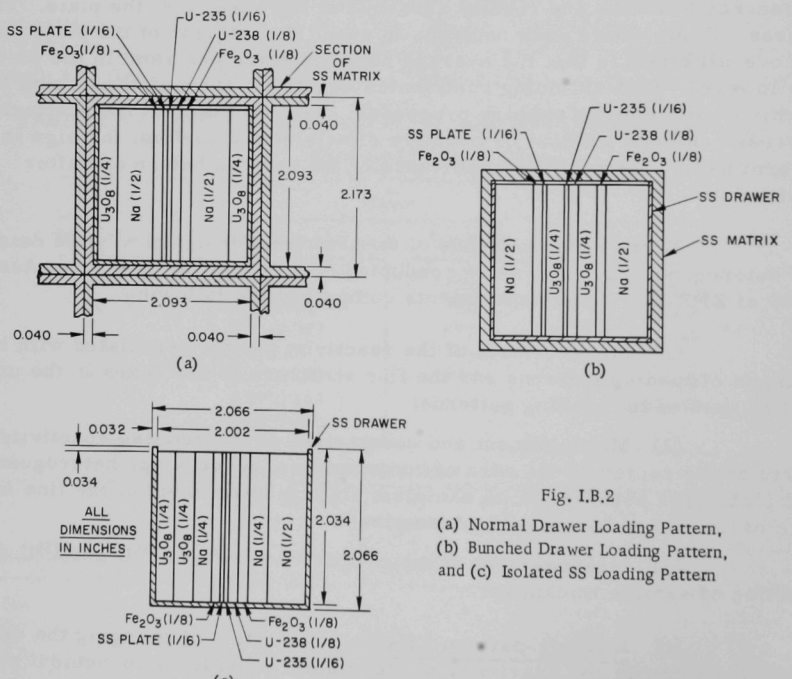

Fig. I.B.2

(a) Normal Drawer Loading Pattern,
(b) Bunched Drawer Loading Pattern,
and (c) Isolated SS Loading Pattern

*Haram, R. A., et al., Trans. ANS 11, 597 (1968).

TABLE I.B.5. Homogenous and Cell-averaged σ_p and Corresponding σ_c of ^{238}U for the Three Loading Patterns of Assembly 6 of ZPR-6

Energy Group	Homogenous[a]		Normal[b]		Bunched[c]		Isolated SS[d]	
	σ_p (b)	σ_c (b)	σ_p (b)	σ_c (b)	σ_p (b)	σ_c (b)	σ_p (b)	σ_c (b)
11	48.69	0.4357	38.63	0.4223	32.41	0.4011	36.43	0.4201
12	40.75	0.5502	34.37	0.5313	30.48	0.5052	32.95	0.5286
13	51.97	0.6721	40.37	0.6426	33.37	0.6021	37.70	0.6375
14	69.53	0.8206	47.38	0.7690	36.02	0.7030	42.64	0.7579
15	107.3	1.048	53.58	0.9121	37.29	0.8134	46.46	0.8884
16	91.13	1.097	49.69	0.9467	36.69	0.8394	44.36	0.9199
17	58.02	0.9724	42.40	0.8702	34.91	0.7867	39.37	0.8513
18	56.30	1.117	42.10	0.9874	35.22	0.8885	39.38	0.9649
19	57.27	1.203	42.56	1.035	35.66	0.9174	39.80	1.006
20	60.09	1.147	43.72	0.9810	36.59	0.8768	40.76	0.9534
21	64.50	1.676	45.09	1.339	38.44	1.181	42.03	1.288
22	67.04	2.129	45.71	1.701	39.57	1.526	42.68	1.642

[a]All materials homogenized.
[b]Loading pattern of Fig. I.B.2a.
[c]Loading pattern of Fig. I.B.2b.
[d]Loading pattern of Fig. I.B.2c.

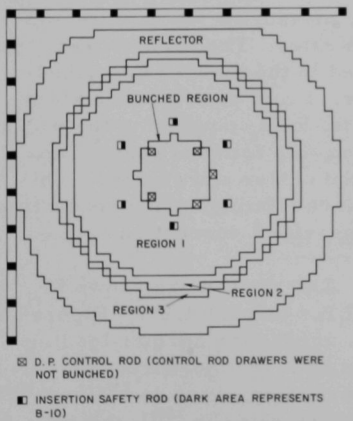

Fig. I.B.3. Half-core of Assembly 6 of ZPR-6

The measured change in reactivity corresponding to the change in loading pattern from that in Fig. I.B.2a to Fig. I.B.2c, in a square region comprising the 25 central drawers per half, was 4.47 Ih. The calculated value for such change was 2.99 Ih.

In addition to the measurements of loading-pattern effects on the reactivity of the system, an independent series of experiments, measuring the fission rates in ^{235}U and ^{238}U as well as the capture rates in ^{238}U, was made as a function of position in the unit cell. Such integral measurements provided tests to verify the adequacy of the methods for predicting the spatial fine structure of the fluxes in the unit cell. (It should be noted that the detailed shapes of the fluxes have a significant influence on the spatially averaged cross sections.)

Depleted-uranium foils (0.2% enrichment, 5 mils thick by 5/8 in. in diameter) and ^{235}U foils (93% enrichment, 4.5 mils thick by 3/8 in. in diameter) were placed at corresponding locations about the center of the

core in the two halves of the ZPR-6 machine.* The foils were placed between the adjoining surfaces of all the plates in the unit cell. All foils were irradiated for one hour at a power level of about 50 W. After five hours of irradiation, the activities of the ^{238}U foils were counted for fission fragments (counting gammas with energies above 0.41 MeV) and for capture by counting the 106-keV gammas from excited ^{239}Pu in coincidence with X rays produced by internal K-conversion electrons. The 5-hr waiting period was necessary to allow sufficient time for the buildup of ^{239}Np from ^{239}U. The ^{235}U foils were counted for fission fragments in a similar manner to the ^{238}U foils. A few foils were radiochemically analyzed for the absolute number of fissions in ^{235}U and absolute number of fissions and captures in ^{238}U. The radiochemical results were used to obtain efficiency factors to convert the rest of the data to absolute numbers. Irradiations of the ^{235}U and ^{238}U foils were performed in each of the loading patterns shown in Fig. I.B.2.

In another experiment, a 2 x 2 x 1/16-in. plate of 93% enriched uranium and a 2 x 2 x 1/8-in. plate of depleted uranium (0.2% enriched) that were normally in the core were replaced by packets of foils equivalent in weight and enrichment to the two plates. This arrangement provided means by which the spatial distribution of the fluxes within the fissile and fertile plates can be verified by measuring the capture and fission rates. The packets were irradiated in the manner described earlier. From each of the 2 x 2 x 0.005-in. foils comprising the packets, a 5/8-in.-dia foil was punched out from the center and counted. This procedure eliminated any requirement for edge-effect corrections.

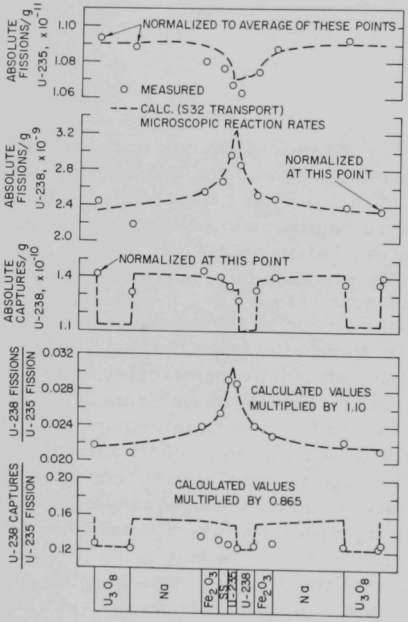

Fig. I.B.4. Measured and Calculated Values of ^{235}U Fission Rate, ^{238}U Fission Rate, ^{238}U Capture Rate, and Their Ratios in "Normal" Loading of Assembly 6 of ZPR-6

The results are shown in Figs. I.B.4 through I.B.7. Figure I.B.4 shows, across the normal-loading-pattern cell, the measured and calculated fission rates in ^{235}U and ^{238}U, the capture rates in ^{238}U, the ratio of fission in ^{238}U to fission in ^{235}U, and the ratio of capture in ^{238}U to fission in ^{235}U. The calculated fission rates in ^{235}U and ^{238}U were obtained using the cell fluxes from the SNARG-1D code,** with ^{32}S and modified Gaussian

*Kato, W. Y., et al., ANL-6271 (1963). **Duffy, G. J., et al., ANL-7221 (1966).

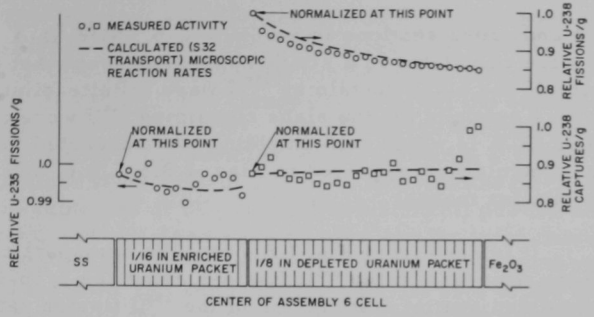

Fig. I.B.5. Relative Fissions in ^{235}U and ^{238}U Packets and Relative Capture in ^{238}U Packet Simulating the ^{235}U and ^{238}U Plates in Assembly 6 of ZPR-6

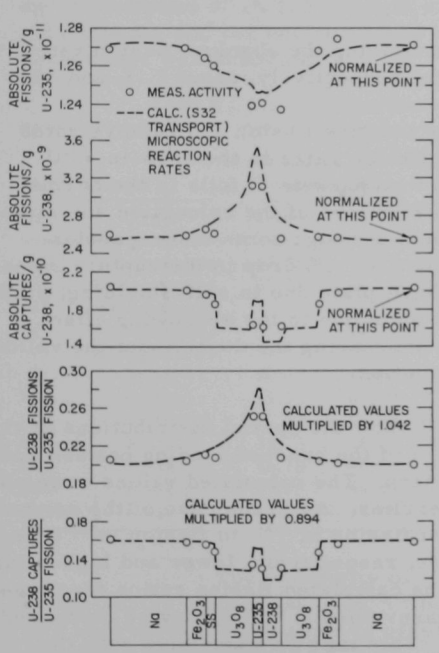

Fig. I.B.6. Measured and Calculated Values of ^{235}U Fission Rate, ^{238}U Fission Rate, ^{238}U Capture Rate, and Their Ratios in "Bunched" Loading Pattern of Assembly 6 of ZPR-6

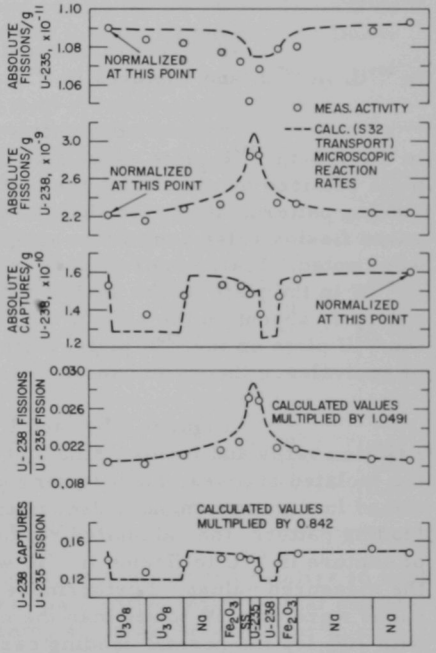

Fig. I.B.7. Measured and Calculated Values of ^{235}U Fission Rate, ^{238}U Fission Rate, ^{238}U Capture Rate, and Their Ratios in an "Isolated SS" Loading Pattern of Assembly 6 of ZPR-6

quadratures,* and cross sections in Set ZPR-6-6 ENDF/B-A. The capture rates in ^{238}U were calculated in a similar manner except that the cross sections used outside the slabs containing ^{238}U were infinite-dilution cross sections. The cross sections for the slabs containing ^{238}U were those of ZPR-6-6 ENDF/B-A in which self-shielding was accounted for by equivalence theory. Calculations reported in Figs. I.B.5, I.B.6, and I.B.7 were obtained in a similar manner.

It is seen from Fig. I.B.4 that the transport calculations underpredict the decrease in the ^{235}U fissions about the 1/16-in. plate of ^{235}U. The calculated spatial distribution of the ^{238}U fission rates is in fair agreement with the measurements. The measured and calculated capture rates in ^{238}U are in apparent agreement although the step-function description of the ^{238}U capture cross sections would not reflect flux depression in the vicinity of the ^{238}U plates. (Note that the point of normalization is arbitrary.) The calculated ratio of fission in ^{238}U to fission in ^{235}U is overestimated by about 15%.

The accuracies in determining the absolute fission rates in ^{235}U, in ^{238}U, and captures in ^{238}U are, respectively, about 2, 5, and 5%.

Figure I.B.5 shows the relative fission and capture rates in the 1/8-in. ^{238}U plate as well as the fission rates in the 1/16-in. ^{235}U plate obtained by simulating the plates with packets of foils in the normal loading pattern. It is seen that the distributions of the calculated and measured fission rates are in fair agreement although some discrepancies were noted. Furthermore, there is about 10-15% drop in the capture rates of ^{238}U in the plate on the side of the Fe_2O_3 plate due to self-shielding; such a drop is absent on the side of the ^{235}U plate due to the shadowing effect of the ^{235}U plate on the ^{238}U plate, further increasing the doubt about the validity of equivalence theory to handle this situation.

Figures I.B.6 and I.B.7 show the spatial distributions of the reaction rates and ratios in the unit cell of the bunched loading pattern and the isolated stainless steel loading pattern. The calculated values were obtained in the same manner described earlier. As in the case of the normal loading pattern, the calculated ratios of fission in ^{238}U to fission in ^{235}U and of capture in ^{238}U to fission in ^{235}U were, respectively, lower and higher than the measured values. Furthermore, the calculated fission ratios for these cases were only 5% lower than the measurements, which may be compared with 10% for the normal-loading case. This may be associated with the fact that the one-dimensional transport calculations do not account for streaming accurately. (The sodium channels in the bunched and isolated stainless steel cases were wider than in the normal case when one considers two adjacent unit cells.)

*Meneghetti, D., Nucl. Sci. Eng. 11, 295 (1962).

(ii) Relative Reactivities of Homogeneous, Pellet-heterogeneous, and Plate-heterogeneous Samples. The relative reactivity worths of a nominally 2-in. cube, plate, and rodded and homogeneous samples, were measured in Assembly 6 of ZPR-6. The compositions of all the samples were essentially the same (see Table I.B.6). The plate-type sample had the loading pattern of Fig. I.B.2a. All samples were encased in a 1.90 x 1.90 x 2.00-in. Type 304 stainless steel cans of 0.015-in. wall thickness. The homogeneous samples were mixtures of UO_2 (16.42% enrichment) powder and sodium or of UO_2, sodium, and stainless steel powder, the latter to mockup the stainless steel tubes in the rodded samples. The stainless steel and UO_2 powders were blended together and sintered; the particle size of the blend was such that only about 53% of the volume would be used when packed under vibration. The empty volume fraction was filled with sodium. Tests conducted with X rays, as well as an actual opening of one can, revealed that the mixture was quite homogeneous. The rodded samples consisted of 0.25-in.-dia by 1/2-5/8-in.-long pellets inserted in 36-tube calandria cans. The pellets consisted of two enrichments, 19.947 and 15.861%, prorated to give an average enrichment of 16.43%. A test of the reactivity worth of UO_2 with both enrichments and the two combined showed that the assumption of linear dependence was adequate.

TABLE I.B.6. Samples Used in Study of Heterogeneity Effects

Sample		Composition (g)						Enrichment of UO_2 (w/o ^{235}U)
		Stainless Steel			Total			
No.	Type	Sample	Can	Fe	SS + Fe	Na	UO_2	
1	Homogeneous	58.00	46.10	45.74	149.84	-	392.87	16.42
2	Homogeneous	57.97	46.18	45.72	149.87	52.89	392.66	16.42
3	Homogeneous	-	46.36	-	46.36	-	452.00	16.42
4	Homogeneous	-	46.36	-	46.36	-	392.87	16.42
9	Homogeneous	-	46.05	-	46.05	69.17	392.87	16.42
8	Pellet	60.39	46.00	-	106.39	41.33	392.65	16.42
11A	Pellet	61.17	46.00	-	107.17	-	392.60	16.42
11B	Pellet	61.17	46.00	32.31	139.48	-	392.60	16.42
11A	Plate	45.18	46.08	46.28	137.54	42.94	399.29	16.41
11B	Plate	45.18	46.08	46.28	137.54	-	399.29	16.41
20A	Plate	45.35	34.25	46.88	126.29	-	403.36	16.40
20B	Plate	45.35	34.25	46.88	126.29	42.94	403.36	16.40

The reactivity of a sample was measured relative to void by the period method (at least 5 times); the relative worth of that sample was then measured relative to other samples using an oscillator in conjunction with an autorod. The autorod was calibrated differentially and integrally "on-line" with the aid of a code recently developed.*

*Cohn, C. E., Trans. ANS 11(2) (1968).

In addition to the rodded samples used for oscillation, there were 26 (2.00 x 2.00 x 3.17-in) calandria cans with which a rodded zone was built around the sample being oscillated at the center of the core. This rodded zone comprised the first 3 in. of 13 drawers in each half of Assembly 6. The relative reactivity worths of the plate, rodded, and homogeneous samples were measured in the rodded-zone enrivonment as well.

The results are given in Table I.B.7. All samples were measured relative to homogeneous Sample No. 3, which was measured relative to void by the period method. The errors listed reflect the relative errors associated with the oscillation method and not the period method. The values listed for samples without sodium contain minor corrections accounting for small differences in composition between homogeneous Sample No. 1 and the rest. The values for the samples with sodium have been normalized to the composition of homogeneous Sample No. 2. The corrections were prorated linearly according to the worth of the material in its particular geometry. For example, the worth of stainless steel powder was obtained from the relative worths of homogeneous Samples Nos. 1 and 4.

TABLE I.B.7. Measured Reactivity Worths at Center of Assembly 6 of ZPR-6

Sample No.	Sample Type	Sample Worth Relative to Void (Ih)[a]	
		Normal Plate Environment	Pellet Environment
1	Homogeneous with SS, no Na	1.364 ± 0.003	1.379 ± 0.002
11B	Pellet, no Na	1.351 ± 0.004	1.345 ± 0.003
11B	Plate, no Na	1.369 ± 0.005	-
20A	Plate, no Na	-	1.367 ± 0.003
2	Homogeneous with Na and SS	1.361 ± 0.002	1.375 ± 0.003
20B	Plate with Na	1.359 ± 0.003	1.367 ± 0.003
8	Pellet with Na	1.347 ± 0.003	1.359 ± 0.003

[a] 1% $\Delta k/k$ = 458 Ih.

It is seen from Table I.B.7 that the relative reactivities of the plate, and the rodded and homogeneous samples are essentially the same. It appears that the various effects, such as the increase in capture in ^{238}U and fission in ^{235}U in the homogeneous samples relative to the heterogeneous samples, largely cancel.

In a separate experiment, the first 3-in. plate-loaded segments in 26 drawers were replaced with 26 (3-in.) pellet cans at the core center. The relative reactivity difference for all 26 cans was only 1.61 Ih.

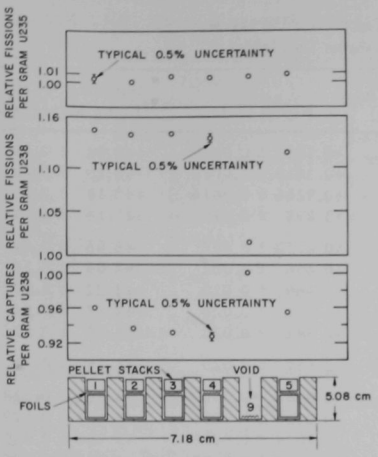

Fig. I.B.8. Diagonal Cross Section of Pellet Can

The fission rates in ^{235}U and fission and capture rates in ^{238}U were measured in the 3-in. calandria cans. Depleted and 93% enriched uranium foils (of 0.25-in. diameter) were placed between the last two pellets in tubes along the diagonal line of the calandria. In one tube there were no pellets and therefore the foil was placed at the bottom. The foils were irradiated and analyzed in the manner described earlier. The results are shown in Fig. I.B.8.

It is seen from Fig. I.B.8 that the spectrum in the empty tube is significantly softer in the high-energy groups (fission in ^{238}U) than that in the pellet-filled tubes. Furthermore, the captures in the ^{238}U foil in the empty tube are also higher than the average captures in a foil "sandwiched" between two pellets. This indicates that there are heterogeneity effects in the rodded samples; yet these effects combine in such a way that the reactivities of the rodded, plate, and homogeneous samples tend to equalize.

(iii) Reactivity Worths of ^{235}U and ^{238}U as a Function of Thickness. The calibrated autorod was used in the measurement of the reactivity worths of ^{235}U and ^{238}U as a function of sample thickness. The samples were 0.005-in.-thick foils with a nominal area of 4 in. square, stacked together, and placed in a 2 x 2 x 2-in. stainless steel can on a 1/32-in. wire rack that supported the samples at 1 in. from the bottom of the can. The samples were oscillated relative to an empty stainless steel can with wire racks. In the case of ^{235}U, the reactivity worth as a function of sample thickness was also measured in the exact environment of the normal core-loading pattern. This particular measurement comprised the oscillation of 2 x 2 x 2-in. stainless steel cans, relative to each other, loaded in the same manner as in the core and contained the same materials except for ^{235}U, which was present in one can only. The results are given in Table I.B.8.

On the basis of the results shown in Table I.B.8 the following remarks can be made:

(1) Self-shielding in ^{235}U is significant in the core environment but absent in the 2 x 2 x 2-in. cavity at the core center.

(2) The fast heterogeneity effect is noticeable in the worths of the 16 foils of ^{235}U suspended in the empty stainless steel can.

(3) Self-shielding in ^{238}U is significant.

TABLE I.B.8. Reactivity Worths of ^{235}U, ^{238}U, Iron, and Nickel as a Function of Sample Thickness

Material and Environment	No. of Foils	Total Foil Wt (g)	Worth (Ih)	Specific Worth (Ih/kg Material)
93% Enriched Uranium Foils	1	4.638	+0.1857 ± 0.0019	+40.04 ± 0.41
Suspended in a 2 x 2 x 2-in.	2	9.002	+0.3619 ± 0.0018	+40.20 ± 0.20
Empty Stainless Steel Can	5	23.059	+0.9266 ± 0.0016	+40.18 ± 0.07
	16	73.634	+3.039 ± 0.010	+41.14 ± 0.14
93% Enriched Uranium Foils	1	4.511	+0.2110 ± 0.002	+46.66 ± 0.44
in Plate-type Heterogeneous	2	9.221	+0.406 ± 0.002	+44.06 ± 0.22
Cans Identical to Core-	5	22.950	+0.969 ± 0.020	+42.22 ± 0.87
loading Pattern	8	36.851	+1.544 ± 0.020	+42.17 ± 0.54
	14	64.349	+2.682 ± 0.020	+41.68 ± 0.31
1/16-in. Plate		61.491	+2.567 ± 0.020	+41.75 ± 0.31
Depleted-uranium Foils	1	5.913	-0.0252 ± 0.0017	-4.262 ± 0.288
Suspended in a 2 x 2 x 2-in.	2	11.739	-0.0429 ± 0.0021	-3.654 ± 0.179
Empty Stainless Steel Can	5	28.977	-0.1034 ± 0.0016	-3.568 ± 0.055
	10	60.227	-0.2202 ± 0.0015	-3.656 ± 0.025
	25	147.123	-0.5136 ± 0.0018	-3.491 ± 0.009
2 x 2 x 1-in. Block		1153.58	-3.764 ± 0.01	-3.263 ± 0.009

(iv) Conclusions. The extensive measurements of heterogeneity effects conducted with Assembly 6 of ZPR-6 show that the theoretical methods used can predict such effects qualitatively but not quantitatively. The sources of errors can be any or all of the following: (1) basic data (ENDF/B file), (2) nonapplicability of equivalence theory, and (3) use of a few (22) groups to obtain the spatial distribution of the fluxes with which the cross sections are averaged in the unit cell. It is unclear how much of the discrepancy should be attributed to the basic data. More work is required in refining and validating the calculational methods before definitive conclusions could be drawn.

b. Integral Studies of Large Systems (W. Y. Kato)

Last Reported: ANL-7500, pp. 22-27 (Sept 1968).

(i) Plutonium-alpha Measurements. Analysis of the null-reactivity plutonium-alpha measurement made with ZPR-3 Assembly 55 (see Progress Report for November 1968, ANL-7518, pp. 23-25) is in progress. Measurements were made in two different null zones. In each case the zones were made up of plates of plutonium metal, depleted uranium, carbon, and the stainless steel in the matrix and drawers; in the first zone were the regular plutonium plates (which were 95% ^{239}Pu), and in the second zone were plutonium plates containing approximately 22% ^{240}Pu. The average homogenized atomic concentrations for the two zones are given in Table I.B.9.

TABLE I.B.9. Average Atom Densities (x 10^{24}) in Null Zone

Material	Zone 1 (Regular Plutonium)	Zone 2 (22% ^{240}Pu)
C	0.037269	0.033313
Al	0.000111	0.000118
Cr	0.001895	0.002194
Fe	0.006177	0.007149
Ni	0.000839	0.000971
^{235}U	0.000033	0.000027
^{238}U	0.015282	0.012668
^{239}Pu	0.001068	0.000851
^{240}Pu	0.000051	0.000255
^{241}Pu	0.000005	0.000053

The exact null compositions were determined by measuring the reactivity worths of small (2 x 2 x 2-in.) boxes containing plates of plutonium, depleted uranium, carbon, and stainless steel. The preliminary values for the null-composition weight ratios are given in Table I.B.10. The ratios relative to equivalent ^{239}Pu are given, and the equivalent ^{239}Pu was obtained by using the calculated worths of the plutonium isotopes to convert the ^{240}Pu and ^{241}Pu in the plutonium plates to equivalent ^{239}Pu. The null-composition weight ratios are very close to being in agreement with the average null-zone atom densities listed in Table I.B.9. It was not possible, because of plate-size limitations, to load the null zone to the exact null compositions, however.

TABLE I.B.10. Measured Null-composition Weight Ratios

Material	Zone 1 (Regular Plutonium)	Zone 2 (22% ^{240}Pu)
Equivalent ^{239}Pu	1.000	1.000
Depleted Uranium	14.25 ± 0.02	13.68 ± 0.06
Carbon	1.737	1.780
Stainless Steel	1.914	2.540

(ii) Central Reactivity Measurements. The measurements of central reactivity worth routinely conducted with ZPR-6 and -9 materials provide a convenient means of verifying material cross-section data sets in a particular neutron spectrum if sample-size effects are accounted for correctly. In this work, corrections to first-order perturbation theory incorporating self-shielding effects both inside and outside the sample, as well as scattering, fission, and edge-effect perturbations, were made for each energy group. This method was applied to the analysis of the central-worth measurements in Assembly 6 of ZPR-6.

(a) Theory. The basic concept used was the calculation of the ratio of the actual average flux in the sample to the unperturbed flux for each energy group. This ratio was then used to multiply the components of $\delta k/k$, i.e., absorption, fission, scattering, and leakage in each group, obtained from first-order perturbation (FOP) calculations. The perturbed-to-unperturbed flux ratio R_i in group i can be expressed as

$$R_i = \frac{\overline{C_i}}{(\Sigma_a)_i T \phi_i^0}, \qquad (1)$$

where $\overline{C_i}$ is the absorption rate in group i per unit surface area of a finite sample of thickness T, Σ_{ai} is the absorption cross section in group i, and ϕ_i^0 is the unperturbed flux prior to the insertion of the sample.

The formulation for $\overline{C_i}$ is based in part on the single-scattering treatment of Beckurts and Wirtz.* We consider first the infinite-slab problem. For such a case the number of neutrons in group i which suffer their first collision in dx about x is

$$P_{1i}(x)\,dx = (\phi_i^0/2)\{E_2[\Sigma_{ti}(T - x)] + E_2(\Sigma_{ti}x)\}\,\Sigma_{ti}\,dx, \tag{2}$$

where $E_2(\ )$ is the exponential function of order 2, Σ_{ti} is the total cross section in group i, and T is the thickness of the slab.

The fraction of the total collisions which lead to absorption in group i is given by Σ_{ai}/Σ_{ti}, whereas the number of neutrons born into any group j due to a collision in group i is given by

$$A_{i\to j} = \frac{\Sigma_{si\to j} + \chi_j(\nu\Sigma_f)_i}{\Sigma_{ti}}. \tag{3}$$

The probability that a neutron isotropically scattered in dx about x in the sample escapes without making another collision is

$$\tfrac{1}{2}\{E_2[\Sigma_{ti}(T - x)] + E_2(\Sigma_{ti}x)\};$$

therefore the nonescape probability is

$$B_j(x) = 1 - \tfrac{1}{2}\{E_2[\Sigma_{tj}(T - x)] + E_2(\Sigma_{tj}x)\}, \tag{4}$$

and the number of neutrons which suffer a second collision in group j is

$$P_{2j} = \sum_{i=1}^{NG} A_{i\to j} \int_0^T P_{1i}(x)B_j(x)\,dx. \tag{5}$$

The symbol NG designates the number of groups. Note that the summation over i = 1 to NG is done to allow for fission neutrons contributed to the various groups when the collision ends in a fission. Now, given that a second collision takes place and assuming that P_{2j}, an integral quantity over the sample, has a flat distribution, the number of neutrons that suffer three collisions is

$$P_{3j} = \sum_{i=1}^{NG} A_{i\to j} \int_0^T (P_{2i}/T)B_j(x)\,dx, \tag{6}$$

*Beckurts, K. H., and Wirtz, K., Neutron Physics, translated by L. Dresner, Spring-Verlag, New York (1964), pp. 239-246.

which may be written as

$$P_{3j} = \sum_{i=1} A_{i\to j} P_{2i} \overline{B}_j, \tag{7}$$

where

$$\overline{B}_j = \int_0^T B_j(x)\,dx \Big/ \int_0^T dx.$$

In a similar manner the number of neutrons that undergo k collisions are

$$P_{kj} = \sum_{i=1}^{NG} A_{i\to j} P_{k-1,i} \overline{B}_j. \tag{8}$$

The total number of neutrons absorbed in the infinite slab of thickness T in group j after k collisions can now be written as

$$C_j = (\Sigma_{aj}\Sigma_{tj})\left\{\int_0^T P_{1j}(x)\,dx + \sum_{i=1}^{NG} A_{i\to j} \int_0^T P_{1i}(x) B_j(x)\,dx \right.$$

$$+ \overline{B}_j \sum_{i=1}^{NG} A_{i\to j}\left(\sum_{n=1}^{NG} A_{n\to i} \int_0^T P_{1n}(x) B_i(x)\,dx\right) + \ldots$$

$$\left. + \left[\overline{B}_j \sum_{i=1}^{NG} A_i T_j P_{k-1,i}\right]\right\}. \tag{9}$$

The foregoing development is rigorous within the broad-group approximation of the neutron spectrum for infinite slabs only. Considerations of neutrons that make collisions through the edge of a disk-shaped sample was treated by Hanna.* The increase in the number of collisions due to the finiteness of the sample can be represented as

$$P'_{kj} = P_{kj}(1 + \epsilon_j), \tag{10}$$

where P'_{kj} is the number of neutrons that suffer k collisions in the finite sample and ϵ is given by the expression

$$\epsilon_j = \{2\Sigma_{tj}T/[1 - 2E_3(\Sigma_{tj}T)]\}\,(2/\pi n)\{I[\Sigma_{tj}T - \Delta(n\Sigma_{tj}T)]\}, \tag{11}$$

*Hanna, G. C., Nucl. Sci. Eng. 15, 325 (1963).

where

$$n = 2R/T \equiv \text{the radius-to-thickness ratio,}$$

$$I(\Sigma_{tj}T) = (2/\Sigma_{tj}T)\int_0^{\pi/2}\left\{1 + e^{-\Sigma_{tj}T \sec\theta} - [2/(\Sigma_{tj}\sec\theta)]\left(1 - e^{-\Sigma_{tj}T\sec\theta}\right)\right\}\sin^2\theta\, d\theta, \tag{12}$$

and

$$\Delta(n\Sigma_{tj}T) = \int_0^1 E_2(n\Sigma_{tj}T \sin\phi)d(\cos\phi). \tag{13}$$

As the collision density increases because of the finite size of the sample, so does the escape probability. The decrease in the nonescape probability due to the finiteness of sample is taken into account by multiplying the quantities B_j of Eq. (4) by the ratio of the nonescape probabilities of the finite to the infinite samples as obtained from the rational approximation. Specifically, this ratio can be written as:

$$K_i = \frac{\left(1 - \dfrac{1}{1 + \dfrac{4V}{S}\Sigma_{tj}}\right)_{\text{finite}}}{\left(1 - \dfrac{1}{1 + \dfrac{4V}{S}\Sigma_{tj}}\right)_{\text{infinite}}}$$

$$= \left[\frac{1 - \dfrac{1}{1 + \dfrac{2\Sigma_{tj}T}{1 + \dfrac{T}{R}}}}{1 - \dfrac{1}{1 + 2\Sigma_{tj}T}}\right], \tag{14}$$

where V and S are the volume and surface area of the sample.

Finally, the effect of the sample on the flux outside the sample must be considered. The outer flux perturbation may be defined as the ratio of the flux at the surface of the sample to the flux at the same point prior to the introduction of the sample. This perturbation factor can be expressed* as

$$F_i = (1 + \{\tfrac{1}{2} - E_3[\Sigma_{ti}T]\}\, g_i)^{-1}, \tag{15}$$

*Ritchie, R. H., and Eldridge, H. B., Nucl. Sci. Eng. 8, 300 (1960).

where the g factor can be approximated* by the relation

$$g_i = 1.05(R\Sigma_{ti}). \tag{16}$$

The final relationship governing the number of neutrons absorbed per unit area in a circular disk of radius R and thickness T in group j after k collisions can be written as

$$\overline{C_j} = (F_j\Sigma_{aj}/\Sigma_{tj})\left\{\int_0^T P'_{1j}(x)\,dx + \sum_{i=1} K_jA_{i\to j}\int_0^T P'_{1i}(x)B_j(x)\,dx \right.$$

$$\cdot\,\overline{B_j}\left(\sum_{i=1}^{NG} K_jA_{i\to j}\right)\left[\sum_{n=1}^{NG} K_iA_{n\to i}\int_0^T P_{1n}(x)B_i(x)\,dx\right] + \ldots$$

$$\left. + \overline{B_j}\sum_{i=1}^{NG} K_jA_{i\to j}P_{k-1,i}\right\}. \tag{17}$$

Equation (17) was used in conjunction with Eq. (1) to obtain the appropriate correction factors to first-order perturbation calculations.**

(b) Comparison of Theory and Measurements. The foregoing theoretical treatment of self-shielding was used to calculate the central reactivity worths of various samples whose worths had been measured in a large oxide core, Assembly 6 of ZPR-6. Assembly 6 was a 4000-liter cylindrical core reflected with 30 cm of depleted uranium (0.2% enrichment).

The reactivity worth of a sample was measured by either of two methods: (1) If the reactivity of a sample was one inhour or more, its worth was determined by the period method, i.e., measuring repetitively the period of a slightly above critical system (~10 Ih) with and without (void) the sample at the center of the core. The accuracy of this procedure is typically 0.005 Ih. (2) The reactivity of a small sample was determined by oscillating the sample relative to void and using a calibrated autorod. The accuracy inherent in this technique can be as low as 0.001 Ih provided the autorod is accurately calibrated. The samples used were 2 in. square (nominally) by various thicknesses.

The calculated and measured values for the central worths in Assembly 6 are compared in Table I.B.11. The third column in Table I.B.11 lists the calculated values obtained by first-order perturbation (FOP) theory* and cross section set 224.† Values in parentheses were

*Reactor Physics Constants, Sect. 9, ANL-5800 (1963).

**Menely, D. A., et al., ANL-7223 (1966).

†O'Shea, D. M., et al., Trans. ANS 7, 242 (1964).

obtained with Set ZPR-6-6 ENDF/B-A generated specifically for Assembly 6. The FOP values were corrected for self-shielding according to Eq. (17) with the number of consecutive scatterings terminated after 5, and the results are listed in the fourth column. The measured values are listed in the last column.

TABLE I.B.11. Measured and Calculated Central Reactivity Worths in Assembly 6 of ZPR-6

Material	Sample Weight (g)	Calculated Worth,[a] (Ih)[b] First-order Perturbation (FOP)	FOP Corrected for Self-shielding	Measured Worth (Ih)
Fe	488.0	-0.745[c] (-0.658)[d]	-0.646 (-0.561)	-0.450 ± 0.004
Ni	546.0	-1.069 (-0.721)	-0.929 (-0.748)	-0.833 ± 0.008
Cr	220.73	-0.363 (-0.403)	-0.352 (-0.369)	-0.222 ± 0.008
Na	51.38	-0.023 (+0.002)	-0.033 (-0.004)	+0.013 ± 0.008
^{10}B	29.29	-33.015 (-32.842)	-21.945 (-22.145)	-23.209 ± 0.010
Ti	90.42	-0.045 -	-0.061 -	+0.026 ± 0.013
Zr	406.0	-0.464 -	-0.425 -	-0.443 ± 0.007
Nb	481.2	-5.259 -	-4.290 -	-3.525 ± 0.007
Mo	599.0	-3.888 (-6.211)	-3.165 (-4.371)	-3.115 ± 0.021
Al	165.33	-0.279 (-0.204)	-0.263 (-0.192)	-0.122 ± 0.010
C	103.0	+0.036 (+0.060)	+0.042 (+0.066)	+0.366 ± 0.002
Be	114.31	- (-0.4711)	- (-0.352)	+1.304 ± 0.003
^{238}U	5.913	-0.0211 (-0.0248)	-0.0211 (-0.0248)	-0.0252 ± 0.002
^{238}U	11.739	-0.0420 (-0.0493)	- (-0.0494)	-0.0429 ± 0.002
^{238}U	28.977	-0.1037 (-0.1216)	- (-0.122)	-0.103 ± 0.002
^{238}U	60.227	-0.215 (-0.253)	- (-0.255)	-0.220 ± 0.002
^{238}U	147.123	-0.526 (-0.617)	- (-0.623)	-0.514 ± 0.002
^{238}U	1153.580	-4.132 (-4.838)	- (-3.710)	-3.764 ± 0.003
^{235}U	4.511	- (+0.191)	- (+0.190)	+0.186 ± 0.002
^{235}U	22.950	- (+0.969)	- (+0.986)	+0.947 ± 0.002
^{235}U	61.491	- (+2.596)	- (+2.665)	+2.567 ± 0.020

[a] Calculated with one-dimension diffusion theory (see Reactor Physics Constants, ANL-5800 (1963), Sect. 9).

[b] 1% $\Delta k/k$ = 458 Ih.

[c] Values obtained from cross section set 224 (see D. M. O'Shea et al., Trans. ANS 7, 242 (1964)).

[d] Values in parentheses obtained from ENDF/B parameters.

It is seen from Table I.B.11 that a significant improvement in the agreement between the calculated and measured values results as a consequence of the self-shielding corrections. Note that for ^{10}B, for which the cross sections are smooth with energy, the agreement between the calculated and measured value is very good. For ^{238}U, which has many resonances, the agreement with measurements is good for the thinnest and thickest samples. This may be due to negligible self-shielding in the thinnest sample and to a small contribution from resonance neutrons to the total worth of the large sample. The calculated values for iron, chromium, niobium, aluminum, and molybdenum are somewhat higher than the measured values. This discrepancy could very well be due to the inadequacy of the multigroup approximation to the neutron spectrum in the

resonance energy range rather than to inaccuracies in basic data. In the case of nickel, ENDF/B data seem to result in low values for the cross sections. For molybdenum, the ENDF/B values are significantly different from those of cross section set 224. The calculated and measured values of ^{235}U are in good agreement.

The disagreement between the calculated and measured values of scattering materials such as carbon and beryllium may be associated with inaccuracies in the calculated adjoint fluxes rather than with errors in basic data.

The calculated worth as a function of the number of consecutive scatterings in the sample for a few materials is shown in Table I.B.12. It is seen that convergence has been achieved with five scatterings for practically all the materials except sodium, beryllium, and carbon.

TABLE I.B.12. Calculated Central Reactivity Worths as a Function of the Number of Consecutive Scatterings in Sample (2 x 2 x 1 in.)

	Worth (Ih)[a]				
			No. of Consecutive Scatterings in Sample		
Material	Measurement	FOP[b] Values	1	3	5
Na	+0.013 ± 0.008	-0.00230	-0.00989	-0.00503	-0.00424
Fe	-0.450 ± 0.004	-0.6581	-0.4856	-0.5448	-0.5607
Ni	-0.832 ± 0.008	-0.7204	-0.7184	-0.7514	-0.7477
Cr	-0.222 ± 0.008	-0.4034	-0.3375	-0.3622	-0.3692
^{10}B	-23.208 ± 0.012	-32.842	-21.812	-22.139	-22.145
Mo	-3.115 ± 0.021	-6.2113	-3.5795	-4.2362	-4.3713
Al	-0.122 ± 0.010	-0.2042	-0.1803	-0.1906	-0.1920
Mn	-0.481 ± 0.006	-1.1963	-0.5028	-0.5702	-0.5939
^{9}Be	-1.304 ± 0.003	-0.4711	-0.5686	-0.4325	-0.3525
C	-0.366 ± 0.001	0.06037	0.00991	0.05527	0.06644

[a] 1% $\Delta k/k$ = 456 Ih.
[b] First-order perturbation-theory calculations with ENDF/B data.

5. ZPPR Operations and Analysis (W. G. Davey and P. I. Amundson)

Last Reported: ANL-7518, pp. 25-28 (Nov 1968).

a. FFTF Critical Program. The required loading changes to accommodate Assembly I of the Resumed Phase-B FFTF Critical Program for ZPPR were completed. Transformation of the reactor loading pattern from that of the previously loaded 1400-liter, UO_2-reflected core* to that of the proposed Assembly I required the removal of 4320 drawers (≈70 tons) and installation of 2101 drawers (≈11 tons) of material.

*Reference to original ZPPR Core I.

The preloaded reactor interface configuration corresponding to Assembly I is shown in Fig. I.B.9. Assembly I is to be a cylindrical critical having a core height of 36 in. and 12-in.-thick axial and radial reflectors. Cross-sectional views and corresponding nominal compositions of the core and reflector drawer cells are presented in Fig. I.B.10 and Table I.B.13, respectively.

The critical mass of Assembly I has been calculated (utilizing the calculational and experimental correlation obtained from ZPR-3 Assembly 51) to be 367 kg of fissile material ($^{239}Pu + ^{241}Pu + ^{235}U$). The corresponding total plutonium mass and core volume are 411 kg and 699 liters, respectively.

b. Doppler Effect

(i) Design. The rod and fuel-capsule container bid package has been prepared and sent to potential vendors.

(ii) Equipment. The drive mechanism has been received. The vacuum system has been assembled on the carriage and is leaktight. Integration of control circuitry into the drive system has been started.

c. Reactor Equipment Development

(i) Experimental Equipment. An in-place test of the radial perturbation sample and counter-drive mechanism has been performed with the stationary reactor half.

Mechanical and electronic adjustments have been made to the perturbation-sample changer mechanism to insure reliable operation of the stepping-motor indexer.

(ii) Automation of Data Acquisition

(a) Data Collection System. Installation and testing is continuing.

(b) Counting Room. Interfacing of the Incremental Magnetic Tape Unit with the SEL-810A computer is continuing and is approximately 60% complete.

d. Heterogeneity. Major effort has been concentrated on assembly of the components of the automated gamma-ray-spectrometry system. The general-purpose digital computer has been interfaced with an analog/digital converter for test purposes. Present efforts are centered on readout interfaces and program debugging. Micrological problems with the magnetic-tape unit have been corrected, and efforts toward interfacing with the computer continue.

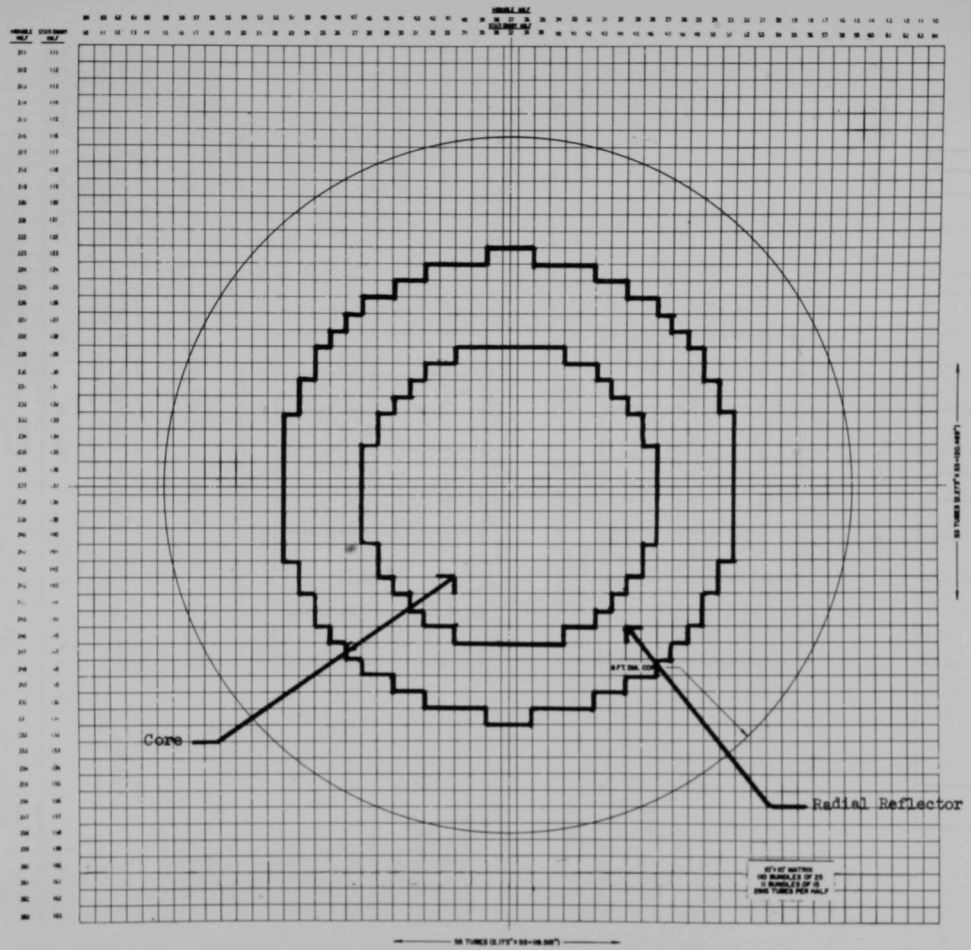

Fig. I.B.9. Preloaded Assembly-I Configuration of Resumed Phase-B FFTF Critical Program

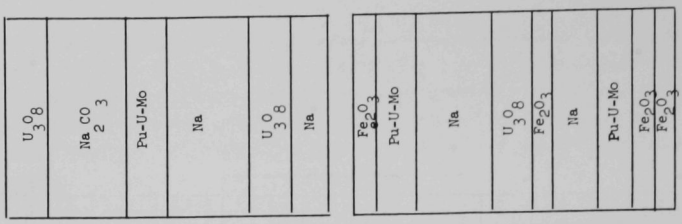

Core Two-Drawer Cell

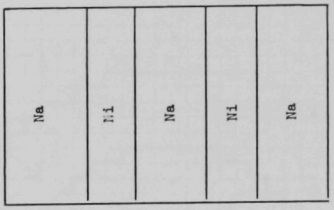

Axial Reflector Drawer Cell

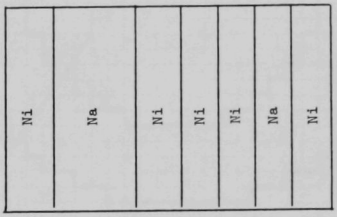

Radial Reflector Drawer Cell

Fig. I.B.10. Core and Reflector Drawer Cells

TABLE I.B.13. Nominal Compositions in Assembly I of ZPPR (atom/b-cm)

Nuclide	Core	Axial Reflector	Radial Reflector	Nuclide	Core	Axial Reflector	Radial Reflector
O	0.01442066	-	-	^{235}U	0.00001334	-	-
Na	0.00860629	0.013358	0.006495	^{238}U	0.00597782	-	-
Fe	0.01215677	0.008418	0.007163	^{239}Pu	0.00128254	-	-
Cr	0.00259267	0.002394	0.002048	^{240}Pu	0.00017469	-	-
Ni	0.00129094	0.019264	0.046215	^{241}Pu	0.00002376	-	-
Mn	0.00022017	-	-	C	0.00110393	-	-
Mo	0.00032997	-	-				

e. Preparation for Operation

(i) Reactor Control and Nuclear Instrumentation. ZPPR review of operator and supervisor qualifications for the startup team is complete.

"Prooftest" runs without fuel in the matrix continue. Long-term reliability of safety-rod static characteristics is being investigated.

6. ZPR Materials

a. Development of Fabrication Techniques (J. E. Ayer)

Last Reported: ANL-7518, pp. 28-29 (Nov 1968).

(i) Doppler Coefficient Elements. Six Doppler elements with low-density fuel columns were fabricated by loading 100% PuO_2 fuel containing 47.28 w/o ^{240}Pu into Inconel jackets.* The oxygen-to-metal ratio of the fuel particles was 1.97, and the Inconel jackets were ~2 in. long, with nominal fuel cavities that ranged from 0.500 to 0.810 in. in diameter. Two pilot elements containing 11.42 w/o ^{240}Pu were also fabricated. The loading data are shown in Table I.B.14.

TABLE I.B.14. Loading Data for $^{240}PuO_2$ Doppler Elements[a]

Element No.	^{240}Pu (w/o)	Inside Diameter (in.)	Inside Length (in.)	Fuel Wt (g)	Fuel Density (g/cm^3)	Packing Efficiency (%)
810	42.27	0.811	1.936	96.638	6.224	56.47[b]
750-1	42.27	0.751	1.937	84.567	6.341	57.54[b]
750-2	42.27	0.751	1.936	84.238	6.326	57.41[b]
690	42.27	0.691	1.937	73.699	6.442	58.46[b]
625	42.27	0.626	1.937	60.491	6.538	59.33[b]
500	42.27	0.501	1.937	38.643	6.518	59.14[b]
Pilot Capsule 1	11.42	0.810	1.812	88.405	5.78	54.84[c]
Pilot Capsule 2	11.42	0.810	1.812	87.443	5.72	54.24[c]

[a]Particles of 50-100 mesh size vibratorily compacted in Inconel jackets.
[b]Based upon pycnometer particle density of 11.02 g/cm^3.
[c]Based upon pycnometer particle density of 11.54 g/cm^3.

The six required elements had packing densities of 6.2 to 6.5 g/cm^3 and packing efficiencies of 56.5 to 59.3%, based on a pycnometric particle density of 11.02 g/cm^3. The required low-density fuel columns were obtained by vibratorily compacting 50- to 100-mesh (US sieve size) particles into the Inconel jackets. Special fixtures were required to control contamination during element compaction because the fuel was loaded

*Inconel-600 alloy has the nominal composition 70 w/o Ni, 15.8 w/o Cr, and 7.2 w/o Fe.

to within 0.100 in. of the jacket lip. After loading and preliminary decontamination, the jackets were welded, decontaminated, leakchecked with a helium mass spectrometer, and radiographed. All the elements passed the leaktests, and the contamination levels on all jackets were less than 200 d/m α/61 cm^2 of jacket surface (direct count). Radiography showed a gap of less than 0.003 in. between the fuel and the surface of the top end plug.

(ii) Oxide Plate Elements. Reactor physics information specific to oxide compositions is required for LMFBR application. These determinations will be made in ZPPR by using $(U,Pu)O_2$ fueled plates in zoned experiments. The oxide plates have geometric dimensions and tolerances similar to those of the metallic bulk-fuel plates. Two processes show promise of being applicable to the fabrication of plates: cold pressing followed by sintering, and hot pressing. Hot pressing is being considered because size and dimensional tolerances may be easier to control by this method and because the fabrication process is inherently simpler than the cold press-sinter technique.

A small-scale hot press that will be used to conduct initial studies has been installed in a nitrogen-filled glovebox in the Plutonium Fabrication Facility of Building 350. The hot press consists of a resistance furnace and a "single-acting" hydraulic press. Graphite dies and punches were used in the preliminary studies. To date, 12 runs have been made to determine the effects of pressure, time, and temperature upon the density and geometric tolerances of the resultant plates.

The process by which platelets for screening studies are made is essentially as follows. The die is loaded with 40 g of UO_2-15 w/o PuO_2 and the punches are added. The assembled die is prepressed to about 500 psig and loaded into the press in the furnace cavity where a predetermined force is exerted. The furnace is started and operated at a fixed temperature-time cycle while the pressing pressure is maintained at a constant level. The subsidence of the specimen is noted during the entire run. After the desired period of time at operating temperature has elapsed, furnace power is decreased, the die is cooled to room temperature, and the specimen is ejected.

Single and multiple plates of UO_2-15 w/o PuO_2 have been hot pressed by this technique. Both round (1 in. in diameter) and square (0.75 in. side) plates of uniform thickness have been made. The hot-pressing characteristics of UO_2-15 w/o PuO_2 have been studied in the temperature range from 1000 to 1500°C and at pressures ranging from 1280 to 5100 psig. Densities from 85.2 to 94.8% of theoretical density have resulted from hot pressing in this range. The maximum density was obtained by hot pressing at 1500°C for 30 min at 5100 psig. Thickness variations of the pressed plates were consistently within the range of ±0.0015 in. Although graphite dies were used, carbon pickup averaged under 500 ppm, with the carbon evidenced mainly near the surface of the specimen.

C. Component Development--LMFBR

1. Reactor Mechanism and Instrumentation

a. Instrumentation Development (T. P. Mulcahey)

(i) Out-of-core Neutron Flux Detection System (Intermediate Range Neutron Flux Monitor) (G. F. Popper)

Last Reported: ANL-7500, pp. 34-36 (Sept 1968).

Wide-range and intermediate-range circuits are being developed for testing with detectors installed in a special thimble in EBR-II. Environment and performance requirements for FFTF and future LMFBRs serve as development and test goals.

(a) Detectors and Cables. Although the Westinghouse high-temperature (850°F maximum) fission-counter chambers and compensated ionization chambers and mating cables were received, the detectors and cables were returned to the manufacturer so the required identification markings could be applied. Westinghouse will partially test and qualify the detectors at temperatures up to the maximum rating.

The Reuter-Stokes detectors have been fabricated, but delivery awaits cable fabrication. Arrangements are being made for Reuter-Stokes to test and qualify the detectors partially.

The Westinghouse WX-4036 fission-counter chamber attached to the Bostrad-22 cable has been installed in the EBR-II 01-thimble facility. The previously described Argonne system and the detector cable have been tested at ~120, 300, 500, and 700°F with the reactor shut down; overall system performance was satisfactory. As shown in Fig. I.C.1, data have been taken during reactor startup with the detector cable operating at 700°F. A very low gamma flux (~60 R/hr) was present, so the data show an overlap greater than two decades between the log counting channel and the true rms log channel. For comparison, Fig. I.C.1 also shows the conventional EBR-II linear flux channel.

After the test system was operated for ~1 week at 700°F, and during approach to full reactor power of 50 MWt after an unexpected shutdown, a malfunction occurred. The cause is being determined.

(b) Circuits. After the manufacturer-supplied modified bandpass amplifier circuit board for the mean-square system was installed in the Gulf General Atomic 10-decade neutron monitor, the entire system was realigned. During this realignment process, large induced-noise signals were noted in both the counting and the mean-square voltage systems, even

with the detector cable disconnected from the preamplifier. Therefore, spurious noise signals are being picked up on the signal-transmission cables between the preamplifier and the remaining electronics. This previously undetected problem is being discussed with the manufacturer; solutions to the problem are being formulated.

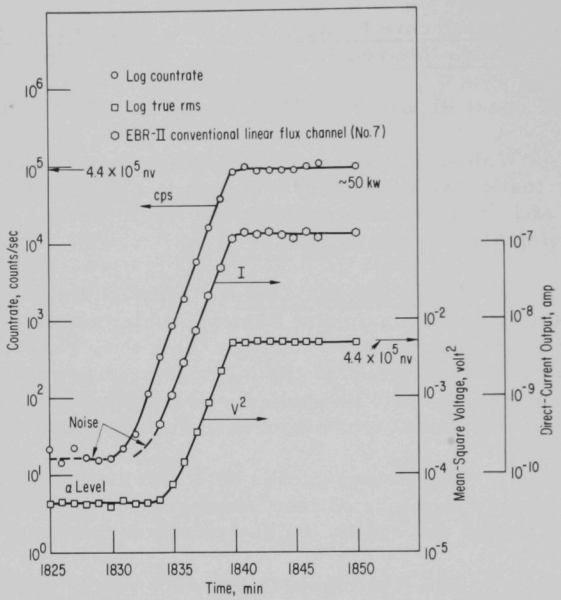

Fig. I.C.1. Response of WX-4036 Detector with Bostrad-22 Cable (at 700°F in 01 thimble of EBR-II) to Reactor Startup; Response of Conventional Channel is Shown for Comparison. Gamma flux was ~60 R/hr, chamber sensitivity: 0.21 cps/nv and 1.15 x 10^{-8} V^2/nv.

It has been determined that the 4.8-kHz clock-synchronizing signal applied to the EBR-II 115-V lines is not being induced into the Gulf system through the power supplies, so a line filter will not solve the problem. The signal is being injected into the system either through the detector-signal cable or through one of the preamplifier interconnection cables. Further analysis in underway to eliminate the noise.

A boral shield has been placed around the detector of the Gulf General Atomic system to reduce the neutron flux. While the shield was being installed, the detector and cable were disturbed, breaking the attached cables and connectors. These cables had deteriorated badly because of exposure to the EBR-II J-thimble environment for more than 135 days, during which they had accumulated an estimated dose of 1 x 10^8 rad,

which is ten times the recommended maximum dose for polyethylene cables. Therefore, the cables and connectors have been replaced with new ones. However, in the process of reinstalling the cables and flexible conduit shielding through the thimble shield plug, the electrical insulation on the shield conduit was damaged, causing an unwanted ground to the reactor. In an attempt to isolate the damaged shield conduit above reactor ground, one of the new cables opened, making the entire system inoperative. New flexible conduit shielding has been ordered; the open cable will be repaired or replaced during the next reactor shutdown.

The Milletron system is nearly ready for acceptance tests. Unexpected problems of circuit design caused the delivery delay.

b. FFTF Instrumentation (R. A. Jaross)

(i) In-core Flowmeter Development (R. A. Jaross)

Last Reported: ANL-7518, pp. 32-33 (Nov 1968).

(a) Prototype Permanent-magnet Flowmeter Tests. Flowmeter designs incorporating (a) a single cylindrical permanent magnet, and (b) two curved permanent-magnet segments with two soft-iron pole pieces are being compared for ease of assembly, availability and cost of the magnets, sensitivity, and reliability.

(b) Eddy-current Flowmeter Tests. High-temperature universal-type coils (of ~2.02-in. OD) for the 15/16-in. flowmeter that will be installed on the 15/16-in.-ID flowtube were wound with 16-mil-dia nickel-clad silver magnet wire having ceramic insulation (and supplied by Secon Metals Corp.). Five coils are required for this flowmeter. Of eight coils wound, five had short circuits because of mechanical damage to the ceramic insulation. Additional wire is being purchased so that two more acceptable coils can be produced.

A second source of supply for such magnet wire has been found; Physical Sciences Corp. can supply this wire in AWG sizes 16 to 26 (50- to 16-mil diameter) and with a temperature rating of 1000°F; inasmuch as the coils would be encapsulated in a stainless steel chamber and maintained in an inert gas atmosphere, it is possible that this wire would serve above 1000°F.

It has been determined that Sylvania Electric Products, Inc., can supply nickel-clad silver wire in AWG sizes 16 to 26.

(ii) Signal Lead Connectors for Sodium Service (A. P. Grunwald)

Last Reported: ANL-7513, p. 40 (Oct 1968).

Exposure of the four nipple connections of the FFTF prototype connector to argon at temperatures to 500°F yielded the following results: (a) the leakrates, which were monitored initially at room temperature and then continuously as the test temperature was increased, showed a definite downward trend for three nipples and a much smaller downward trend in the fourth (which is characteristic behavior for connectors of this type); (b) with each incremental increase in temperature, the leakrates change temporarily, positively for some nipples and negatively for others, with no definite pattern for any one nipple, but the temporary change disappears after the nipple has soaked a while, then resumes its regular pattern for a specific nipple; and (c) the leakrates of the four nipples with a pressure differential of 5 psi across the connection ranged from 1 to 8×10^{-3} std. cm^3/sec at room temperature and from 2 to 10×10^{-4} std. cm^3/sec at 500°F.

The connector is being tested in sodium at temperatures to 500°F.

(iii) Failed-fuel Location Method Development (E. Sowa)

Last Reported: ANL-7518, p. 33 (Nov 1968).

(a) Sodium Test Loop. All the shop-fabricated components have been delivered for installation in the loop that will be used to develop a method for detecting fission gas released from a failed fuel subassembly. The gas-disengagement chamber, pump-mounting pad, sodium-catch pan, and sampling valve were among the last units received. To expedite delivery of the sampling valve, its design was modified by substituting a weld for the seal ring at the upper part of the body.

Welding of the loop piping has begun. The return pipe, tank, and gas-disengagement section have been joined.

2. Fuel Handling, Vessels, and Internals--Core Component Test Loop (CCTL) (F. A. Smith)

Last Reported: ANL-7518, pp. 33-34 (Nov 1968).

Except for 4 hr when the pump was turned off to remove a sodium-sample tube and to replace it by welding in a new tube, the CCTL has been operating continuously during this reporting period (i.e., 620 hr out of 624 available). The loop flowrate has been a constant 400 gal/min, with a

pressure drop of 45.9 psi across the prototype FFTF fuel subassembly. During the first 12 days, the loop temperature was raised from 700 to 1060°F, at which it has been operating since; each incremental increase of 50°F was not initiated until the plugging temperature of the sodium measured less than 250°F.

To verify the adequacy of the design of the support structure for the test vessel, temperature profiles of the support stand were measured on December 11 and compared with data recorded on July 23. On both dates the CCTL was at 1060°F, flow conditions were similar, and the support stand and test-vessel pads were at equilibrium temperatures. The two sets of data agree precisely, with the insulated vessel support pad being at 800°F and the uninsulated 5.6-ft-high support stand being at an average temperature of 260°F. The support pad at the top of the test stand measured 220°F; the bottom pad of the stand, which is in contact with the floor, measured 100°F. Thus we conclude that the "Lubrite" plates between the hot-vessel-support pads and the mating-support pad of the stand are effective in providing a thermal barrier (these plates also provide for radial expansion of the test vessel).

Four sodium-vapor traps, located between the argon supply and the test vessel, expansion tank, pump free surface, and loop dump tank, have operated for a total sodium "pump-on" time of 2146.7 hr, about 60% of which has been while the loop sodium was at 1060°F. Although there has been no evidence of the vapor traps obstructing the normal flow of argon to the various loop components, temperature profiles of the traps were measured on December 15 and compared to data taken July 29. Both sets of data are identical, indicating that the vapor traps are functioning as expected and no maintenance is required. With the temperature of the sodium in the loop at 1060°F, argon enters each vapor trap at about 845°F; electrical-resistance heaters are controlled manually to maintain the argon outlet temperature at 245°F; further cooling is provided downstream toward the gas source to reduce the gas-line temperature to ambient.

D. Systems and Plant--LMFBR

1. 1000-MWe Plant

a. Contract Management, Technical Review and Evaluation (L. W. Fromm)

Last Reported: ANL-7518, pp. 34-35 (Nov 1968).

Final patent clearances have been obtained on all Task-I reports, so their publication can proceed, except for the Westinghouse Task-I report, whose editing is being completed. The Task-I reports are being printed on a schedule that will see the publication of all five completed in about two months.

The quarterly report for the period July 1 through September 30, 1968 has been compiled and edited, and is being reviewed.

(i) Babcock & Wilcox Co. Subcontract. B&W has completed its work on the follow-on study, except for editing and reproducing the Task-II and -III final report, which describes the B&W reference concept, and the Task-IV report describing the requirements for research and development.

(ii) Westinghouse Electric Corp. Subcontract. The Task-II conceptual system design descriptions of the primary and intermediate coolant systems are being typed. All Task-III parametric calculations have been completed and are being used in the Task-IV value analysis. All but two sections of the Task-IV report have been drafted. The plant availability study is nearing completion.

(iii) General Electric Co. Subcontract. The Task-II report has been completed and is being reviewed. Most of the material for the Task-III and -V reports has been drafted. Except for some safety information, all material for preparation of the Task-IV report has been collected and is being integrated into the proper report format.

(iv) Combustion Engineering, Inc., Subcontract. Work on the follow-on study has been completed, except for the editing of the Task-IV report describing the requirements for research and development.

(v) Atomics International Subcontract. Reactor-burnup analysis and plant capital cost estimates have been completed. Drafts of all the system design descriptions have been completed; those that have been reviewed are being revised. Drawings of the reactor structure and fuel subassemblies are being revised. Nuclear and thermal-hydraulic analyses of the Task-III reference reactor are being completed. Sections of the Task-III report are being drafted; sections of the Task-IV report have been drafted.

E. EBR-II

1. Research and Development

a. Reactor Experimental Support--Reactor Analysis and Testing (R. R. Smith)

Last Reported: ANL-7518, pp. 36-39 (Nov 1968).

(i) Nuclear Analysis and Safety

(a) Exposed-fuel Calibration Studies in EBR-II. Under normal operating conditions, small quantities of fission products are generated from fuel material contaminating the surfaces of core components.

Consequently, all EBR-II fission-product monitoring systems always register signals. These signals are proportional to the concentrations of specific index species in the primary coolant or cover gas.

When exposed fuel is introduced into the core, the signals of all the monitoring systems increase. Defining the unavoidable response from fuel contamination as "noise" and the increase in response caused by the exposed fuel as "signal," the signal-to-noise ratios (S/N) for all index species (thus, for all monitoring systems) is the same, regardless of the time-power operational history of the reactor.

A useful parameter in diagnosing the nature and magnitude of a fuel failure is the S/N ratio associated with a single unclad driver element. In recent studies, two unclad Mark-IA driver elements, located in a special control rod, were installed in the core. Measurements of the responses of all fission-product monitoring systems before and after the insertion of the exposed fuel led to values for the S/N ratios of the various monitoring systems.

Prior to the installation of the special control rod, the reactor was operated continuously for nine days at 50 MWt. During this time, noise levels were established for all monitoring systems. Then the reactor was shut down, the special control rod was fully inserted, and the power level was raised to 50 MWt. The FERD (fuel-element-rupture detector) and FGM (fission gas monitor) systems reached equilibrium during subsequent operation of the reactor for 53 hr at 50 MWt. The equilibrium level for ^{135}Xe was not completely reached by the end of the 53-hr test; the degree of saturation (0.945) at this point was used to adjust the measured level to the equilibrium value.

The results of the tests indicated the following S/N ratios for a single unclad pin: for the FGM, 4.3; for the FERD system, an average of 3.6 for the three channels; and for the ^{135}Xe in the cover gas, 1.45. From analyses of primary-sodium samples taken before and at the end of the tests, the S/N ratio for ^{131}I was found to be 1.40.

The much lower values of the S/N ratios for ^{135}Xe and ^{131}I suggest either of the following possibilities: an unduly low value for the ^{135}Xe and ^{131}I signals, or the use of unduly large values for the respective noise contributions. The latter possibility appears to be the most logical because it is more consistent with the observations of September 9 and 10 (see Progress Report for September 1968, ANL-7500, pp. 44-47) when it was noted that the levels of ^{135}Xe and ^{131}I increased by factors of approximately two. Because no increase was then noted in the responses of the FGM and FERD systems, the increase in ^{131}I and ^{135}Xe activities was postulated to be the result of the slow extrusion of sodium bond through a cladding defect. For such a failure mode, fission-product

gases cannot escape. Insofar as the existing monitoring systems are concerned, the only significant release of fission products to the primary coolant involves the longer-lived iodine species. The shorter-lived iodine and bromine species, which are sensed by the FGM and FERD systems, decay before they can migrate from their place of birth to the defect. Longer-lived species such as ^{131}I and ^{135}I (the parent of ^{135}Xe) live long enough to negotiate the defect.

Cladding penetration involving the slow extrusion of bond sodium qualitatively accounts for the differences noted in the S/N ratios for the various monitoring systems. If the pre-September 9 values for the noise levels of ^{131}I and ^{135}Xe are used (rather than the values established immediately prior to the tests), the S/N ratios for ^{131}I and ^{135}Xe become approximately four, values in excellent agreement with those measured for the FERD and FGM systems. Such evidence was used to conclude that the source of fission-product release, first suspected on September 9, was still in the core.

(b) Origin of the September 9 Fission-product Release. Throughout the remainder of Run 30 and during Runs 31 and 32, attempts were made to locate the September 9 source of fission-product release by removing groups of suspects and using the reactor as a leak detector. Eventually, all of the standard driver subassemblies and fueled experiments that had been in the reactor at the time of the September 9 release had been removed and tested, but the source of the release was not found. Then, the control rods were checked by withdrawing each rod completely, one at a time, for approximately 50 MWd of reactor operation while measuring the saturated ^{135}Xe activity in the cover gas. On December 8, a decrease in the ^{135}Xe activity was noted when the last control rod (L-462) was withdrawn from the core. Reinsertion of the rod resulted in an increase, and a final withdrawal caused a decrease from the fully inserted level of 7.0×10^{-3} to 4.5×10^{-3} μCi/ml. Since the signal associated with the September 9 release was estimated to be 3.5 μCi/ml, and since the power generation of a fully withdrawn control rod is half that of a fully inserted rod, the magnitude of the decrease is consistent with other experimental information. Accordingly, control rod L-462 was removed from the core and will be inspected in the FCF.

(c) Mark-IIA Safety Analysis (J. R. Trinko)

A code for computing fuel-temperature coefficients for 20 hypothetical Mark-IIA core loadings was written and debugged. As a test case, the temperature coefficient of EBR-II Run 30 was calculated to be -4.1×10^{-6} $\Delta k/k/^{\circ}F$, a value which compares favorably with the value of -4.8×10^{-6} $\Delta k/k/^{\circ}F$ inferred from experimental work conducted during Run 25. The calculation is based on spherical reactor geometry.

The sensitivity of the spherical model to blanket composition was explored with the following k calculations for a critical 91-subassembly Mark-II core:

Blanket Composition	$\underline{k}$ (10^{-5} convergence)
Depleted U (^{238}U only)*	0.99908
0.2 a/o ^{235}U added to inner blanket	1.00150
0.2 a/o ^{235}U added to inner and outer blankets	1.00250
Stainless steel inner reflector**	1.03153
Nickel inner reflector**	1.04936
Stainless steel upper reflector (without gap) replacing inner and outer blankets	1.01227
Stainless steel upper reflector with 4.37-in. gap replacing inner and outer blankets†	0.97660

It is apparent that the gap is significant in spherical calculations.

(d) Code for Converting Ih to Reactivity Units (J. R. Trinko)

A code was written for computing the factor for converting from inhours (Ih) to reactivity units ($\Delta k/k$) and for assessing the uncertainty resulting from the uncertainties in the delayed-neutron fractions β_i and the decay constants λ_i. For the wet critical EBR-II core, a value of 413 ± 13 Ih/$\Delta k/k$ was obtained (this value compares favorably with the 415 Ih reported in ANL-5800). Thus, for a ^{235}U-fueled reactor, the uncertainty amounts to approximately 3%.

(ii) Higher Power Operation

(a) Nickel Reflector (R. A. Cushman)

The temperature distribution in the proposed nickel reflector subassembly has been calculated for core positions 7N4 and 8N4 at 50-MWt reactor operation. The results of the calculations indicate that a properly orificed nickel reflector will have acceptable thermal characteristics. The maximum temperature difference from the center to the edge of a $1\frac{7}{8}$-in.-dia nickel cylinder in Row 7 was calculated to be less than 40°F, and the maximum temperature difference from one side of the subassembly hex can to the other was calculated to be less than 10°F.

*Appropriate amounts of sodium and stainless steel were included.

**Appropriate amount of sodium was included.

†Gap contains sodium (53.3 v/o), stainless steel (29.8 v/o), and void.

The calculations were carried out with the THTB program. An additional program (BLANKSUB) was written and used to determine the volumetric heat generation at the nodal mesh points used in the THTB program. The calculational procedure has been automated to permit rapid determination of temperature distributions in a modified-geometry subassembly or with varied axial and radial heat-generation rates.

b. Nuclear Analysis Methods Development

Last Reported: ANL-7518, pp. 39-41 (Nov 1968).

(i) Oxide Driver Core. One-dimensional diffusion-theory modeling techniques were studied, using the preliminary conceptual design of the oxide core and the six-group cross-section set 23806 as a basis of comparison. In the first technique--based on the self-consistent diffusion theory (SCDT)--the group-independent transverse bucklings that gave the same critical composition for both the axial- and radial-geometry representations of the reactor were determined. The second technique was based upon iteration of group-dependent transverse bucklings in the core to a consistent core composition. The second technique was compared with the first by doing a series of iterative calculations to converge on k_{eff} for the critical composition predicted by the SCDT model. When transverse bucklings in the core were used to represent transverse leakage in all regions, k_{eff} was found to converge to 1.0888 (within 0.001) after six iterations. This high value of k_{eff} indicates that the method as used initially underpredicted transverse leakage in regions outside the core.

The procedure was repeated, using appropriate group-dependent core bucklings in core regions as before, but using the simple group-independent formulations

$$b_r^2 = \left(\frac{2.4048}{R_{ext}}\right)^2 \text{ and } b_z^2 = \left(\frac{\pi}{H_{ext}}\right)^2$$

in all other regions. Here k_{eff} converge to 0.9982 (within 0.0009) in five iterations.

A corresponding k calculation based on two-dimensional diffusion theory and using the DIF2D code gave k_{eff} = 1.0335. This larger value is ascribed to differences in corner representations in the one- and two-dimensional models. Further comparisons were made between the SCDT modified group-dependent transverse bucklings and the two-dimensional results with regard to the median energies for source, absorption and flux, and group-4 spatial distribution of flux. The modified group-dependent method was concluded to be the most accurate and easiest to use for the initial neutronics scoping calculations for the oxide core.

Information on power distribution obtained in the foregoing work will be used in making a thermal-hydraulic analysis of the initial design.

(ii) DSN Methods. Implementation of the DSN numerical method for the IBM-360 Model-75 computer was continued with further testing of the DOT program. Comparison of the running times for a typical EBR-II analysis problem (6 groups, S_2, 1196 mesh points) indicated that calculation with the DOT code on the IBM-360 is $3\frac{1}{2}$ times faster than calculation with the SNARG-2D code on the CDC-3600.

To facilitate the use of available codes for group cross-section generation and data handling with the DOT and ANISN programs, a code was written for the CDC-160A to accept cross sections in the XLIBIT format from either cards or magnetic tape, and to punch the cross sections on cards in the DOT and ANISN input format.

(iii) Evaluation of Cross-section Sets. An effort has been initiated to generate a new cross-section set for analyzing the physics of EBR-II utilizing the point cross-section data from Evaluated Nuclear Data File B (ENDF/B) as well as from other later measurements. Analysis is being made of the physics measurements of some ZPR-3 critical assemblies (e.g., Assemblies 2, 5, and 6F) similar in composition and size to the EBR-II. The EBR-II mockup and wet-critical experiments also will be analyzed. The calculated physics parameters will be compared using the new cross sections and the present cross-section sets 238 and 23806.

A new cross-section set is also being generated using the ZPR-3 Assembly 46C (FARET oxide core) as a model. This assembly is similar in size and composition to the preliminary conceptual design of the EBR-II oxide core.

(iv) Study of Nickel Reflector

(a) Calculations of Gamma-ray Heating. The distribution of the gamma-ray heating must be known for designing the nickel reflector for the inner radial blanket of EBR-II. Attempts have been made to obtain the data by using the MAC code,* which was developed for calculating shielding requirements of thermal reactors rather than for gamma heating adjacent to the core of a fast reactor. With the MAC code, the neutron flux in regions outside the core is first calculated using a combination of removal and diffusion theories; then, the gamma-ray flux is calculated from the gamma-ray sources produced by fission in the core and capture of neutrons outside the core.

*Peterson, E. G., MAC--A Bulk Shielding Code, HW-73381 (April 1962).

The magnitude and slope of the neutron flux at the core-blanket interface are used as input to calculate the neutron flux in the blanket and shielding regions. In this calculation, the neutron flux and power distribution are taken to be linear with distance within the core, and fission outside the core is not considered. A 31-group flux is obtained for noncore regions in which inelastic scattering occurs only in the first six groups and in which the neutrons may downscatter a maximum of six groups.

The gamma-ray flux is obtained with removal theory (using correction factors for buildup) for one-dimensional slab geometries. Production of gamma rays is calculated from core fissions and neutron captures outside the core. The fission density and the slope of the flux at the core-blanket interface are used to obtain the gamma-ray production from fissions.

Because of the orientation of the MAC code to thermal reactors, many neutron-capture cross sections at high energies are given as zero in the code. The code also assumes that the energy distribution of the gamma rays produced by neutron capture is independent of the incident energy of the neutron, and it ignores production of gamma rays by inelastic scattering. A seven-group energy structure is used by the code with all gamma rays of 1 MeV or less contained in the seventh group. A finer division of gamma-ray energy of 1 MeV and less is desirable for calculating the distribution of gamma-ray heating.

Transport-theory calculations (see Progress Report for August 1968, ANL-7487, p. 42) were performed to obtain the neutron-flux quantities used as input for the MAC code. The model for EBR-II was a sphere with a core composition similar to that used in Run 27A (i.e., a steel reflector in Rows 7 and 8, and a depleted-uranium blanket in Rows 9 through 15). The heating rates in iron calculated with the code are compared with the rates obtained by other sources in Fig. I.E.1. Considering the weakness of the MAC code for calculating gamma-ray heating in regions adjacent to cores of fast reactors, the close agreement of the results is surprising. However, a high degree of confidence in the heating rates is required for designing a nickel reflector. Therefore, efforts have been initiated to develop a code for calculating gamma-ray flux from transport theory rather than from diffusion or removal theory.

(b) Worth of Reflector Materials. Three reactor configurations, each with a core loading and outer blanket identical to those of Run 27A but with different materials in the inner blanket, were studied to determine the worths of different reflector materials. The materials and their approximate compositions (placed in Rows 7 and 8 for the investigation) were: (1) depleted-uranium blanket (60% ^{238}U, 20% steel, 20% sodium); (2) steel (80% steel, 20% sodium); and (3) nickel (80% nickel, 20% sodium). The values of k_{eff} were obtained from second-order SNARG-2D calculations in R-Z geometry and six energy groups. The calculated worths are given in Table I.E.1.

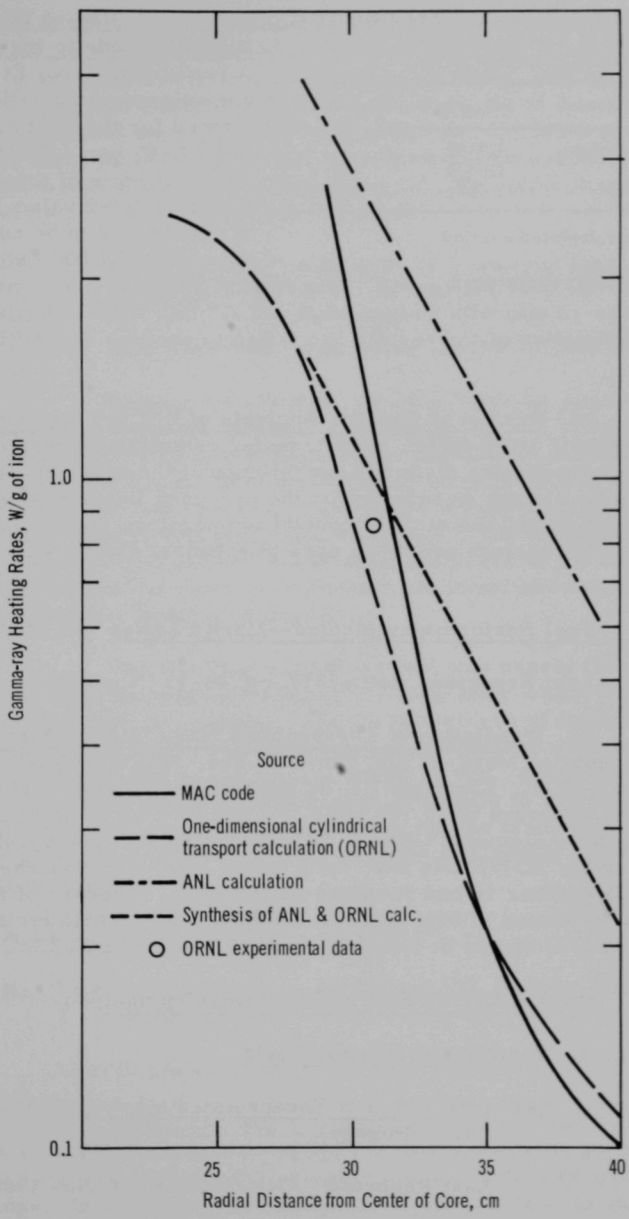

Fig. I.E.1. Radial Gamma-ray Heating Rates in Iron Obtained by Various Sources

TABLE I.E.1. Calculated Reactivity Worths of Various Materials in Radial Reflector Region

Reflector Material	k_{eff}	$\Delta k/k^a$ (%)
Depleted Uranium	1.0187	-
Steel	1.0369	1.8
Nickel	1.0891	6.9

[a]Compared to depleted uranium.

(v) Use of Two-dimensional Diffusion Code in the ARC System. A two-dimensional (R-Z) flux-convergence calculation was performed for the loading of Run 27A in EBR-II, using the diffusion-theory module of the ARC system. The calculated value 1.001 for k is considered to be consistent with the value of 1.037 calculated with the SNARG-2D code with n = 2. The running time for a k convergence of 3×10^{-9} was 12 min with no input flux and 7.5 min with an initial flux. Initial examination of the results has failed to uncover any difficulties with the code.

(vi) Review of Hazards Analysis of UNC 19 Experimental (UPu)C-fueled EBR-II Rods. Heat-transfer calculations were made to determine temperature distributions throughout the encapsulated subassembly. The calculations were based on the proposed linear heat-generation rate of 15 kW/ft and the allowed coolant temperature rise of 130°C. The resulting temperatures are being used to estimate stresses in the cladding wall.

c. Fuel Performance Studies--Mark I Series (C. M. Walter)

Last Reported: ANL-7518, pp. 41-43 (Nov 1968).

(i) Irradiation of Encapsulated Mark IA Fuel Elements. Five encapsulated Mark-IA fuel elements are being irradiated to high burnups in EBR-II. Elements BF-02 and BF-03 (in Subassembly XO15) had received an exposure of 10,158 MWd (3.2 a/o burnup) as of December 16. The other three elements (BF-04, BF-08, and BF-11, previously irradiated in Subassembly XO17) have been returned to EBR-II in Subassembly XO52, and as of December 16 had received an additional exposure of 840 MWd and a total exposure of 8060 MWd (2.8 a/o burnup). Tentative target burnup for XO52 (3 a/o) should be reached during EBR-II Run 33.

d. Mark II Driver Fuel Element Development

(i) Element Irradiation Tests

(a) Irradiation of Encapsulated Mark-II Fuel Elements (M. A. Pugacz)

Last Reported: ANL-7518, p. 44 (Nov 1968).

Three of the 37 capsules removed from experimental Subassembly XO29 at the end of Run 30 are being destructively examined.

The remaining 34 capsules, irradiated to a maximum burnup of approximately 2.4 a/o in XO29, were reassembled in their original positions along with three replacement capsules in a new subassembly designated as XO53 and returned to the original position 4E3 in the reactor. As of December 10, Subassembly XO53 had been exposed to an additional 669 MWd of operation for a total exposure of 4807 MWd. Calculated maximum burnups were in the range from 2.2 to 2.8 a/o as of December 10. Tentative target burnup (4 a/o) should be reached during EBR-II Run 34.

(b) Encapsulated Irradiations of Prototype Mark-II Elements in CP-5 (W. N. Beck)

Last Reported: ANL-7518, pp. 43-44 (Nov 1968).

Capsule CP-59 was removed from the reactor December 16. As of that date, the three prototype Mark-II elements in the capsule had been irradiated at a maximum clad temperature of 610°C to a calculated burnup of 2.8 a/o. In this instrumented experiment, the thermal conductivity of the fuel was found to have decreased approximately 59% when the fuel had expanded to the inside diameter of the cladding. The temperature reduction following the fission-gas release in the experiment supported the premise that sodium infiltrates the interlinked porosity, thereby improving the thermal conductivity.

The swelling rate of the fuel was nearly linear until the fuel volume had increased approximately 20%, after which it followed a typical breakaway swelling curve. The initial release of fission gas to the plenum was rapid, and the quantity released coincided with previously determined values for fuel which had expanded 33 v/o. After the release of the fission gas, the plenum pressure rose gradually to 150 psia, at which point an unexplained system malfunction rendered the transducer inoperative. The samples in Capsule CP-59, as well as those in Capsule CP-58, will be destructively examined.

e. Equipment--Fuel Related (E. Hutter)

(i) New Control Rod Subassemblies (O. S. Seim and T. E. Sullivan)

Last Reported: ANL-7518, pp. 44-45 (Nov 1968).

(a) Increased-worth Control Rod. Previously conducted flow tests of a Model IHE control rod with the upper shielding piece removed and replaced with the B_4C-cluster mockup indicated excessive pressure drops. In an attempt to reduce the pressure drop to an acceptable level, the lower shield piece was redesigned. Flow tests of the rod containing the redesigned shield piece revealed a significant reduction in pressure drop.

Additional experimental designs are being made to reduce pressure drops further; one design will incorporate a pressure-drop recovery feature in the B_4C capsules. These experimental designs will be tested to ascertain their predicted effectiveness.

After an adequately low internal pressure drop of the coolant has been achieved, the orificing system at the control-rod inlet will be designed to provide the desired specific flow value and the necessary flow variation with rod lift.

(ii) Oscillator Rod--Mark II (O. S. Seim, J. A. Pardini, and T. E. Sullivan)

Last Reported: ANL-7513, p. 57 (Oct 1968).

The detailed drawings for fabricating the modified oscillator-rod drive have been completed and are ready for checking.

Fabrication of the Mark-IIB oscillator rod is approximately 95% complete. The rod will be flowtested in a water loop when completed.

Tests of the partially completed adapter sleeve for the oscillator-rod storage basket and of the sleeve-handling tool revealed that the handling tool did not consistently engage the adapter sleeve because of binding of the fingers on the indexing barrel. The handling tool is being revised to provide a more positive engagement. Drawings of the revisions are complete, and the revised components are being fabricated.

The components of the sodium-test fixture have been fabricated, and the fixture is being assembled.

f. New Subassemblies Design and Experimental Support (E. Hutter)

(i) Irradiation Subassemblies (O. S. Seim and W. R. Ware)

Last Reported: ANL-7518, pp. 45-46 (Nov 1968).

(a) Mark B. A variation of the standard Mark-B-61 subassembly is being designed to accept a new mixed-oxide fuel element proposed by Pacific Northwest Laboratory (PNL) for use in the FFTF program.

The present Mark-B-61 accepts 61 elements, each $60\frac{7}{8}$ in. long and 0.220 in. in diameter. These elements are wrapped with a 0.052-in.-dia helical spacer wire on a 6-in. pitch. The new subassembly (the Mark B-61A) will contain 61 elements of the same length but 0.230 in. in diameter and wrapped with a 0.040-in.-dia helical spacer wire on a

12-in. pitch. When these elements are installed on a standard B-61 grid, they will provide 0.002 in. more growth space between elements in the bundle. This additional clearance has been requested by PNL and RDT to accommodate the anticipated swelling of these elements during long-term irradiations. After periodic interim examinations, these elements may have to be reassembled into a standard-sized hexagonal can for further irradiation. Assuming an anticipated swelling of 1.5% for the Type 304 stainless steel tubing of the element, remote reassembly of the elements would be difficult without the additional 0.002-in. growth space.

The effects of the additional initial clearance in the element bundle cannot be clearly defined, and ways to provide a nominal clearance and yet permit easy reassembly are being studied. One concept being investigated would indent the sides of the outer hex can with hash-mark indentations similar to those now used on several other types of subassemblies. These hash marks could be located above and below the region of expected swelling (the core region). This concept would provide reasonable support and good damping to the element bundle without interfering with reassembly operations.

(b) Mark-E-37. Hydraulic flowtests of the Mark-E-37 subassembly were performed to determine the pressure drop versus flow characteristics. The tests were made in the stainless steel pressurized-water loop, and data were collected for reactor row positions 1 through 5. The data obtained from the tests, based on a reference 67-subassembly core, are presented in Table I.E.2; Table I.E.3 shows the standard reference flow versus pressure drop values for a standard EBR-II core subassembly.

TABLE I.E.2. Results of Flowtest of Mark-E-37 Irradiation Subassembly

Reactor Row	Effective Pressure Drop (psi)	Sodium Flowrate at 800°F (gpm)
1, 2	38	93
3	39	88
4	34.5	72
5	34	63

TABLE I.E.3. Reference Flow versus Pressure-drop Values for EBR-II Standard Core Subassembly

Reactor Row	Effective Pressure Drop (psi)	Sodium Flowrate at 800°F (gpm)
1, 2	38	139
3	39	123
4	34.5	93.5
5	34	78

A separate test was made of the subassembly in Row 5 position and without the screen-type top collector. The results indicated that the pressure drop through the collector is approximately 1 psi; this is considered to be satisfactory.

(c) Mark-E-61. Further modifications were made to lower the pressure drop through the Mark-E-61 subassembly and to increase the integrity of the lower collector section. The previous designs of the Mark-E-61 employed the standard STB (stainless-triflute-blanket) shield pieces above and below the core region. This type of shield piece

has been replaced with the SCPS (stainless central-plug shield) type of shield pieces to lower the pressure drop of the coolant through the subassembly and to improve the shielding slightly. The configuration of the SCPS shield also allows the lower collector to be made integral with the shield, thus providing a thicker wall section to contain any debris and to eliminate the possibility that this debris may contact the outer wall of the hex can.

Additional alternatives of the Mark-E, to test 0.174-in.-OD metallic-fuel elements in bundles of 19 and 37, are being considered. These smaller-sized arrays will require extensive redesign of the present 61-element concept.

g. Instrumented Subassembly (E. Hutter)

Last Reported: ANL-7518, pp. 47-48 (Nov 1968).

(i) Research and Development (A. Smaardyk and H. H. Hooker)

(a) Prototype Fuel-pin Thermocouples (A. E. Knox)

Delivery of the additional thoria insulators required for making more than nine thermocouples (seven for the subassembly plus two spares) is expected in mid-February.

A representative hermetic seal was found to be leak-tight after being internally pressurized to a 135-psi differential pressure at 1150°F. The seals have been deemed suitable for the instrumented sub-subassembly.

The status of thermocouple fabrication is as follows: All adapters have been fabricated, and all Kovar tubes have been welded to hermetic seals and leaktested. All W-3% Re/W-25% Re wires have been prepared and are being junctioned. Machining of the alumina insulators to be used in the hermetic seals is approximately 60% complete. All fixtures required for fabricating the thermocouples have been completed. All of these fixtures have been tested, except the fixture for brazing the Type 308L stainless steel and Alumel wires into the hermetic seals, and proved satisfactory. The brazing fixture is being tested. Thermocouple assembly will begin when enough usable tantalum tubing is available. Eddy-current testing of this tubing is nearly complete.

(b) Coolant and Clad Thermocouples. All thermocouples from one of the two vendors have been delivered. The second vendor has partially completed delivery.

(c) Plant Modification Document--Electrical Installation Notes (W. M. Thompson)

The Electrical Installation Notes for the Plant Modification Document have been completed and are being reviewed. These notes contain the complete instructions for incorporating the control and interlocking functions of the drive system of the instrumented subassembly into the fuel-handling control system. They include wiring and cabling diagrams, sketches showing the changes and additions to be made in the fuel-handling console, and an overall schematic.

(d) Temporary Control Console (W. M. Thompson)

The temporary control console for the instrumented subassembly has been built, wired, and tested. The various electrical components of the mechanism have been fitted and wired, and the temporary electrical connections to the console have been made. The console was used before and during the December 16-17 "rehearsal test," and performed successfully in all of its functions.

(e) Rehearsal Test. A "rehearsal test" of the instrumented subassembly system was conducted on December 16 and 17 to verify fit and operation of various components.

The drive system (consisting of the center-column extension, the guide track, the elevator assembly, force switches, etc.) was installed in the reactor mockup during the week prior to the test. An electrical control console was fabricated and connected to the drive system to regulate the raising and lowering operations. The system was wired so that signals from the load-sensing devices and limit switches of the drive system would trigger shut-off responses in the control console (similar to the responses in the actual operation).

The instrumented subassembly package (consisting of the subassembly, the extension tube, and the terminal box) for the rehearsal test was constructed and assembled according to procedures being used in constructing the instrumented subassembly package for Test I. Twenty-two leads extended from the subassembly, three of which were from instrument thermocouples. These thermocouples were checked for electrical continuity and resistance, and remained intact and operable throughout the assembly and installation operations.

The instrumented subassembly package was brought to the full-scale reactor mockup in Building 331 at ANL in the same shipping container that will be used to ship this equipment to Idaho. The shipping container was brought into the building in the horizontal position, raised to the vertical position, and inserted into a well constructed to support the shipping container in the vertical position.

The package was removed from the shipping container, inserted into the mockup of the control-rod penetration, and attached to the drive system. This installation was accomplished according to the "Installation Procedures for EBR-II Instrumented Subassembly Prototype (12/3/68)." The terminal box on the instrumented subassembly package was charged with helium to 15 psig. There was no perceptible pressure drop after 30 hr; this verifies the leaktightness of the box.

The subassembly was driven to the full-up and full-down positions several times to check the engagement of the full-up and full-down interlock yokes, the actuation of the limit switches, and the action of the drive unit. The frictional resistance to the vertical drive measured 30 to 90 lb, and the load-sensing devices were adjusted to be sensitive to resistance forces in excess of 90 lb. The drive system operated satisfactorily.

The subassembly was then disassembled. The extension tube was uncoupled from the subassembly, the coupling was removed, and the lead-cutting tool was inserted into the extension tube and connected to the drive system of the tool. The drive motor was energized and the lead-cutting operation was performed while the current of the drive motor of the cutting tool was monitored and recorded on a strip-chart. Cutting was indicated on the strip-chart record by current peaks. Because of the additional friction caused by the large number of leads being cut, the peaks were not finite enough to indicate clearly each separate lead cut; however, completion of the lead-cutting operation was clearly indicated. After the leads had been severed, the lead-cutting tool and the extension piece were removed from the mockup according to the "Removal Procedure for the EBR-II Instrumented Subassembly Prototype (12/3/68)."

The rehearsal test was performed without difficulty. All of the equipment functioned properly, and the instrumentation remained operable throughout the test.

h. Packaged Loop (R. E. Rice)

Last Reported: ANL-7513, pp. 67-71 (Oct 1968).

The literature is being searched to determine the present state-of-the-art of the annular-linear-induction (Einstein-Szilard type) pump. Preliminary design calculations are being made for a small-diameter, high-temperature pump that would fit within the loop thimble.

Heat-transfer calculations are being made for a packaged sodium loop with an internal pump arrangement. Loop heat would be rejected as much as possible to the reactor coolant in the reactor outlet plenum and to the bulk sodium above the vessel cover to cool the loop sodium before it reaches the pump. The remaining heat would be rejected

to the reactor coolant flowing through the test thimble. A calculation using the HECTIC code was completed for the temperature distribution and pressure drop in the fuel and blanket sections.

The problem of providing the necessary radiation protection for personnel during the removal of a complete packaged loop has been re-examined. Distance and portable personnel shielding still appear to offer the most feasible protection during this infrequent operation.

A survey is being continued to find available high-temperature, high-strength steels that might be used in place of stainless steel in the packaged loop. If safety studies require a system design pressure higher than 1000 psig, it may be necessary to use a steel with higher strength or higher thermal conductivity, or both.

A brief look was taken at the possibility of combining the functions of a nonfueled packaged loop with the functions of an in-core instrument test facility. Tentative conclusions are: (a) it would be feasible to combine these functions so long as the instruments to be tested and the material samples are small in diameter; and (b) the design and operating problems with such a loop would be somewhat less than those with a fueled packaged loop. However, the programmatic justification for such a dual-purpose loop is not clear. A memorandum was sent to the LMFBR Program Office requesting their opinion on possible need for such a dual-purpose facility.

i. Process Chemistry (D. W. Cissel)

Last Reported: ANL-7518, pp. 48-49 (Nov 1968).

(i) Sodium Coolant Quality Monitoring and Control (W. H. Olson, C. C. Miles, E. R. Ebersole, and G. O. Haroldsen)

(a) Primary Sodium

(1) Sampling. The new purification-loop sampling system was filled with sodium and checked out. Flowmeters were calibrated by measuring the time required to fill a tank of known volume. A new "overflow" type of sampler, designed to fill four beakers or crucibles simultaneously, was successfully tested. Sodium which overflows the beakers during flushing is returned to the purification system rather than being dumped to a waste tank as it was in the old sampling system. Other improvements over the old sampling system are:

(a) sample lines tap directly off the purification lines at the inlet and outlet of the cold trap rather than off the lines of the plugging indicator;

(b) a small EM pump is provided to ensure flow through the sample loop when the pressure drop across the cold trap is not sufficient to drive the flow through the sampling system;

(c) the sampling system is automatically shut down and isolated from the purification system by signals from leak detectors on valves and samplers or from a high-sodium-level detector in the overflow sampler.

(2) Radionuclides. The results of analysis for ^{131}I in two samples of primary sodium are listed in Table I.E.4.

TABLE I.E.4. ^{131}I in Primary Sodium

Sample Date	Results Corrected to	^{131}I ($\mu Ci/g$)
11/14/68	11/14/68	6.75×10^{-4}
11/18/68	11/18/68	1.12×10^{-3}

(3) Trace Metals. A sample of primary sodium taken on November 8, 1968, was analyzed for some trace metal impurities by atomic absorption spectrophotometry. Results of the analysis are given in Table I.E.5.

TABLE I.E.5. Trace Metal Impurities in Primary Sodium

Metal	Concentration (ppm)	Metal	Concentration (ppm)
Bi	1.5	Pb	11.1
Cd	<0.05	Sn	19.3
Cu	0.5		

The distillation of sodium spiked with radiotracers of zinc-65, cadmium-109, iron-59, and tin-113 was studied. The results show that 99.5% of the zinc and 88% of the cadmium were codistilled with sodium. No loss of iron and tin activities was observed.

A titanium burner has been made for the atomic absorption spectrophotometer to provide a reliable determination of iron. A heated titanium aspiration chamber is being incorporated into the burner system to study the improvement in the sensitivity of the atomic absorption due to hot aspiration of solution.

The increase in the sensitivity of the atomic absorption of metal oxinates in the MIBK phase is under study. Data for the oxine-MIBK extraction system are lacking, and extraction of varying amounts of water into the MIBK phase might affect the reproducibility of results. A preliminary oxine-chloroform extraction is being studied for preparing metal oxinates in MIBK phase.

(4) Oxygen. Prior to placing the new cold trap into service, two samples of primary sodium were taken and analyzed for oxygen content by the mercury amalgamation method. One sample was taken in an extrusion vessel and the other in 1/2-in. stainless steel tubing. Results of the analyses are shown in Table I.E.6. The plugging temperature of the primary sodium was in the range 260-280°F when these samples were taken.

TABLE I.E.6. Oxygen Content of Primary Sodium

Sample Date	Container	No. of Aliquots	Oxygen (ppm)
11/25/68	Extrusion Vessel	5	6.6 ± 2.0
11/25/68	Tube	4	6.1 ± 1.2

(5) Carbon. A sample of primary sodium taken November 25, 1968, was analyzed for carbon by the oxyacidic flux method. The average carbon content in three aliquots was 1.96 ± 1.0 ppm.

(6) Uranium. A 10-g sample of primary sodium was taken in a high-purity tantalum cup on December 13, 1968. The sodium was removed from the sample by vacuum distillation, and uranium in the distillation residue was determined by a sodium fluoride fluorimetric method. The analysis showed that the concentration of uranium in the sodium was less than 0.2 ppb.

(b) Secondary Sodium

(1) Trace Metals. A sample of secondary sodium taken December 3, 1968, was analyzed for trace metal impurities. Results are listed in Table I.E.7.

TABLE I.E.7. Trace Metal Impurities in Secondary Sodium

Metal	Concentration (ppm)	Metal	Concentration (ppm)
Al	1.0	Fe	0.25
Bi	<0.1	Mn	<0.016
Cd	<0.025	Ni	<0.08
Co	<0.07	Pb	0.8
Cr	<0.04	Sn	<1.0
Cu	<0.03		

(2) Oxygen. Results of analysis for oxygen in secondary sodium by mercury amalgamation are listed in Table I.E.8.

TABLE I.E.8. Oxygen Content of Secondary Sodium

Sample Date	Container	No. of Aliquots	Oxygen (ppm)
10/25/68	Extrusion Vessel	2	4.1 ± 0.5
10/25/68	Extrusion Vessel	4	6.0 ± 1.6
10/25/68	Extrusion Vessel	3	6.1 ± 2.3
11/18/68	Extrusion Vessel	3	5.2 ± 2.8
11/18/68	3/8-in. SS Tube	3	12.7 ± 0.7

(3) Carbon. Recovery tests using the oxyacidic flux method are being continued for different carbon compounds. Four carbides have been purchased from Consolidated Astronautics, Long Island City, New York. Information furnished by the vendor follows:

Carbide	Composition
Boron Carbide	B--77%; C--21%
Chromium Carbide	Cr--86.2%; C--13%
Silicon Carbide	Si--70.0%; C--29.9%; free C--0.6%
Zirconium Carbide	Zr--87%; C--11.5%

The zirconium carbide was chosen for the first recovery tests because it contains the lowest fraction of carbon. Weighing errors thus translate into considerably smaller errors in the computed amount of carbon. Using a Cahn Electrobalance, microgram quantities of zirconium carbide were weighed into preignited quartz vials. These samples were then combusted in the $K_2Cr_2O_7$ flux without sodium. Table I.E.9 gives the results of the first three tests.

TABLE I.E.9. Carbon-recovery Tests Using Zirconium Carbide (Sodium Absent)

Amount ZrC Weighed In (μg)	Computed Carbon Present (μg)	Amount Carbon Recovered (μg)	Recovery (%)
840	96.6	95	97.4
501	57.6	57	98.2
541	62.2	65	103.0
		Mean Recovery	99.5 ± 2%

Recovery tests for the other carbides are planned, with and without sodium present.

(c) Primary and Secondary Argon. Table I.E.10 lists high, low, and average concentrations of hydrogen and nitrogen in the primary and secondary cover-gas systems.

TABLE I.E.10. Hydrogen and Nitrogen in Primary and Secondary Argon (ppm)

	Primary			Secondary		
	High	Low	Avg	High	Low	Avg
H_2	108	0	18	0	0	0
N_2	6,500	2,500	4,700	400	200	300

j. Experimental Irradiation and Testing (H. Lawroski)

Last Reported: ANL-7518, pp. 50-53 (Nov 1968).

(i) Experimental Irradiations (R. Neidner)

(a) Status of Experiments in EBR-II. The status of the experimental irradiation subassemblies in EBR-II as of the end of Run 32 is shown in Table I.E.11.

TABLE I.E.11. Status of EBR-II Experimental Irradiations

Subassembly (Position)	Date Charged	Capsule Content and Number of Capsules ( )		Experimenter	Accumulated Exposure (MWd) at End of Run 32	Estimated Goal Exposure (MWd)	Approx Accumulated Burnup (fuels--a/o) (nonfuels--nvt x 10^{-22})
XG03 (7D1)	7/16/65	UO_2-20 w/o PuO_2	(2)	GE	19,600	23,300	5.1
		Stainless Dummies	(17)				
XG04 (7B1)	7/16/65	UO_2-20 w/o PuO_2	(2)	GE	19,600	45,000	5.1
		Stainless Dummies	(17)				
XA08 (4F2)	12/13/65	UC-20 w/o PuC	(8)	ANL	15,770	20,700	9.8
		Structural	(9)	ANL			5.8
		Structural	(2)	GE			5.8
XO10 (7F3)	3/24/66	UO_2-20 w/o PuO_2	(4)	GE	16,531	20,400	6.1
		Structural	(11)	ANL			3.3
		Structural	(4)	PNL			3.3
XO12 (4B2)	8/10/66	UO_2-20 w/o PuO_2	(19)	NUMEC	12,370	21,400	7.5
XO15 (4A2)	11/15/66	UO_2-20 w/o PuO_2	(11)	NUMEC	10,715	11,500	6.4
		UO_2-20 w/o PuO_2	(2)	GE			5.9
		UC-20 w/o PuC	(4)	ANL			6.5
		U-Fs (Mark-1A)	(2)	ANL			2.4
XO18 (2B1)	12/6/66	Structural	(3)	GE	10,746	22,900	4.4
		Structural	(1)	PNL			4.4
		Structural	(2)	ANL			4.4
		Structural and Heavy-metal Fission-yield Sample	(1)	ANL			4.4
XO19 (6D2)	1/13/67	UO_2-20 w/o PuO_2	(7)	GE	9,150	13,000	3.3
		UC-20 w/o PuC	(3)	UNC			3.9
		Structural	(8)	PNL			2.5
		Graphite	(1)	PNL			2.5
XO20 (6B5)	1/13/67	UO_2-PuO_2	(9)	GE	9,563	13,000	3.4
		UC-20 w/o PuC	(3)	UNC			4.1
		Structural	(4)	PNL			2.6
		Structural	(2)	ANL			2.6
		Graphite	(1)	PNL			2.6
XO25 (4E2)	10/10/67	Structural	(19)	GE	8,458	7,700	3.1
XO27 (4B3)	11/21/67	UO_2-25 w/o PuO_2	(18)	GE	6,886	7,700	4.2
		Structural	(1)	PNL			2.5
XO32 (6E5)	11/22/67	UO_2-25 w/o PuO_2	(19)	PNL	6,189	11,900	2.6
XO33 (5E2)	12/22/67	UC-20 w/o PuC	(19)	UNC	6,033	10,900	3.2
XO34 (2F1)	4/13/68	Structural	(7)	ORNL	6,415	14,800	2.6

TABLE I.E.11 (Contd.)

Subassembly (Position)	Date Charged	Capsule Content and Number of Capsules ( )	Experimenter	Accumulated Exposure (MWd) at End of Run 32	Estimated Goal Exposure (MWd)	Approx Accumulated Burnup (fuels--a/o) (nonfuels--nvt x 10^{-22})
XO35 (7B4)	4/13/68	Structural (7)	ORNL	5,998	44,800	1.2
XO36 (7E1)	7/25/68	UO_2-25 w/o PuO_2 (19)	GE	4,284	33,300	1.1
XO38 (7C5)	5/7/68	Structural (7)	INC	5,489	17,700	1.1
XO39 (3C2)	8/15/68	UO_2-25 w/o PuO_2 (5)	PNWL	2,532	3,000	1.0
		UC-20 w/o PuC (1)	LASL			1.5
		Structural (4)	GE			1.0
		UO_2-20 w/o PuO_2 (1)	ANL			1.5 + 3.7[a] = 5.2
		UO_2-20 w/o PuO_2 (7)	GE			1.6 + 3.7[a] = 5.3
		Structural (1)	GE			1.0 + 4.7[a] = 5.7
XO40 (5B2)	8/14/68	UO_2-20 w/o PuO_2 (19)	ANL	3,574	7,000	1.7
		UO_2-25 w/o PuO_2 (16)	GE			1.8
XO41 (7A3)	7/24/68	Structural (7)	PNL	3,950	16,700	0.8
XO42 (7D5)	7/24/68	Boron Carbide (4)	PNL	4,363	27,800	0.9
		Tantalum (3)	PNL			
XO44 (7A1)	9/28/68	Oxide Insulator (1)	LASL	2,625	8,100	0.5
XO51 (3A2)	12/16/68	UO_2-25 w/o PuO_2 (37)	PNL	545	16,400	0.3
XO52 (4C3)	11/25/68	Mark-IA (3)	ANL	1,397	1,400	0.5 + 2.4[a] = 2.9
XO53 (4E3)	11/27/68	Mark-II (37)	ANL	1,397	1,400	0.8 + 2.5[a] = 3.3

[a]Previous exposure from another subassembly.

Special Subassembly XO52, containing three encapsulated Mark-IA fuel pins from XO17, was remotely assembled in the Air Cell and charged into core position 4C3. This subassembly is a modified Mark-A design in which 16 of the 19 channels are occupied by solid stainless steel rods to provide a satisfactory flow pattern for meeting test and temperature criteria. The subassembly is scheduled for irradiation in Run 32 only (consisting of Runs 32A, 32B, and 32C).

Subassembly XO53 (reconstituted XO29) was also remotely assembled in the Air Cell and loaded into the reactor in position 4E3. Of the 37 encapsulated Mark-II fuel pins in the subassembly, 34 were reassembled from XO29 and 3 are new, unirradiated capsules.

Subassembly XO51, of Mark-F-37 design, was loaded into grid position 3A2 after the end of Run 32A. This subassembly contains 37 mixed-oxide elements from series PNL-3. Each element is 0.250 in. in diameter and uses a 0.062-in.-dia spacer wire. This is the first loading of a Mark-F-37 subassembly in EBR-II.

(b) Status of Irradiation Experiments Given Approval in Principle. The status of all irradiation experiments that have been given approval in principle but have not been loaded into the reactor is summarized in Table I.E.12.

TABLE I.E.12. Status of Experiments with Approval in Principle

Sponsor	Material of Test	No. of Capsules	Suggested Reactor Row[a]	Date of AIP	Estimated Delivery
ANL	Oxide fuel, Group O-3	19	3	9/22/67	1/69
	Carbide fuel, Group C-5	19	2	9/22/67	Indefinite
	Mark-II fuel (unencap)	455	Core	9/22/67	2/69
	Mark-II fuel (encap)[b]	25	4	6/3/67	6/68[c]
	Metal fuel, M-4	19	3	2/13/68	Indefinite
	Structural, Group S-9	19	4	9/22/67	2/69
	Magnetic materials	7	7	6/8/67	1/69
	Instrumented subassembly	1	5	5/9/68	2/69
BMI	Nitride fuels	4	5	8/28/68	1/69
GE	Oxide fuels, Group 7	4	4	9/2/66	2/68[c]
	Oxide fuels, Group 5	19	4	1/20/67	1/69
	Oxide fuels (unencap), Group 9A	37	4	1/20/67	11/68[c]
	Oxide fuels (unencap), Group 9B	37	6	5/9/68	2/69
	Oxide fuels (unencap), Group 9C	37[d]	5	5/9/68	12/68
	Oxide fuels (unencap), Group 9D	37	7	5/9/68	1/69
INC	Structural	14	7	8/28/68	1/69
LASL	Carbide fuels	6	3	2/27/67	2/69
NRL	Structural materials	7	7	9/6/67	2/69
ORNL	Oxide insulators	7	8	9/21/67	2/69
	Sol-Gel oxide fuel	5[e]	4	5/9/68	12/68
PNL	Oxide fuel (unencap), PNL-4	37	4	9/21/67	1/69
	Oxide fuel (unencap), PNL-5	37	3	9/21/67	12/68
	Graphite materials	7	7	7/31/67	Indefinite
	Thermocouple materials	5	4	7/31/67	Indefinite
		2	4	7/31/67	2/68[c]
UNC	Carbide fuel (UNC 88)	1	4	12/9/65	10/66[c]
	Carbide fuel (UNC 129-147)	19	7	6/6/67	1/69
	Carbide fuel (UNC 185-190)	6	3	1/20/67	6/68[c]
	Carbide fuel (UNC 191-209)	19	3	8/28/68	4/69
W	Carbide fuel (+ V-alloy)	4[f]	4	8/28/68	1/69
	Carbide fuel (+ V-alloy)	12	g	8/28/68	Indefinite

[a]Based on fission rates at a reactor power of 50 MWt.
[b]Replacements for capsules of same type whose irradiation is nearing completion (e.g., Subassembly XO29).
[c]Date received.
[d]Six capsules delivered; expected delivery of others as indicated.
[e]Four capsules delivered; expected delivery of other as indicated.
[f]Two capsules delivered; expected delivery of others as indicated.
[g]Space-available basis.

(c) New Experimental Subassembly Design. Two new experimental subassembly designs have received final approval for reactor use: the Mark-C-19 and -C-37 (same basic design) and the Mark-H-37.

The Mark-C design features a concept of split internal flow. The central flow is heated by passing it over the fuel samples, and the annular flow bypasses the fuel samples and remixes with the heated central flow above the fuel but before leaving the subassembly.

The design of the Mark-H, similar to that of the Mark-F, provides an inner hex flow shroud to contain 37 fuel elements of 0.250-in. diameter with spacer wires of 0.040-in. diameter. The space between the flow shroud and outer hex can would contain only weepage sodium when in use.

Initial design efforts have been started on a new subassembly which would contain 61 elements of 0.230-in. diameter with 0.040-in.-dia spacer wires.

(ii) Handling and Examination

(a) Testing of Procedures for Removing Sodium from Subassemblies. The pressurized tubes selected for investigation from Subassembly X900 were depressurized after their fifth and final wash cycle. Metallographic investigation of these sodium-to-water-cycled specimens was initiated.

(iii) Procurement and Nondestructive Testing (G. K. Whitham and D. C. Cutforth)

(a) Tubing Procurement. Delivery of the 0.290-, 0.335-, and 0.375-in.-OD tubing ordered early in the fall has been delayed until April 1969. The stainless steel strip to be used for making the tubing has been rejected by the tubing manufacturer because of an odd grain-boundary condition. The strip will be remelted and rerolled, and is scheduled for redelivery to the tubing manufacturer late in February 1969. Current supplies of tubing will last until spring.

A purchase order is being issued for 2000 ft each of 0.805- and 0.220-in.-OD tubing.

(b) Improved Resolution from Neutron Radiography. A rejected driver-fuel pin from the cold line was encapsulated in Mark-B-37 hardware and neutron radiographed several times at TREAT with different exposure conditions. The parameters which were varied were type of detector foil, geometry, integrated dose, and beam filtration. The best results obtained to date have been with an unfiltered beam, a dysprosium foil, a film density of about 2.2, and good exposure geometry. The gap between the fuel and the cladding was clearly identified on the best radiograph.

An analysis of α-n sources was performed to determine the potential of these sources for neutron radiography. The results show that in the optimum moderator arrangement one would need 10^{10} n/sec to have a radiography source equivalent to the FCF source with 7000 Ci ^{124}Sb.

k. FCF Process Analysis and Testing (M. J. Feldman)

(i) Test and Analytical Methods (M. J. Feldman, J. P. Bacca, E. R. Ebersole, and V. G. Eschen)

Last Reported: ANL-7518, p. 54 (Nov 1968).

As part of the program to develop the capability for remote reencapsulation, the pressure-vacuum technique for loading sodium into capsules was tested. Satisfactory results were obtained.

l. FCF Equipment Improvements (M. J. Feldman)

(i) Auxiliary Equipment (W. L. Sales and K. H. Kinkade)

Last Reported: ANL-7518, p. 54 (Nov 1968).

(a) Pneumatic Transfer System. The receiving and sending station for the pneumatic transfer system was installed in the FCF transfer cell. This completed the hot-sample transfer system between the FCF cells and the analytical caves. Several empty carriers were sent back and forth, each taking approximately 14 sec each way.

(b) Transfer-cell Plug and Manipulators. The transfer-cell plug was installed and is operating satisfactorily. Models-D and -F master slaves were installed for use with the window and transfer system in the plug for transferring items directly out of the cell. These manipulators will also operate the pneumatic transfer system mentioned above.

When the equipment decontamination and repair facility is completed, it will also operate in conjunction with this transfer plug. Small items will be brought out through the transfer system within the plug. When transferring large items, the entire plug will be removed so that a cask can be moved into the transfer cell for loading and subsequent movement to the FCF decontamination areas.

(ii) Repair and Decontamination (W. L. Sales and K. H. Kinkade)

Last Reported: ANL-7513, p. 76 (Oct 1968).

The crane for the manipulator repair and decontamination facility was received and installed. Final acceptance tests of the contractor-furnished components are underway.

m. Nuclear Instrument Test Facility Study (R. E. Rice)

Last Reported: ANL-7513, p. 77 (Oct 1968).

(i) Out-of-core Thimble Modification to Provide a Facility for Tests from 650/700°F to 1200°F (J. D. Cerchione)

The Preliminary Feasibility Study and Conceptual Design Description for this facility is being revised. It will include a section describing the facility for sodium prooftesting that was originally proposed for prooftesting of components. An accelerated schedule for this high-temperature nuclear instrument test facility (NITF) may eliminate any possibility of out-of-pile prooftesting of components.

Construction of a sodium-prooftest loop may still be necessary to fulfill component-testing requirements of the packaged loop and future projects. Tentative specifications for the loop provide for a sodium flowrate of 25 to 30 gpm at 16 to 20 psi and a system temperature of 700°F. The flow and head specifications are limited by an available EM pump, and the 700°F temperature was selected to simulate the EBR-II primary-tank temperature. The size of the loop-test tank tentatively has been established as 18 in. in diameter and 20 ft high. This size would permit testing of full-sized nuclear instrument test thimbles and packaged loops.

Preliminary design of the heater controls and temperature instrumentation for the NITF is in progress. Different methods are being investigated for controlling the heaters to be installed in the thimbles. DC power is expected to be supplied by a transformer-rectifier power supply, with contactors controlled by temperature sensors in the thimble. A variable-voltage transformer can be employed to adjust power input to the heaters to compensate for heat losses. This method should improve control and reduce the frequency of contactor operation. Each heater section will have individual variable-voltage control. A higher voltage, supplied by a transformer tap and controlled by a manually operated switch, may also be provided to increase power input to the heaters during heatup to operating temperature.

A new design concept of the NITF is being developed. This concept will include a 5-ft-long oven for heating the detector cable to 1200°F, but will not include a vertical detector traversing mechanism. A list of pertinent questions was sent to proposed experimenters who will make use of the facility. Of primary concern are the outer dimensions of the nuclear detectors and cables. Also of concern is the flexibility of the high-temperature cables that must be passed through spiral-shaped tubes in the shield plugs for the thimble.

n. Feasibility Study of Fuel Failure Detection--Chemical and Mechanical Methods

(i) Trace Elements Analytical Techniques (C. E. Crouthamel)

Last Reported: ANL-7518, p. 56 (Nov 1968).

The goals of the program for fuel-failure detection are to select suitable tags for individual subassemblies and to develop methods for identifying the tagged elements in liquid sodium. Antimony is one of the elements being considered for use as a tag. The composition of naturally occurring antimony is 57.25% ^{121}Sb and 42.75% ^{123}Sb. Antimony that is highly enriched in each isotope is available, and various mixtures of these enriched isotopes would provide a large number of unique tags. The identification of a tag released from a failed element would be made by determining the isotopic ratio of the tag mixture. This method of tag identification has been discussed previously in connection with the proposed use of xenon isotopic tags (see Progress Report for April 1968, ANL-7445, p. 85). Two analytical methods are being considered for identifying antimony tags: neutron activation and spark-source mass spectrometry.

A test was made of the feasibility of determining isotopic ratios of antimony by neutron activation and subsequent computer analysis of the gamma-spectrometric data. A sample of natural antimony was irradiated in CP-5 for 2 min in a flux of 2×10^{13} n/cm^2. The activation products, ^{122}Sb ($t_{1/2}$ = 2.8 days) and ^{124}Sb ($t_{1/2}$ = 60.4 days), were assayed 2.5 and 29 hr after irradiation by gamma spectrometry, and the number of atoms of ^{122}Sb and ^{124}Sb present at the end of the irradiation was calculated. From these data and the appropriate thermal-capture cross sections, the $^{121}Sb/^{123}Sb$ ratio in the starting material was calculated. Values of 1.37 and 1.33, respectively, were obtained for the assays at 2.5 and 29 hr; these are in excellent agreement with the known isotopic ratio of natural antimony, namely, 1.34.

Samples of natural antimony will also be examined by spark-source mass spectrometry to determine the accuracy with which the $^{121}Sb/^{123}Sb$ ratio can be measured.

o. Materials-Coolant Compatibility (D. W. Cissel)

(i) Problems Identified due to Operations (W. E. Ruther and T. D. Claar)

Last Reported: ANL-7518, pp. 56-57 (Nov 1968).

Chemical analysis, electron-microprobe evaluation, and fatigue testing have indicated that carburization did not cause the failure

of the Type 347 stainless steel bellows of the SN-17 valve from the EBR-II secondary-sodium sampling system.

Carbon content of a section of the bellows near the defected area analyzed 0.08 w/o, the same as the maximum carbon specification given for Type 347 stainless steel. The electron microprobe showed a carbon peak for only one of the more than ten attack sites evaluated on the sodium side of the bellows. However, a number of the observed areas showed an oxygen peak coupled with a chromium increase. This evidence, combined with the results of the chemical analysis, tends to discourage the carburization hypothesis. The simultaneous peaking of oxygen and chromium in the attack areas suggests an oxidation phenomenon; this possibility will be investigated.

In the fatigue tests, two sections of Type 347 stainless steel bellows, one carburized and the other uncarburized, were extended and compressed at 42 cycles/min. Both of the $1\frac{3}{16}$-in.-long by 1/4-in.-wide sections previously had been exposed to sodium at 550°C for one week, but one of the sections had been carburized by putting a drill rod (0.9-1.1 w/o C) in the sodium. Carburization of the one section was verified by oxalic electrolytic etch. The carburized bellows failed after 55.8 hr, and the uncarburized bellows failed after 82.3 hr. These tests indicate that carburization in sodium reduces fatigue life, but not to the extent noted for the SN-17 valve bellows.

(ii) Data Development (F. A. Cafasso)

Last Reported: ANL-7500, p. 76 (Sept 1968).

Type 304 stainless steel in the form of coils of large surface area is being heated in liquid sodium at 650°C over long periods to determine the diffusion rates and distribution behaviors of various constituents of stainless steel. The materials are contained in tantalum capsules. Two of these capsules have been opened after one month, and the sodium phases are being analyzed for copper, nickel, chromium, iron, and manganese.

p. Systems Engineering (B. C. Cerutti)

(i) Surveillance, Evaluation, and Studies of Systems

Last Reported: ANL-7518, pp. 59-62 (Nov 1968).

(a) Primary Coolant Flow Monitors (R. O. Haroldsen)

The draft of the engineering submittal for simplifying the coolant flow monitors is being reviewed. The review group requested

more analyses of selected types of flow failures. Sufficient data on flow coast-down experiments are available for this purpose. Considerable analytical data are also available which predict maximum temperatures in subassemblies after total instantaneous flow failure. The latter data, however, are based on reactor shutdown simultaneous with pump failure. A new analysis will be made based on reactor shutdown which is delayed until a drop of 8% in the coolant flow occurs; this 8% drop is the normal trip-point setting of the flow monitors.

(b) Packing Gland for Main Core Gripper (J. B. Waldo)

Three types of Teflon-impregnated packing were received as possible replacements for the graphite packing now used in the gripper gland. One of the three was tested in a sodium-vapor atmosphere at approximately 500°F. After approximately 16 hr, the packing was already visibly deteriorating, so the test was suspended. Use of Teflon-impregnated packing in the top rings of the packing gland, which are essentially out of a sodium environment, might still be considered.

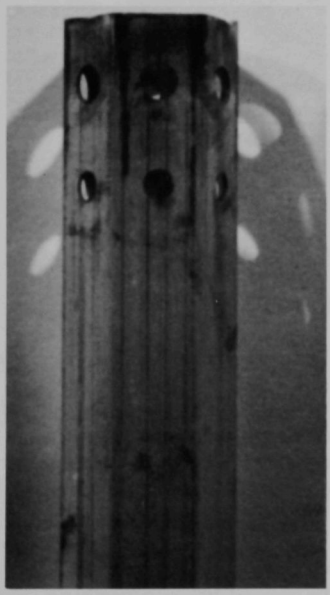

Fig. I.E.2

Safety-rod Thimble Removed from Core Position 3D1 on November 20, 1968. The two damaged top edges are visible at the top of the photograph.

(c) Inspection of Damaged Safety-rod Thimble (B. C. Cerutti, C. C. Crothers, and H. W. Sine)

Visual inspection of the safety-rod thimble removed from the reactor on November 20 and transferred to the FCF showed damage to two of the flats at the top of the hex can (see Figs. I.E.2 and I.E.3). This damage is similar to but less severe than that suffered by the control-rod thimble removed in January 1968 (see Progress Report for January 1968, ANL-7419, pp. 48-49). The damage observed in that thimble was postulated to have occurred in a series of steps during a number of insertions of adjacent subassemblies. The two flats of the safety-rod thimble removed on November 20 appear to have been damaged in a similar fashion.

The safety-rod thimble was removed because minor fuel-handling problems had been encountered when handling adjacent subassemblies. No problems were encountered while removing the safety rod from the thimble, indicating that there was no binding between the rod and the thimble.

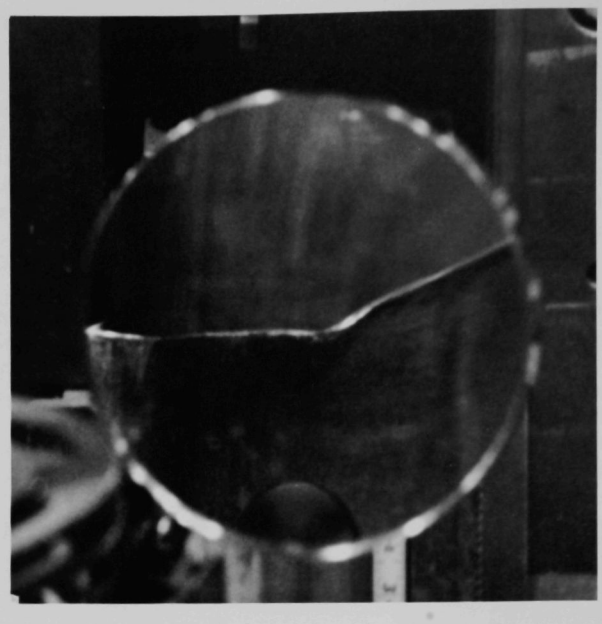

Fig. I.E.3. Magnified View of One of the Two Damaged Top Edges of the Safety-rod Thimble Removed from the Reactor on November 20. The other edge was damaged less.

(ii) Reactor and Primary Systems Improvements

Last Reported: ANL-7518, pp. 62-64 (Nov 1968).

(a) New Plugging Meter for Primary Purification System (C. C. Crothers)

A new plugging meter for the primary purification system has been installed and is in routine operation. Testing of the new meter is being continued on a limited basis to determine optimum operating conditions.

The plugging valve for the new plugging-meter system is a 1/2-in. bellows-seal valve with high-temperature backup packing. The valve was modified by milling ten 40- by 40-mil grooves in the stem insert and is remotely operated by flexible shafts, as are the other valves in the system.

The inlet and outlet valves serve as isolation valves, with the inlet valve also serving as a throttle valve. In addition to these

valves, a bypass valve has been included to provide an approach to constant head at the plugging valve. Although provision of bypass flow was expected to provide a more pronounced break in the recorded flow during a plugging-temperature determination, only a slight improvement of this break was obtained.

A desirable feature of the new plugging meter is sequenced electrical heating. The system is heated in a stepwise sequence to eliminate stresses due to sodium expansion which could cause failure of components.

The meter system includes a sodium-to-sodium heat exchanger and a sodium-to-air heat exchanger. The latter exchanger is equipped with a 0- to 120-cfm variable-speed blower to provide positive control of the cooling rate during a plugging-temperature determination.

The flowmeter for the new system is immediately ahead of the sodium-to-sodium heat exchanger in the constant-temperature leg of the system. This change has produced a decided improvement in flow indication because the flowmeter is now unaffected by the temperature transient occurring during the plugging run.

q. Leak Detection and Location--Xenon Method (R. E. Rice and P. B. Henault)

Last Reported: ANL-7518, pp. 64-65 (Nov 1968).

Continued evaluation of the requirements for the unit to collect xenon tags indicates that a relatively simple modification of existing hardware will be adequate. A preliminary design description has been submitted for internal review.

General Electric reported that the test conducted to determine the adequacy of their apparatus for injecting xenon tags was completely successful and that they plan to start tagging early in January. They have recommended to the AEC the use of xenon tags, as proposed by ANL, in Subassembly F9D.

2. Operations

a. Reactor Plant (G. E. Deegan)

Last Reported: ANL-7518, pp. 66-67 (Nov 1968).

(i) Operations (J. R. Davis)

Fuel loading for Run 32A was completed concurrently with the checkout, filling, and initial operation of the primary purification system.

Cooling-water systems were returned to normal following tie-in of the new auxiliary cooling tower.

The reactor was started up on November 27 and a reduced-flow experiment was conducted at the beginning of the run. After the activity levels in the primary-tank cover gas had stabilized for 50-MW operation, control rod No. 2 (Subassembly L-462) was lowered to its down position as part of the search for the source of the fission-product release. Within 48 hr the ^{135}Xe activity in the cover gas had decreased by about one-third. The control rod was reinserted, and the ^{135}Xe activity returned to the higher value previously observed. From this, the conclusion was made that control rod No. 2 was the probable source of the fission-product release. Run 32A was completed with the control rod in the fully down position.

Run 32A ended with rod-drop kinetics experiments at 500 kW and 50 MW, a reduced-flow experiment, and a measurement of the ascending power-reactivity decrement.

Fuel handling for Run 32B included the removal of control rod No. 2 and the installation of one experimental subassembly. Fifty-megawatt operation was resumed after startup on December 18.

The reactor operated for 1188 MWd during December and had accumulated 22,666 MWd by the end of the month.

b. Fuel Cycle Facility (M. J. Feldman)

Last Reported: ANL-7518, pp. 67-75 (Nov 1968).

(i) Fuel Production

(a) Hot Line (N. R. Grant)

Table I.E.13 summarizes the production activities for December and for the year.

The air-cell crane stopped several times during the month in the same place--at the south end of the crane bridge, above the straightness tester and the assembly machine. The stoppage occurred while transferring subassemblies in and out of the tester and the assembly machine. Investigation revealed a dead spot in the electrical bus bar at the bridge at this point. The straightness tester was moved approximately 2 ft north, away from the dead spot. Care will be used to avoid the dead spot when handling subassemblies at the assembly machine.

TABLE I.E.13. Production Summary for FCF Hot Line

	December 1968	Total This Year
Subassemblies received		
Core, control, and safety	19	141
Other	3	72
Subassemblies sent to ICPP for storage	3	8
Subassemblies dismantled for processing	17	119
Subassemblies dismantled for examination, etc.	0	29
Subassemblies fabricated	5	35
Subassemblies transferred to reactor	7	70
Subassemblies sent to L&O vault and interbuilding corridor for storage	0	0
Elements Decanned		
From irradiated subassemblies	796	7911
Rejects	56	483
Other	0	188
Total decanned	852	8582

Melt Refining

	Irradiated Fuel	Recycle Material	New Fuel
Number of runs	6	4	0
Average pour yield, %	92.5	93.1	-
Total runs in 1968	57	32	4

Processing

	December 1968	Total This Year
Injection-casting runs	9	95
Elements processed		
Accepted	714	3954
Rejected	120	883
Elements welded	506	3585
Elements rewelded	0	4
Elements leaktested		
Accepted	418	3571
Rejected	31	202
Elements bonded (including recycle)	423	4408
Elements bond tested		
Accepted	157	2782
Rejected	21	268
Elements to surveillance	490	3124
Number of subassemblies	14	80

Waste Shipments

Cans to burial ground	7	70
Oxide and glass scrap to ICPP	13	41

Repair of the inoperable electromechanical manipulator in the Air Cell has been postponed because construction of the manipulator repair facility is not complete.

Modifications of the transfer cell between the Air and Argon Cells (subcell 4) were completed. These included: (1) placing into operation the pneumatic transfer system for conveying samples to the analytical laboratory; (2) installing and testing the movable shield plug for the entrance to the subcell; (3) installing two master-slave manipulators; and (4) installing additional lighting equipment in the subcell.

(b) Cold-line Production and Assembly (D. L. Mitchell)

Efforts required for acceptance inspection of vendor-produced fuel reduced the bonding and bond-testing throughput for cold-line-produced fuel. Production data for the month and for the year are summarized in Table I.E.14.

TABLE I.E.14. Production Summary for FCF Cold Line

	December 1968	Total This Year
Alloy-preparation runs		
New fuel	0	6
Remelts	6	58
Total	6	64
Injection-casting runs	8	112
Pins processed		
Accepted	808	9000
Rejected	27	786
Elements welded	385	6815
Elements rewelded	0	15
Elements leaktested		
Accepted	596	7122
Rejected	2	75
Elements bond tested		
Accepted	308	6559
Rejected	103	507
Elements available for subassembly fabrication (cold-line fuel)	0	0
Subassemblies fabricated (cold-line fuel)	8	80
Elements received from vendor	1166	4097
Inspected and accepted	3316	3398
Inspected and rejected	689	699
Elements available for subassembly fabrication (vendor fuel)	2956	3038
Subassemblies fabricated (vendor fuel)	3	4

(ii) Inspection of Vendor Fuel (D. L. Mitchell)

Modifications of the cold-line building were started to provide additional space for inspection of vendor-produced fuel. When this space is available, inspection of vendor-produced fuel will no longer interfere with cold-line production.

The acceptance for vendor-produced elements has increased from an original rate of less than 75% to a present rate of about 90%. This improvement was obtained after the vendor instituted a post-bonding step to reduce the size and number of shrinkage voids.

The initial vibratory test of vendor-produced elements (see ANL-7518, pp. 69-70) was terminated after 154 hr when a faulty heater switch allowed the temperature of the elements to exceed the desired test temperature of 500°C. Thirty-nine of the 42 elements being tested had developed voids of rejectable size prior to the heater failure. A second vibratory test was initiated using 30 acceptable (as-received) vendor-produced elements, 10 vendor-produced elements that were rejectable because of sodium voids when received, and 5 acceptable cold-line-produced elements.

(iii) Surveillance or Failure Analysis of Product (M. J. Feldman, J. P. Bacca, and E. R. Ebersole)

(a) Chemical Analyses (E. R. Ebersole)

The number of fuel-product analyses of hot-line, cold-line, and vendor fuel samples made in December, together with the average values and ranges, are as follows:

Analyzed for	Number	Average Value	Range
Total U	24	94.47 w/o	93.91-94.87
^{235}U (% of total U)	24	52.10 w/o	51.92-52.38
^{239}Pu	12	1330 μg/g	710-1810
Mo	20	2.48 w/o	2.05-2.61
Ru	22	1.91 w/o	1.81-2.03
Rh	18	0.265 w/o	0.233-0.289
Pd	22	0.183 w/o	0.160-0.198
Zr	23	0.074 w/o	0.030-0.099
Nb	12	0.009 w/o	0.008-0.011
Si	90	380 ppm	171-670
Al	20	94 ppm	60-195
Cr	20	70 ppm	30-127
Fe	28	441 ppm	71-1070
Ni	15	154 ppm	99-192
C	7	188 ppm	160-380
Total Analyses	357		

December analyses for surveillance of irradiated pins from the reactor are tabulated below:

Analyzed for	Number	Average Value	Range
Al	12	128 ppm	52-260
Fe	6	406 ppm	292-554
Zr	6	0.113 w/o	0.082-0.134
Nb	4	0.010 w/o	0.008-0.011
Ru	1	1.87 w/o	
Si	33	365 ppm	86-957
Total Analyses	62		

(b) Postirradiation Analysis of EBR-II Fuel (J. P. Bacca)

(1) Surveillance of Mark-IB Fuel. The fifth and final Mark-IB subassembly (C-2136) of this surveillance program, now being irradiated in EBR-II, will attain a target burnup of 1.2 a/o at the end of Run 32B.

(2) Surveillance of Cold-line Fuel. Elements from cold-line Subassembly C-2130 were examined after irradiation in EBR-II to a calculated maximum subassembly burnup of 1.18 a/o, approximately 0.4 a/o of which was accumulated during 50-MWt operation. Seven batches of cold-line fuel, with silicon contents ranging from 140 to 376 ppm, were represented in this subassembly. The fuel swelled an average of 5.9%; maximum swelling was 13.0% and the minimum was 3.9%. These swelling values are in reasonable agreement with those observed following comparable burnup of similar types of fuel (with comparable silicon contents) manufactured in the FCF hot line.

As has been observed in the past, the silicon content of the fuel affects its swelling characteristics. The higher-swelling elements of Subassembly C-2130 were those manufactured from the two batches with the lowest silicon content (140-145 ppm). The elements made from the other five batches (with silicon contents ranging from 220 to 376 ppm) displayed significantly lower fuel-swelling characteristics.

The fifth and last subassembly (C-2120) of the first phase of the cold-line surveillance program accumulated its target burnup of 1.25 a/o at the end of Run 32A. Postirradiation surveillance examinations of elements from this subassembly will be conducted in the near future.

(3) Surveillance of Vendor-produced Fuel. Three subassemblies containing fuel elements manufactured by Aerojet-General Corp. are being irradiated in EBR-II. Tentative target burnup levels for the

subassemblies (C-2178, C-2181, and C-2182) are 0.6, 0.8, and 1.0 a/o, respectively. The initial burnup level of 0.6 a/o should be attained by Subassembly C-2178 approximately halfway through Run 33.

(4) 50-MWt Surveillance Program. One of the requirements associated with raising the power level of the EBR-II from 45 to 50 MWt is the surveillance of selected subassemblies that have been irradiated at the higher power level. The purpose of these examinations is to provide assurance that the slightly higher irradiation temperatures associated with the higher power level has not caused significantly greater volume swelling of the driver fuel.

Two subassemblies of this surveillance program were examined during December. The first (C-2049) had been irradiated to a calculated maximum burnup of 0.95 a/o, of which 0.17 a/o had been accumulated during 50-MWt operation. The second subassembly (C-2072) had been irradiated to a maximum burnup of 1.06 a/o, of which 0.44 a/o had been accumulated during 50-MWt operation.

Tables I.E.15 and I.E.16 summarize the compositions, burnups, and fuel-swelling data for elements from the two subassemblies. The figures for average fuel swelling of C-2049 (see Table I.E.15) are comparable to those observed in the past for several thousand driver-fuel elements irradiated during 45-MWt operation. Furthermore, the swelling data for C-2072 (see Table I.E.16) are comparable to those observed in the past for similar types of U-5 w/o Fs fuel irradiated during only 45-MWt operation. Table I.E.16 also shows

TABLE I.E.15. Swelling of Fuel in 50-MWt Driver-fuel Surveillance Subassembly C-2049

Injection-casting Batch No.	Silicon Content of Fuel (ppm)	Number of Elements	Element Burnup Range[a] (a/o)	Total Volume Swelling of Fuel (ΔV/V, %)	
				Average	Range
0403	110	1	0.90	6.2	-
0406	60	40	0.90-0.94	6.1	3.4-8.1
0408	170	48	0.85-0.90	5.1	3.4-7.1

[a]Max burnup 0.95 a/o, of which 0.17 a/o was accumulated during 50-MWt operation.

TABLE I.E.16. Swelling of Fuel in 50-MWt Driver-fuel Surveillance Subassembly C-2072

Injection-casting Batch No.	Silicon Content of Fuel (ppm)	Number of Elements	Element Burnup Range[a] (a/o)	Total Volume Swelling of Fuel (ΔV/V, %)	
				Average	Range
0409	130	5	1.01-1.02	12.3	9.2-14.0
0410	120	7	1.04-1.06	11.4	10.7-12.5
0411	160	58	0.98-1.04	10.3	6.5-15.2
4208	240	1	1.02	5.6	-
4209	260	3	1.01-1.02	5.2	4.9-5.5
4211	290	14	1.03-1.05	5.2	3.1-6.0
4212	260	1	1.02	4.8	-

[a]Max burnup 1.06 a/o, of which 0.44 a/o was accumulated during 50-MWt operation.

that a silicon content greater than 200 ppm in the fuel enhances the resistance of the alloy to irradiation swelling.

A third subassembly in this program (C-2103) will be examined following irradiation to a burnup of 1.2 a/o at the end of Run 32B. Of the 1.2 a/o burnup, 0.6 a/o should have been accumulated during 50-MWt operation.

(5) Controlled-flow Experiment. This experiment, like the 70%-enriched-fuel experiment (see ANL-7518, p. 72), is being made to assess the irradiation performance of U-5 w/o Fs driver fuel under conditions typical of higher-power operation of EBR-II. In this experiment, however, the driver fuel in the surveillance subassemblies has a ^{235}U enrichment of 52%. The higher irradiation temperatures for the fuel, characteristic of higher-power operation of the reactor, are achieved by sizing the orificing of the subassemblies to reduce the coolant flow through them.

Subassembly C-2185, the first of three subassemblies of this experiment now being irradiated, is expected to reach its initial target maximum burnup during the first half of Run 33.

(6) Driver-fuel Extended-burnup Experiment. Subassembly C-2027 attained a calculated maximum burnup of 1.5 a/o at the completion of Run 32A. This is the highest burnup yet attained by a normal driver-fuel subassembly with unencapsulated elements. Postirradiation surveillance examinations of elements from this subassembly will begin after the postirradiation cooling period.

Subassembly C-2027 is the "lead" unit of a program to investigate the advisability of raising the maximum-burnup limit permitted for driver subassemblies above its present value of 1.20 ± 0.05 a/o. Previously, the maximum burnup reached by any driver subassembly was 1.31 a/o, attained by Subassembly C-291 of this program.

(7) Driver-fuel Silicon Surveillance Program. The purpose of the silicon surveillance program is to obtain data on the irradiation performance of U-5 w/o Fs alloy containing silicon in various amounts up to a maximum of approximately 1000 ppm. This program will provide the information necessary to establish wider limits for silicon specifications of EBR-II driver fuel manufactured in the future. Because a considerable number of subassemblies in the FCF inventory contain fuel having silicon contents higher than the specification limit (520 ppm) but below 1000 ppm, this program should also provide the experimental data necessary to justify use of these higher-silicon fueled subassemblies in EBR-II.

During December, Subassembly C-2155, containing fuel with silicon contents ranging from approximately 200 to 785 ppm, was examined following irradiation to a calculated maximum burnup of 0.78 a/o. Average swelling of fuel in the elements of the subassembly was 3.1%; maximum swelling was 4.2% and minimum 2.5%. These values are consistent with data observed in the past for fuel having silicon contents lower than the present specified maximum of 520 ppm. No abnormal swelling could be attributed to the higher-silicon fuel batches (to 785 ppm Si) in C-2155.

Subassembly C-2110, containing fuel to which silicon had been added to bring silicon contents within a range from 166 to 487 ppm, was examined following irradiation to 0.92 a/o calculated maximum burnup. Average swelling of fuel in the elements of the subassembly was 4.6%; maximum was 6.9% and minimum 3.0%. Again, these results are consistent with swelling data observed in the past for U-5 w/o Fs fuel of similar silicon content and comparable burnup.

(c) Materials Surveillance and Compatibility Studies (J. P. Bacca, R. V. Strain, C. L. Meyers, and S. T. Zegler)

The safety-rod thimble recently removed from EBR-II core position 3D1 is being examined for evidence of increases in the flat-to-flat dimensions at the midlength of the thimble and for bowing. Dimensional profiles are being constructed along the thimble axis by making: (1) precision caliper measurements across each of the three pairs of opposing flat; and (2) precision measurements of distance from each of the six flats to a fixed reference point. Preliminary results indicate that the flat-to-flat dimensions have increased and that bowing has occurred.

(iv) Fuel Management and Handling (N. R. Grant and P. Fineman)

A summary of fuel-handling operations is included in Tables I.E.13 and I.E.14.

(v) Experiment Handling and Interim Examination (V. G. Eschen and N. R. Grant)

Two experimental subassemblies were reloaded in the Air Cell. The first (XO52) is a Mark-A type containing three capsules that had been previously irradiated in Subassembly XO17. Each of the capsules contain metal fuel elements from ANL-MET. The other 16 positions in the subassembly have solid rods in place of the shroud tubes; therefore, essentially all the coolant flow will be cooling the three capsules. The second subassembly (XO53), a Mark-B-37 type,

contains 34 encapsulated Mark-II fuel elements that had been previously irradiated in Subassembly XO29 and three new capsules of the same material to replace three removed for extensive examination.

(vi) Reactor Support (N. R. Grant)

Control rod L-469S, containing two bare fuel pins, was received from the reactor and washed by a special procedure developed for bare-pin subassemblies. After disassembly, the two bare pins were stored for later examination. Three standard fuel elements were punctured, and the cover gas in the elements was tested for fission products. The data obtained from these samples are being evaluated.

PUBLICATIONS

A Jaw Crusher for Plutonium Ceramics
J. E. Ayer and H. Osuna*
Nucl. Appl. 5, 417-423 (Dec 1968)

The Use of Fast-Framing Cameras Instead of Magnetic Recording Media to Accumulate Data at High Rates
A. DeVolpi
J. Soc. Motion Picture and Television Engineers 77, 1286-1289 (Dec 1968)

In-core Activation Traverses during the Plutonium Recycle Experiment in the Experimental Boiling Water Reactor at Power Levels of 35 to 70 MW
R. E. Grajek and K. E. Freese
ANL-7414 (July 1968)

The EBR-II Feedback Function
R. W. Hyndman and R. B. Nicholson
ANL-7476 (July 1968)

Radiation Protection Requirements for Fabricating Recycled Plutonium Reactor Fuel
T. A. Steele, A. B. Shuck, and P. K. Doherty**
Radiation Protection, Proc. 1st Intern. Congr., Rome, September 5-10, 1966. Pergamon Press, Oxford, 1968, pp. 949-960

*Comision Nacional de Energia Atomica, Argentina.
**Purdue University.

II. OTHER FAST REACTORS--CIVILIAN--OTHER FAST BREEDER REACTORS

A. Fuel Development

1. Corrosion of Fuel Jacket Alloys

a. Sodium Corrosion of Austenitic Stainless Steels (J. Y. N. Wang and K. Figlik)

Not reported previously.

The interaction between liquid sodium and austenitic stainless steels, particularly Types 304 and 316, is complicated by many variables within the material structure as well as within the liquid. The selective and localized attack may be influenced by orientation effects, coherent precipitates, stacking faults, and other dislocation barriers. Low macrostresses may induce locally high microstresses, which could initiate and propagate cracking. The contaminants in the sodium exert a strong influence on the corrosion behavior of austenitic stainless steels. There is appreciable evidence* to support the importance of the close relationship between carburization and intergranular penetration of these materials in sodium. The initial phase of this work is, therefore, directed to the study of the structures of the precipitated carbides in relation to the penetration and temperature of a controlled sodium environment. Attention is also given to the mode of sodium penetration and to any complex compound that may form at the interface between the stainless steel and the sodium.

A high-temperature furnace with a rotating sample holder has been constructed for the corrosion tests, and thin sheets of Types 304 and 316 stainless steel of 5- to 10-mil thickness have been prepared. The average grain size of these samples was maintained at about 0.09 mm. Preliminary experiments are being conducted to evaluate techniques for preparing carbides (by precipitation and by carbon transfer to the stainless steel) for examination by means of the electron microscope. Current results of this work are being evaluated. The possibility of using a radioactive isotope tracing technique to elucidate the path of preferential attack at the grain boundaries is also being investigated.

b. Influence of Dissolved Cesium, Antimony, Rubidium, and Gold in Sodium on the Corrosion Behavior of Austenitic Stainless Steel (J. Y. N. Wang, C. A. Youngdahl, and K. Figlik)

Not reported previously.

An investigation has started to assist in the determination of the relative effect of sodium containing small additions of cesium, antimony,

*Rowland, M. C., and Plumlee, D. E., GEAP-4838 (Oct 1965); Andrews, R. C., et al., A Limited Comparison of the Relative Merits of 304 vs 316 SS for Liquid Metal Service, Topical Report No. 10, MSAR-67-216 (Dec 1967); Anderson, W. J., and Sneesby, G. V., NAA-SR-5282 (Sept 1960).

rubidium, or gold on the corrosion of Type 304L stainless steel. Radioactive isotopes of these elements have been suggested for possible use in the bond sodium of fuel elements in a sodium-cooled reactor to indicate failure of the stainless steel cladding. Pertinent phase diagrams indicated that these elements are soluble in sodium in the temperature region of interest (375 to 500°C).

Capsules of Type 304L stainless steel were loaded with 5- and 10-mil-thick samples of solution heat-treated Type 304L stainless steel and reactor-grade sodium containing 2 w/o additions of either high-purity cesium, antimony, rubidium, or gold. The capsules were loaded and electron-beam sealed in a drybox (with about 3 ppm moisture) and then sealed in quartz tubes under a reduced pressure of about 2×10^{-5} Torr. The assemblies were then rotated at a speed of 1 rpm (to promote mixing) other isothermal conditions at 650 ± 2°C for 500 hr. The exposure temperature of 650°C was chosen to verify the existence of an operating temperature margin.

After testing, the sodium was analyzed for oxygen by vacuum distillation and atomic absorption spectrometry. The results indicated less than 10 ppm oxygen. Insert samples were removed from the sodium at an elevated temperature to avoid solute precipitation, and the surfaces were cleaned with ethyl alcohol in a Soxhlet extractor under a cover gas of dry helium to prevent air contamination during the cleaning process.

The specimen weight changes in Table II.A.1 show that small weight gains were exhibited by all the tested samples. Inconsistencies between the weight gains of the two samples in a given capsule are shown for both the Na-2 w/o Cs and control capsules (no additive); however, damage was found on the surfaces of these specimens, which may have occurred during handling after exposure.

TABLE II.A.1. Weight Changes of Specimens after Exposure to Various Sodium Solutions at 650°C for 500 hr

Capsule No.	Additive in Sodium	Specimen Weight Gain ($\mu g/cm^2$)	
		5-mil Specimen	10-mil Specimen
Tg 15	2 w/o Au	11.0	15.0
Tg 16	2 w/o Cs	12.0	1.0
Tg 18	No additive	4.0	27.0
Tg 19	2 w/o Sb	31.0	30.0
Tg 20	2 w/o Rb	3.0	1.0

Metallographic examination showed a small amount of new phase formation near the surfaces of each sample. The new phases in the form of particles of different shapes were more evident in samples exposed to sodium containing cesium, antimony, and rubidium. Preliminary examination by electron-probe analysis indicates that these particles are not associated directly with the solution additives. No localized or general dissolution of the samples was observed under the test conditions.

2. Other Fuel Jacket Alloy Studies

a. Effect of Irradiation Temperature on the Ductility of Type 304 Stainless Steel (R. Carlander)

Last Reported: ANL-7478, pp. 56-57 (July 1968).

Previous experiments indicated that the ductility of Type 304 stainless steel was reduced by a greater amount when the alloy was irradiated at 371°C than when the alloy was irradiated near 460°C (see ANL-7478, p. 57). These results were for tensile tests conducted at 450°C at a strain rate of 1%/min with specimens of Type 304 stainless steel irradiated in EBR-II to a fluence of approximately 2×10^{22} n/cm^2. This adverse effect of low irradiation temperature on the ductility of Type 304 stainless steel has been investigated further by tensile tests with specimens irradiated in EBR-II at 600 ± 50°C to a nominal fluence of 2×10^{22} n/cm^2. The tensile tests were conducted at both room temperature and 650°C at a strain rate of 1.7%/min.

The ductility of the Type 304 stainless steel, as represented by the total elongation, did not appear to be affected by irradiation. The room-temperature total elongation of the irradiated alloy was 61%, compared with 65% for the unirradiated material. In addition, the total elongations of specimens tested at 650°C were between 18 and 24%, compared with 23% for the unirradiated alloy. The absence of a significant loss in ductility after irradiation at 600 ± 50°C was confirmed, in part, by transmission-electron-microscopic examination of the specimen tested at room temperature. No voids or dislocation loops were found in this specimen (see Section III.B.3.a).

These experiments and the results of the previous investigation are consistent in showing that fast-neutron damage is temperature-dependent; the embrittlement of Type 304 stainless steel decreased with increased irradiation temperature (371, 460, and ~600°C). Thus, Type 304 stainless steel cladding of a fast reactor fuel element might not become embrittled at operating temperatures near 600°C for exposures up to 2×10^{22} n/cm^2.

III. GENERAL REACTOR TECHNOLOGY

A. Applied and Reactor Physics Development

1. Theoretical Reactor Physics--Research and Development

a. Reactor Computations and Code Development (B. J. Toppel)

Last Reported: ANL-7487, pp. 77-79 (Aug 1968).

(i) The ARC System. The modules, standard paths, and system routines of the ARC system*,** have progressed to the point that very substantial production capability now exists in the system.

The system aspects of the ARC system are essentially complete in our present version. The effort is now concerned with producing more of the computational modules needed for our production use.

Table III.A.1 is an updated listing of the modules as planned for the ARC system. The changes as compared with Table VI of ANL-7332* reflect the influence of experience on our earlier planning. One may note for example that a number of the Input and Output Edit Modules are now missing, the function of these modules having been absorbed in the corresponding computational modules. Another notable change is the absence of the Criticality Search Module NUC008. The absorption of the search algorithm within the various neutronics modules was dictated by execution-time efficiency and is typical of the sort of dynamic change we may expect to see in our algorithmic repertoire as operational experience with the ARC system accrues.

TABLE III.A.1. ARC System Modules

I. Cross-section Preparation Modules

A. Input Modules

1. Epithermal Cross-section Specifications CSI001
2. Thermal Cross-section Specifications CSI002

B. Computational Modules

1. Resonance Cross Sections CSC001
2. Nonresonant Cross Sections and Fundamental-mode Spectrum CSC002

*Toppel, B. J., The Argonne Reactor Computation (ARC) System, ANL-7332 (Nov 1967).

**Just, L. C., and Sparck, S. D., The ARC System, AMD Technical Memorandum No. 157 (May 1, 1968); Sparck, S. D., and Just, L. C., A Nonautomated Environment for the ARC System, AMD Technical Memorandum No. 165 (March 1, 1968); Just, Louis, Dynamic Program Management in a Fortran Environment, AMD Technical Memorandum No. 162 (May 1968).

TABLE III.A.1 (Contd.)

B. Computational Modules (Contd.)

3. Thermal Cross Sections CSC003
4. Broad-group Cross Sections and Fundamental-mode Spectrum CSC004
5.

C. Output Edit Modules

1. Thermal Cross-section Edit CSE001
2.

II. Neutronics Calculations Modules

A. Input Modules

1. Cross-section Homogenization Specifications NUI001
2. Code-independent Specifications NUI002
3. 1D-transport Specifications NUI003
4. 2D-transport Specifications NUI004
5. Transport-mesh Refinement Specifications NUI005
6.

B. Computational Modules

1. Cross-section Homogenization NUC001
2. 1D-Diffusion k Calculation NUC002
3. 1D-Diffusion Search NUC003
4. 1D-Transport NUC004
5. 2D-Diffusion k Calculation NUC005
6. 2D-Diffusion Search NUC006
7. 2D-Transport NUC007
8. Diffusion-mesh Refinement NUC008
9. Transport-mesh Refinement NUC009
10.

C. Output Edit Modules

1. 1D-Neutronics Output Manipulation NUE001
2. 2D-Neutronics Output Manipulation NUE002
3.

III. Adjunct Calculations Modules

A. Input Modules

1. Transport Perturbation Specifications AJI001
2. Spatial Synthesis Specifications AJI002
3. Bivariate Cross-section Interpolation Specifications AJI003
4.

TABLE III.A.1 (Contd.)

III. Adjunct Calculations Modules (Contd.)

B. Computational Modules

1. 1D-Neutron Inventory AJC001
2. 2D-Neutron Inventory AJC002
3. 1D-Diffusion Perturbation AJC003
4. 2D-Diffusion Perturbation AJC004
5. Transport Perturbation AJC005
6. Spatial Synthesis AJC006
7. Group Collapse AJC007
8. Bivariate Cross-section Interpolation AJC008
9.

C. Output Edit Modules

1. Transport Perturbation Edit AJE001
2. Spatial Synthesis Edit AJE002
3. Bivariate Cross-section Interpolation Edit AJE003
4.

IV. Fuel-cycle and Depletion Calculation Modules

A. Input Modules

1. Fuel Cycle Specifications FCI001
2. Economics Specifications FCI002
3.

B. Computational Modules

1. Fuel Cycle FCC001
2. Economics FCC002
3.

C. Output Edit Modules

1. Economics Edit FCE001
2.

V. Safety and Accident Calculations Modules

A. Input Modules

1. Point Kinetics Specifications SAI001
2. Spatial Kinetics Specifications SAI002
3. Heat Transfer Specifications SAI003
4. Two-phase Coolant Flow Specifications SAI004
5. Core Compaction Specifications SAI005

TABLE III.A.1 (Contd.)

A. Input Modules (Contd.)

6. Compressible Fluid Hydrodynamics Specifications SAI006
7. Fuel-element Deformations Specifications SAI007
8. Problem Initialization Specifications SAI008
9. Fuel-coolant Interaction Specifications SAI009
10.

B. Computational Modules

1. Point Kinetics SAC001
2. Spatial Kinetics SAC002
3. Heat Transfer SAC003
4. Two-phase Coolant Flow SAC004
5. Core Compaction SAC005
6. Compressible Fluid Hydrodynamics SAC006
7. Fuel-element Deformations SAC007
8. Problem Initialization SAC008
9. Fuel-coolant Interaction SAC009
10. 2D-Weak Explosion SAC010
11.

C. Output Edit Modules

1. Point-kinetics Edit SAE001
2. Spatial-kinetics Edit SAE002
3. Heat-transfer Edit SAE003
4. Two-phase Coolant Flow Edit SAE004
5. Core Compaction Edit SAE005
6. Compressible Fluid Hydrodynamics Edit SAE006
7. Fuel-element Deformations Edit SAE007
8. Problem Initialization Edit SAE008
9. Fuel-coolant Interaction Edit SAE009
10. 2D-Weak Explosion Edit SAC010
11.

The production use of the ARC system is achieved through use of various Standard Path modules which invoke various other modules within the system. Table III.A.2 lists some of the available standard paths; in Table III.A.1, the name of the path is intended to indicate its function.

Table III.A.3 lists the modules invoked by the various standard paths and illustrates graphically the elimination of programming duplication in a modular approach. One should note also that the system provides the enormously powerful capability of a path or module invoking a standard path as well as individual computational modules, as illustrated in STP012.

TABLE III.A.2. Standard Path Modules[a]

1. 1D-Diffusion k Calculation STP001
2. 1D-Diffusion Search STP002
3. 1D-Transport STP003
4. 2D-Diffusion k Calculation STP004
5. 2D-Diffusion Search STP005
6. Burnup Diffusion STP006
7. Multigroup Cross Sections STP007
8. Resonance Cross Sections STP008
9. Spectrum Average and Group Collapsing STP009
10. Group Collapsing STP010
11. 1D-Diffusion Perturbation STP011
12. Synthesis Trial Function Generation STP012
13.

[a]All standard paths listed are in production status for user-debugging.

TABLE III.A.3. Modules Utilized in Various Standard Paths

Standard Path Module	ARC System Modules Invoked
STP001	NUI001, NUI002, NUC001, NUC002, NUE001, AJC001
STP002	NUI001, NUI002, NUC001, NUC003, NUE001, AJC001
STP003	NUI001, NUI002, NUI003, NUC001, NUC004, NUE001, AJC001
STP004	NUI001, NUI002, NUC001, NUC005
STP005	NUI001, NUI002, NUC001, NUC006
STP006	NUI001, NUI002, NUC001, NUC005, NUC006, AJC007, FCI001, FCC001
STP007	CSI001, CSC001, CSC002, CSC004
STP008	CSI001, CSC001
STP009	CSI001, CSC002, CSC004
STP010	CSI001, CSC004
STP011	NUI001, NUI002, NUC001, NUC003, AJC003
STP012	STP001

As in all programming efforts, effective debugging can be accomplished only through interaction with users. This is, of course,

a rather unpleasant time from the user's point of view, but experience to date has shown that it is an inevitable stage in development of a production code tool.

Table III.A.4 provides comments concerning the state of the various modules listed in Table III.A.1. By way of clarification, the following labels are intended to indicate the various levels in the life of a code algorithm in order of increasing completeness:

(i) not initiated;
(ii) algorithm and interfaces specified, programming not initiated;
(iii) programmer-development;
(iv) programmer-debugging;
(v) production; user-debugging;
(vi) production.

TABLE III.A.4. Status of ARC System Modules

Module	Comments
CSI001	Production
CSI002	Interfaces specified, programming not initiated
CSC001	Production
CSC002	Production
CSC003	Algorithm specified, programming not initiated
CSC004	Production
CSE001	Algorithm specified, programming not initiated
NUI001	Production
NUI002	Production use except for external source calculations
NUI003	Production
NUI004	Interfaces specified, programming not initiated
NUI005	Not initiated
NUC001	Production
NUC002	Production; user-debugging; all options available except internal general-interface conditions
NUC003	Production; user-debugging; all options available except internal general-interface conditions
NUC004	Production; user-debugging; all options available except linearly anisotropic scattering option under programmer-debugging
NUC005	Production; user-debugging; all options available except periodic boundary conditions, internal general-interface conditions, kinetics option
NUC006	Production; user-degugging; all options available except periodic boundary conditions, internal general-interface conditions, kinetics option
NUC007	Programmer development; inner iteration loop being programmer-debugged
NUC008	Programmer-debugging
NUC009	Not initiated
NUE001	Production; user-debugging
NUE002	Not initiated
AJI001	Not initiated
AJI002	Not initiated
AJI003	Not initiated
AJC001	Production; user-debugging
AJC002	Not initiated
AJC003	Production; user-debugging; all options available except calculation of effective delayed neutron fractions
AJC004	Programmer development and debugging
AJC005	Algorithm specified, programming not initiated
AJC006	Various algorithms specified, under programmer-debugging
AJC007	Programmer-debugging
AJC008	Not initiated
AJE001	Not initiated
AJE002	Not initiated
AJE003	Not initiated
FCI001	Programmer development of improved user formats
FCI002	Not initiated
FCC001	Production; user-debugging for equilibrium option; programmer development for nonequilibrium options
FCC002	Not initiated
SAI001 ↓ SAI009	Substantial CDC-3600 programming exists having production user-debugging status,[a] which will form the basis for various modules in the Safety and Accident Calculations area
SAC001 ↓ SAC010	
SAE001 ↓ SAE010	

[a]Reactor Physics Division Annual Report July 1, 1966 to June 30, 1967, ANL-7310 (January 1968) Sections IV and VI.

All of the standard-path modules are assumed to be in the state of production user-debugging.

Persons familiar with programming generally agree that no code ever reaches a state of completeness implied by level (vi) above.

(ii) The RABBLE Code. Users of the RABBLE program* have found that for problems in which the resonance escape probability is small, negative fluxes or negative resonance escape probabilities are sometimes computed. The difficulty arises because of the buildup of errors in the calculation of regional slowing-down sources as thousands of fine groups are covered. The slowing-down density is now being used to try to correct the slowing-down source.

In RABBLE, the lethargy range of interest is divided into many very narrow intervals of constant width, called fine groups. These fine groups are taken to be so narrow that it can be assumed that a neutron suffers only one collision within a fine group and that the collision density is independent of lethargy within a fine group. With these assumptions, the source for some region in the k'th fine group, which extends from u to $u + \Delta u$, can be written as

$$S_k = \int_{u-\epsilon}^{u} du' \frac{F_s(u')}{1 -} e^{-(u-u')} = \int_{u-\epsilon}^{u} du' F_s(u') P(u' \rightarrow u), \qquad (1)$$

where $F_s(u')$ is the scattering rate, $P(u' \rightarrow u)$ is the probability of a neutron being scattered from u' to u and where, for simplicity of notation, we have assumed that there is only one species of scatterer present. When the range of integration is broken up into the fine groups it can be shown that

$$S_k = e^{-\Delta u} S_{k-1} + P_1 F_{s,k-1} - e^{-\Delta u} P_L F_{s,k-L-1}, \qquad (2)$$

where P_n is the probability that a neutron is scattered down in n fine groups and L is the maximum number of groups through which a neutron can be scattered. If more than one species of scatterer is present, the last two terms in Eq. (2) are summed over the number of scatterers. Although S_k can be evaluated rapidly by use of Eq. (2), it cannot be evaluated exactly because L can be very large so that $F_{s_{k-L-1}}$ cannot be stored. Instead, we take $F_{s_{k-L-1}}$ to be the average fine-group scattering for the intermediate group in which fine group k-L-1 is located. This unavoidable approximation must contribute significantly to the errors in S_k.

*Kier, P. H., and Robba, A. A., ANL-7326 (April 1967).

A useful quantity in the study of the slowing down of neutrons is the slowing-down density q(u), which is defined as the rate with which neutrons are slowed down past lethargy u. It is given by

$$q_k = q(u) = \int_{u-\epsilon}^{u} du' \frac{F_s(u')}{1-\alpha} \left\{ e^{-(u-u')} - \alpha \right\}. \tag{3}$$

Upon comparison of Eqs. (1) and (3), it is seen that

$$q_k = S_k - \frac{\alpha}{1-\alpha} \int_{u-\epsilon}^{u} F_s(u')du' = S_k - h_k, \tag{4}$$

where h_k satisfies the following recursion relationship:

$$h_k = h_{k-1} + F_{s_{k-1}} \Delta u - F_{s,k-L-1} \Delta u. \tag{5}$$

Just as there is some error in Eq. (2) for S_k, there should be some error in Eq. (4) for q_k.

However, it is possible to use neutron conservation to compute the slowing-down density. The change in the slowing-down density in crossing a fine group is the sum of the absorption rate and the net leakage out of the region:

$$q_k^* = q_{k-1}^* - \Delta u \left\{ F_{a_{k-1}} + J_{net} \right\}. \tag{6}$$

We can consider q_k^* to be exact because it is computed from neutron conservation, and we can therefore find the error δq_k in q_k. However we desire the error δS_k in S_k, and unfortunately there seems to be no rigorous procedure to obtain δS_k from δq_k.

Several relationships between δS_k and δq_k have been tried. A simple relation, namely, $\delta S_k / \delta q_k = S_k / q_k$, has been found to remove negative resonance escape probabilities for some problem but not all. Other relationships are now being tested.

(iii) Space-Time Synthesis. The development of variational space-time synthesis methods which admit trial functions that are discontinuous in space and time has received considerable attention in recent years. The time-discontinuous trial-function treatments parallel the general formalism developed by Pomraning.† The successful applications of the Pomraning-type functional have used a class of discontinuous trial

†Pomraning, G. C., J. Nucl. Energy 20, 617 (1966).

functions which yield a set of Euler-Lagrange equations in a finite difference form.† It can be shown, however, that if a general class of time-discontinuous trial functions is used in a semidirect approach, the resulting set of differential equations and associated boundary and continuity conditions in the time-dependent mixing functions have only the trivial solution. This difficulty is similar to that which exists with the Selengut-Wachspress (S-W) functional†† for spatially discontinuous trial functions in the time-independent case. Buslik‡ illustrates this difficulty with the S-W principle and points out that if trial functions which yield a finite difference form are used, the difficulty does not appear.

In the following paragraphs, a Pomraning-type functional for prompt-neutron diffusion theory in multigroup form is used to illustrate the basic difficulty in time-discontinuous synthesis, and a modified variational principle is proposed which does not exhibit this difficulty.

A variational principle for prompt-neutron diffusion theory [based on Eq. (28) of Pomraning]‡‡ can be written:

$$J_p[u^*,u] = \int_V dV \int_{\bar{\tau}} dt \left[u^* v^{-1} \frac{\partial u}{\partial t} + \nabla u^* \cdot D \nabla u - u^* H u \right]$$

$$+ \int_V dV \left\{ [u^* v^{-1}(u - f)]_{t=t_0} - [f^* v^{-1} u]_{t=t_f} \right\}$$

$$+ \frac{1}{2} \int_V dV \left\{ [u^*(+) + u^*(-)]\, v^{-1} [u(+) - u(-)] \right\}, \qquad (1)$$

where trial functions may be used that are discontinuous at $t = \tau$. The symbol $\bar{\tau}$ indicates integration over the continuous portions of the interval from t_0 to t_f; the quantities $u(-)$ and $u(+)$ denote limiting values of u before and after $t = \tau$, respectively; the functions f and f^* are chosen values for the initial and final flux and adjoint flux distributions, respectively. The matrix H includes absorption, scattering, and fission terms in the multigroup notation of Köhler,§ and u and u^* are appropriately taken to be row and column vectors. In the interest of simplicity, spatial boundary conditions will not be considered.

---

†Yasinsky, J. B., Nucl. Sci. Eng. 29, 381 (1967); Stacey, W. M., ibid. 34, 45 (1968).

††Wachspress, E. L., and Becker, M., in Proc. Conf. Appl. Comp. Methods to Reactor Problems, ANL-7050 (1965).

‡Buslik, A. J., WAPD-TM-610 (1966).

‡‡Pomraning, G. C., J. Nucl. Energy 20, 617 (1966).

§Köhler, W. H., Nukleonik 4A, 203 (1966).

The conditions for the functional in Eq. (1) to be stationary for arbitrary variations in δu and δu^* are

$$\int_V dV \int_{\overline{\tau}} dt\, \delta u^* \left[v^{-1} \frac{\partial u}{\partial t} - \nabla \cdot D \nabla u - Hu \right] = 0; \tag{2}$$

$$\int_V dV\, \delta u^* \Big|_{t_0} v^{-1}(u - f) \Big|_{t_0} = 0; \tag{3}$$

$$\int_V dV [\delta u^*(+) + \delta u^*(-)]\, v^{-1} [u(+) - u(-)] = 0; \tag{4}$$

$$\int_V dV \int_{\overline{\tau}} dt\, \delta u \left[v^{-1} \frac{\partial u^*}{\partial t} + \nabla \cdot D \nabla u^* + H^* u^* \right] = 0; \tag{5}$$

$$\int_V dV\, \delta u \Big|_{t_f} v^{-1}(u^* - f^*) \Big|_{t_f} = 0; \tag{6}$$

$$\int_V dV [\delta u(+) + \delta u(-)]\, v^{-1} [u^*(+) - u^*(-)] = 0. \tag{7}$$

The conditions stated in Eqs. (2) and (5) give the diffusion equation and its adjoint valid over the continuous portions of the time interval. In Eq. (5), H^* is used to indicate that it now includes the adjoints of the fission and scattering kernels. Equations (3) and (6), respectively, give the following initial and final value conditions on the flux and adjoint flux:

$$\phi = f \text{ at } t = t_0; \tag{8}$$

$$\phi^* = f^* \text{ at } t = t_f. \tag{9}$$

The difficulties with this functional appear in the temporal continuity conditions specified by Eqs. (4) and (7).

In order to illustrate these difficulties, the following synthesis approximations will be used:

$$u_\ell(\underline{r},t) = \sum_{i=1}^{N_\ell} G_{\ell i}(\underline{r}) T_{\ell i}(t); \tag{10}$$

$$u^*(\underline{r},t) = \sum_{i=1}^{N_\ell} T^*_{\ell i}(t) G^*_{\ell i}(\underline{r}), \tag{11}$$

where $G_{\ell i}$ and $G^*_{\ell i}$ are trial functions that may be discontinuous at $t = \tau$, $T_{\ell i}$ and $T^*_{\ell i}$ are time-dependent mixing functions to be determined, and $\ell = 1$ and $\ell = 2$ denote the respective time intervals $t_0 \le t \le \tau - \epsilon$ and $\tau + \epsilon \le t \le t_f$ for $\epsilon > 0$. Only Eqs. (2),(3), and (4) will be considered in detail.

The original space-time-dependent partial differential equations of second order, specified by Eq. (2), are reduced to first-order ordinary differential equations in the mixing functions $T_{\ell i}$, giving in matrix form

$$W_{11} \frac{dT_1(t)}{dt} - K_{11} T_1(t) = 0; \quad t_0 \le t \le \tau - \epsilon; \tag{12}$$

$$W_{22} \frac{dT_2(t)}{dt} - K_{22} T_2(t) = 0; \quad \tau + \epsilon \le t \le t_f, \tag{13}$$

and the initial condition specified by Eq. (3) becomes

$$W_{11} T_1 = F; \quad t = t_0, \tag{14}$$

where $W_{\ell\ell}$ is a $N_\ell \times N_\ell$ matrix with elements

$$[W_{\ell\ell}]_{ij} \equiv \int_V G^*_{\ell i}(\underline{r}) v^{-1} G_{\ell j}(\underline{r})\, dV; \quad \ell = 1, 2; \tag{15}$$

$K_{\ell\ell}$ is a $N_\ell \times N_\ell$ matrix with elements

$$[K_{\ell\ell}]_{ij} \equiv \int_V G^*_{\ell i}(\nabla \cdot D\nabla + H) G_{\ell j}\, dV; \quad \ell = 1, 2; \tag{16}$$

F is a column vector with N_1 elements

$$[F]_j \equiv \int_V G^*_{1j}(\underline{r}) v^{-1} f(\underline{r})\, dV; \tag{17}$$

T (t) is a column vector of N_ℓ elements $T_{\ell i}$; $\ell = 1, 2$. Similarly, Eq. (4) can be written as

$$\delta T_2^*(\tau+\epsilon)\left[W_{22}T_2(\tau+\epsilon) - \Lambda_{21}T_1(\tau-\epsilon)\right]$$

$$+ \delta T_1^*(\tau-\epsilon)\left[\Lambda_{12}T_2(\tau-\epsilon) - W_{11}T_1(\tau-\epsilon)\right] = 0, \tag{4a}$$

where Λ_{mn} is a $N_m \times N_n$ matrix with elements

$$[\Lambda_{mn}]_{ij} \equiv \int_V G_{mi}^*(\underline{r})v^{-1}G_{nj}(\underline{r})\,dV \tag{18}$$

for m,n = 1, 2 ($m \neq n$).

In Eq. (4a), $\delta T_2^*(\tau+\epsilon)$ and $\delta T_1^*(\tau-\epsilon)$ are clearly independent and arbitrary variations resulting not in one necessary continuity condition, but rather in the following two conditions:

$$W_{22}T_2(\tau+\epsilon) = \Lambda_{21}T_1(\tau-\epsilon); \tag{19}$$

$$\Lambda_{12}T_2(\tau+\epsilon) = W_{11}T_1(\tau-\epsilon). \tag{20}$$

The differential equations (12) and (13) are now overspecified by the conditions of Eqs. (14), (19), and (20), and in general only the trivial solutions exist. This same fundamental difficulty arises in the solution of the system of equations for the adjoint mixing functions T_1^* and T_2^*, with Eq. (7) specifying the conditions

$$\Lambda_{12}^T T_2^*(\tau+\epsilon) = W_{11}^T T_1^*(\tau-\epsilon); \tag{21}$$

$$W_{22}^T T_2^*(\tau+\epsilon) = \Lambda_{21}^T T_1^*(\tau-\epsilon), \tag{22}$$

where the superscript T indicates the transpose of matrices previously defined.

Functionals of the general form of Eq. (1) are therefore clearly usable only for a rather limited choice of trial functions and a modification of this functional is in order.

By way of justifying the final form of the functional to be presented below, the following observations can be made concerning the set of Eqs. (12), (13), (14), and (19). The differential Eq. (12) together with Eq. (14) form a well-determined initial-value problem in $T_1(t)$ for the time interval $t_0 \leq t \leq \tau - \epsilon$. With $T_1(\tau-\epsilon)$ now known, Eq. (19) becomes a set of N_2 algebraic equations in the N_2 unknowns $T_{2i}(\tau+\epsilon)$, and the $T_{2i}(\tau+\epsilon)$ so determined are just the initial-value conditions for the differential Eq. (13). Thus, the system of equations for the functional of Eq. (1) can be

rendered usable by discarding the condition imposed by Eq. (20). The elimination of Eq. (20) rather than Eq. (19) is not an arbitrary choice. Equation (20) for an initial-value problem represents a set of N_1 algebraic equations in the N_2 unknowns $T_{2i}(\tau + \epsilon)$, and thus is meaningful only for the special case $N_1 = N_2$. However, Eq. (20) is of the same form as Eq. (21) of the adjoint problem. The adjoint problem is a final-value problem, and Eq. (21) is a set of N_1 algebraic equations in the N_1 unknowns $T^*_{1i}(\tau - \epsilon)$. Thus, in the adjoint problem, Eq. (22) must be discarded.

The following functional is a proposed modification of the functional of Eq. (1):

$$J[u^*,u] = \int_V dV \int_{\overline{\tau}} dt \left[u^* v^{-1} \frac{\partial u}{\partial t} + \nabla u^* \cdot D \nabla u - u^* H u \right]$$

$$+ \int_V dV \left\{ [u^* v^{-1}(u - f)]_{t=t_0} - [f^* v^{-1} u]_{t=t_f} \right\}$$

$$+ \int_V dV \left\{ u^*(+) v^{-1} [u(+) - u(-)] \right\}. \tag{23}$$

Since the first two integrals have remained unchanged, the conditions for J to be stationary are the same as those specified in Eqs. (2), (3), (5), and (6), and the conditions which replace those of Eqs. (4) and (7) are

$$\int_V dV \left\{ \delta u^*(+) v^{-1} [u(+) - u(-)] \right\} = 0; \tag{24}$$

$$\int_V dV \left\{ \delta u(-) v^{-1} [u^*(+) - u^*(-)] \right\} = 0. \tag{25}$$

If the synthesis approximations of Eqs. (10) and (11) are used, the following well-determined system of equations is obtained:

$$W_{11} \frac{dT_1}{dt} - K_{11} T_1 = 0; \quad t_0 \le t \le \tau - \epsilon; \tag{12}$$

$$W_{22} \frac{dT_2}{dt} - K_{22} T_2 = 0; \quad \tau + \epsilon \le t \le t_f; \tag{13}$$

$$W_{11} T_1 = F; \quad t = t_0; \tag{14}$$

$$W_{22}T_2(\tau + \epsilon) = \Lambda_{21}T_1(\tau - \epsilon); \tag{19}$$

$$W_{11}^T \frac{dT_1^*}{dt} + K_{11}^{*T} T_1^* = 0; \quad t_0 \le t \le \tau - \epsilon; \tag{26}$$

$$W_{22}^T \frac{dT_2^*}{dt} + K_{22}^{*T} T_2^* = 0; \quad \tau + \epsilon \le t \le t_f; \tag{27}$$

$$W_{22}^T T_2^* = F^*; \quad t = t_f; \tag{28}$$

$$W_{11}^T T_1^*(\tau - \epsilon) = \Lambda_{12}^T T_2^*(\tau + \epsilon), \tag{21}$$

where F^* is a column vector with N_2 elements

$$[F^*]_j \equiv \int_V f^*(\underline{r}) v^{-1} G_{2j}(\underline{r})\, dV. \tag{29}$$

$K_{\ell\ell}^*$ is of the same form as that of Eq. (16), but H must be replaced by H^*. Some of the earlier equations have been repeated in this array for completeness purposes.

The new variational principle of Eq. (23) has been shown to lend itself to the most general application of the semidirect method with time-discontinuous trial functions while exhibiting none of the inconsistencies of Eq. (1).

Although spatial boundary conditions have not been considered in this treatment, they present no particular difficulty. The functional is easily extended to include multiple interfaces in time, and to also include delayed neutrons and precursors with no loss of generality.

2. Nuclear Data--Research and Development

a. Cross Section Measurements (C. E. Crouthamel and N. D. Dudey)

Last Reported: ANL-7500, pp. 91-92 (Sept 1968).

(i) Monoenergetic Neutron Cross Section Measurements. Experiments to measure the neutron-capture cross sections of ^{51}V and ^{50}Ti as a function of neutron energy have been completed. A detailed report of these measurements has been written for publication.

(ii) Integral Cross Section Measurements. Data analysis has been completed for (n,γ), (n,p), and (n,α) reactions in stainless steel

specimens irradiated in EBR-II. Production rates of ^{55}Fe, ^{54}Mn, ^{58}Co, ^{60}Co, and ^{63}Ni, given in atoms per megawatt-day per gram of Type 304L stainless steel, are shown in Fig. III.A.1 for 8 radial locations in EBR-II. The data obtained in this study provided a means of measuring the total neutron flux per megawatt in EBR-II. Our value of $4.9 \times 10^{13}\ \phi/MW$ at full power (50 MW) is in good agreement with a value of $5.06 \times 10^{13}\ \phi/MW$ at 20 kW reported by Jackson and Ulseth.* These values are also in good agreement with a diffusion-theory calculation. From these data it is concluded that, within experimental error, the total flux per megawatt is independent of reactor power.

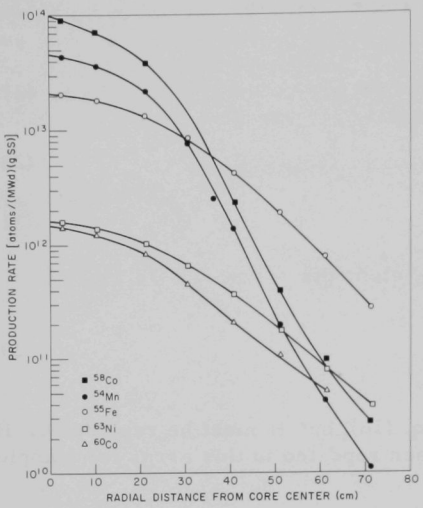

Fig. III.A.1. Specific Atom-production Rates in Type 304L Stainless Steel as a Function of Irradiation Position in EBR-II

The measurements performed in this study indicate that ^{54}Fe can be a very sensitive monitor of fast-reactor neutron flux and neutron-energy spectrum. The $^{54}Fe(n,\gamma)^{55}Fe$ reaction is sensitive to neutron energies between ~1 keV and 1 MeV; the $^{54}Fe(n,p)^{54}Mn$ reaction, to energies between ~1 and 8 MeV. The latter reaction has previously been recognized as a reliable flux and fluence monitor. The sensitivity of the atom ratio $^{54}Mn/^{55}Fe$ as a "spectral hardness" indicator is demonstrated in Table III.A.5 for measurements at 8 radial positions in EBR-II; included in the table, for comparison, are the median neutron energies calculated by diffusion theory.

TABLE III.A.5. "Spectral Hardness" Indicator in EBR-II: Atom Ratio $^{54}Mn/^{55}Fe$ Produced from ^{54}Fe

Radial Position[a] (cm)	Atom Ratio $^{54}Mn/^{55}Fe$	Calculated Median Neutron Energy (keV)	Radial Position[a] (cm)	Atom Ratio $^{54}Mn/^{55}Fe$	Calculated Median Neutron Energy (keV)
2.86	2.18	470	40.83	0.320	206
10.21	1.98	465	51.03	0.102	
21.25	1.63	405	61.24	0.056	140
30.62	0.893	320	71.45	0.040	

[a]Distance from core center.

The analysis of Ti, V, S, Fe, Ni, Co, Sc, Cu, and Au samples irradiated in an EBR-II Dosimetry Test experiment is nearing

*Jackson, J. L., and Ulseth, J. A., Nucl. Appl. 5, 275 (1968).

completion. It is anticipated that production rates and spectrum-averaged cross sections for more than 20 (n,γ), (n,p), (n,α), and (n,2n) reactions will be determined from this study. Preliminary data indicate that the total neutron flux per megawatt, measured in this experiment at 91.5 kW, is identical to the value measured at 50 MW; this finding supports the previously stated conclusion that the total flux per megawatt is independent of reactor power.

(iii) Low-mass Fast-neutron Fission Yields. Assembly and calibration of the equipment to measure low-mass fission yields is proceeding on schedule. Minor modifications to some of the electronic modules have been required; however, the system is expected to be operational by the time the new ANL neutron generator is available for use.

b. Burnup Analysis and Fission Yields for Fast Reactors (R. P. Larsen)

(i) Supplemental Determination of Absolute Fission Yields of Burnup Monitors for Fast Reactor Fuels

Last Reported: ANL-7500, p. 94 (Sept 1968).

Plans are being made to carry out an irradiation in EBR-II to provide additional material for fission-yield determinations (see Progress Report for July 1968, ANL-7478, pp. 93-94. One-hundred-milligram quantities of various fissionable isotopes will be irradiated in driver subassemblies for one full fuel cycle (90-120 days). It was initially planned to determine the number of fissions occurring in the samples by analyzing for each of the heavy fission products and summing the number of fission product atoms produced.

It now appears that the number of fissions can be more readily determined if a short irradiation (1 to 2 hr at a 50-kW power level) is carried out in conjunction with the full-fuel cycle irradiation. In the short irradiation, fission foils and fission track counters of the type described in the Progress Report for November 1968, ANL-7518, p. 81 would be employed. The short-irradiation experiment would provide the data necessary to establish a factor relating the counts of a particular fission product, e.g., cerium-144 (285 days) or ruthenium-106 (365 days), to the number of fissions that occurred. In the full-cycle irradiation, identical fission foils would be encapsulated with the 100-mg samples of fissionable isotopes. These foils would be counted for the same fission product, and the number of fissions calculated using the factor obtained in the short irradiation.

Because this technique is new and has not been tested, it is planned to evaluate it by measuring the thermal-fission yield of

cesium-137 from uranium-235, a yield which has been well-established by other techniques. This irradiation will probably be carried out in either CP-5 or Juggernaut.

c. Reactor Code Center (M. Butler)

Last Reported: ANL-7518, p. 84 (Nov 1968).

R. Prescott of the ENEA Computer Programme Library, Ispra, Italy, spent two weeks at the Code Center during the past month testing the IBM-360 versions of programs abstracted in Supplement 1 to ANL-7411, Compilation of Program Abstracts. This first supplement is being readied for distribution.

Three new programs have been added to our library during December: 352, RAUMZEIT, a time-dependent one-dimensional diffusion program for the CDC-6600 submitted by KAPL; 353, SWELL2, a fuel-element-lifetime study prepared for Argonne for the CDC-3600; and 354, CINCAS, a fuel-cycle economy, accounting, and forecasting program for the IBM 360 submitted by Commonwealth Edison. In addition, an IBM-360 version of 275, PDQ7, was received from IBM. These four programs are now ready for distribution upon request.

A Directory of Cooperating Installations is being prepared for publication as ANL-7497 and is expected to be distributed shortly. This initial issue of the directory contains the installation facilities reports for 73 of the cooperating installations.

B. Reactor Fuels and Materials Development

1. Fuels and Cladding

a. Research and Development

(i) Behavior of Reactor Materials

(a) Fission Gas Behavior in Uranium-Plutonium-Carbide Fuels (L. C. Michels)

Last Reported: ANL-7513, pp. 102-103 (Oct 1968).

The technique developed for the preparation of thin sections of carbide fuels for transmission electron microscopy (see Progress Report for September 1968, ANL-7500, p. 98) has been modified. The zinc embedding material, although quite suitable for other reasons, would not penetrate the microcracks in the carbides being used; consequently, pieces of the carbide specimens would break loose either during or after preparation. However, an epoxy resin, Araldite,* was found to be a suitable impregnant for the carbide specimens. The modified technique consists of (1) immersion of the carbide specimen (approximately 0.062 in. in diameter by 0.020 in. thick) in Araldite in a Teflon mold, (2) evacuation of the composite to 0.025 Torr for about 15 min to remove gases from the microcracks in the carbide specimen as well as dissolved gases from the Araldite, (3) application of a hydrostatic pressure of 100 psi (using argon gas), and (4) heating to 100°C under pressure for 2 hr to set and cure the Araldite. This procedure produces complete penetration of the microcracks by the epoxy as well as a sound epoxy-carbide interface bond.

After ejection from the Teflon mold, the composite specimen is ground on abrasive paper to a thickness of about 0.005 in. and then thinned by using an electrolytic double-jet technique. In order to circumvent the need to make a mechanical-electrical contact to the specimen (which would be rather difficult with the epoxy mount), one jet of electrolyte is made the anode and the other jet the cathode. The polarity of the polishing current is periodically reversed during polishing, according to the method suggested by Bainbridge.** Using the jets as electrical contacts will also allow the application of this technique to oxides and eliminate the problem of a mechanical-electrical contact normally encountered with high-resistivity material. Satisfactory thin sections of UC have been obtained by using this technique.

*Product of the Ciba Products Company.

**Bainbridge, J. E., AERE-R-5677 (Jan 1968).

(ii) Thermodynamics of Fuel Materials

(a) Vapor Species Partial Pressures in the Ternary U-Pu-C System (J. E. Battles)

Last Reported: ANL-7500, p. 98 (Sept 1968).

Mass-spectrometric studies of the volatilization behavior of the U-Pu-C system are being conducted to determine (1) the apparent composition of the vapor phase in equilibrium with the condensed phase(s), (2) the partial pressures of the vapor species as a function of temperature, and (3) the thermodynamic properties of the vapor species and condensed phases.

The binary Pu-C system is being investigated first to establish the relationships between the vapor and condensed phases. These relationships will be helpful in the study of the ternary U-Pu-C system. In the Pu-C system, there are, at selected temperatures, four thermodynamically invariant two-phase fields consisting of solids only: PuC + Pu_2C_3, Pu_2C_3 + C, Pu_2C_3 + PuC_2, and PuC_2 + C.

Mass-spectrometric analysis of the vapor phase in equilibrium with the condensed systems Pu_2C_3 + C and Pu_2C_3 + PuC_2, in the temperature ranges from 1365 to 1750°C and from 1750 to 2026°C, respectively, showed only the presence of Pu(g). No evidence was found for PuC(g) or PuC_2(g), which indicated that their abundance in the vapor phase, if they were present at all, was less than 0.1% at the higher temperatures. (Olsen and Mulford* reported about 0.1% PuC_2(g) in the vapor phase over condensed Pu_2C_3 + C at 1990°K.) Our results, coupled with X-ray diffraction analysis of the sample residues, indicate that vaporization of Pu(g) from the condensed phases proceeds mainly according to the reactions

$$1/2Pu_2C_3(s) = Pu(g) + 3/2C(s)(<1750°C) \quad (1)$$

and

$$2Pu_2C_3(s) = Pu(g) + 3PuC_2(s)(>1750°C). \quad (2)$$

However, the composition limits of the two-phase regions Pu_2C_3-C and Pu_2C_3-PuC_2 are unknown. Tungsten effusion cells were used in both the measurements of temperature dependency and rates of effusion without any apparent reaction with the samples.

The temperature dependence of Pu^+(g) in equilibrium with the condensed phases has been determined in two series of measurements for Reaction (1) and four series of measurements for Reaction (2).

*Olsen, W. M., and Mulford, R. N. R., "Thermodynamics of Plutonium Carbides," Thermodynamics of Nuclear Materials, IAEA, Vienna (1967), p. 467.

The heats of reaction calculated from the slopes of the lines of log IT versus 1/T are 98.2 ± 1.1 and 116.0 ± 1.8 kcal/mol Pu(g) for Reactions (1) and (2), respectively.

Vapor pressures of 1.12×10^{-6} atm at 1746°C for Reaction (1) and 4.98×10^{-6} atm at 1854°C for Reaction (2) were determined from measurements of the rate of mass effusion (weight-loss method). When these values of the vapor pressures and the slopes of the temperature-dependence data are used to evaluate the intercepts, the following equations for the vapor pressures as a function of temperature are derived for Reactions (1) and (2), respectively:

$$\log P(\text{atm}) = -\frac{21{,}470 \pm 230}{T} + (4.686 \pm 0.118)(1365\text{-}1750°C); \qquad (3)$$

$$\log P(\text{atm}) = -\frac{25{,}360 \pm 400}{T} + (6.620 \pm 0.191)(1750\text{-}2026°C). \qquad (4)$$

The errors indicated for the intercepts of Eqs. (3) and (4) are the standard deviations in the slopes combined with an estimated standard deviation of 7% in the measurement of the mass-effusion rates. Equation (3) agrees reasonably well with that of Olsen and Mulford,* namely, $\log P(\text{atm}) = (4.39 \pm 0.08) - (20{,}330 \pm 140)/T$. The condensed $Pu_2C_3 + PuC_2$ system has not been previously studied.

Measurements of rates of effusion and temperature dependence are currently being conducted on the condensed $PuC_2 + C$ system. Since Olsen and Mulford as well as others have investigated the $PuC\text{-}Pu_2C_3$ system, our results for the $PuC_2 + C$ system should complete the characterization of the volatilization behavior of the entire Pu-C system.

2. Coolants, Moderators, and Control Materials--Fundamentals of Corrosion in Liquid Metals

a. Corrosion Mechanisms (D. L. Smith)

Last Reported: ANL-7518, pp. 90-91 (Nov 1968).

The equilibrium distribution coefficients for oxygen between the Group-V refractory metals and liquid sodium are being determined. The experimental measurement requires accurate analyses for oxygen in sodium at concentrations below 20 ppm. The principal method has been by vacuum distillation of the sodium and titration of the hydrolized residue with dilute hydrochloric acid. In some cases the sodium in the hydrolized residue has also been measured by flame photometry. Both techniques require a knowledge of the composition of the residue, since the oxygen content is

*Ibid., see previous page.

determined from the alkalinity or sodium content of the residue. The oxygen in the sodium has been controlled by circulation through a cold trap filled with stainless steel mesh. The cold-trap temperature has been varied from 103 to 240°C. These temperatures correspond to a calculated oxygen solubility in sodium of 0.30 to 30.2 ppm, according to the equation given by Kassner and Smith* and derived from the data of Rutkauskas** and of Noden and Bagley.†

Figure III.B.1 is a plot of the results of the oxygen analyses obtained as a function of reciprocal cold-trap temperature. These data were obtained by titration of the hydrolized residue to pH 4.7. Also included in the figure are the solubility data of Rutkauskas. The original assumption was made that the residue consisted of Na_2O and Na_2CO_3. Other sodium compounds such as NaH and Na_3N were believed to dissociate at the distillation temperature. The titration of Na_2CO_3 occurs in two steps:

$$Na_2CO_3 + HCl \rightarrow NaHCO_3 + NaCl;$$

$$NaHCO_3 + HCl \rightarrow H_2CO_3 + NaCl.$$

The first reaction is completed by pH 7.7 and the second by pH 4.7. Since titration of the NaOH obtained from hydrolysis of the Na_2O residue is completed at pH 7.7, the amount of Na_2O and Na_2CO_3 can be determined from a titration to pH 4.7. Any Na_2CO_3 observed in the titration may have come from either the sodium or from contamination of the Na_2O by CO_2 during transport or titration. Normally, the residue was kept in an inert

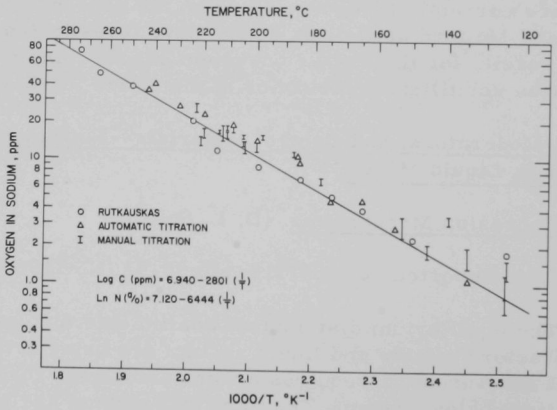

Fig. III.B.1. Vacuum Distillation Analysis of Oxygen in Sodium as a Function of Cold-trap Temperature

*Kassner, T. F., and Smith, D. L., ANL-7335 (1967).

**Rutkauskas, V. J., LA-3524-MS (1966).

†Noden, J. D., and Bagley, K. A., UKAEA Report TN-80 (1958).

atmosphere during transport, hydrolysis, and titration. When the sample was handled carefully, the amount of acid required for the $NaHCO_3$ titration (pH 7.7 to pH 4.7) was usually less than 5% of the acid required for titration to pH 7.7. The $NaHCO_3$ titration was frequently about equal to the water-blank titration. When the residue was intentionally or inadvertently exposed to the atmosphere during transport, hydrolysis, or titration, a significantly larger proportion of the acid was required to titrate from pH 7.7 to pH 4.7. We concluded that the sodium from this system does not contain a detectable amount of Na_2CO_3. The values of oxygen given in Fig. III.B.1 were obtained by assuming that all of the sodium titrated to pH 4.7 was in the form of Na_2O in the residue. Note that the high-temperature portion of the system was at 600 or 700°C for a long period of time, and that Na_2CO_3 has been reported to be unstable at these temperatures.*

The possible loss of Na_2CO_3 during distillation has been tested. The sodium is typically distilled in a vacuum of better than 10^{-3} Torr at a temperature of ~325°C for 2 hr. The temperature is then increased over a 30-min period to above 440°C. When the maximum distillation temperature was less than 440°C, larger amounts of sodium were titrated than for similar samples distilled to higher temperatures. The excess sodium apparently comes from a sodium compound that decomposes at the higher distillation temperatures. This compound may be unstable at the lower distillation temperatures, with the presence of the compound controlled by the kinetics of the decomposition process. Titration of the residues from the lower-temperature distillations indicated that the excess sodium does not come from Na_2CO_3. Off gases collected during distillation will be analyzed by gas chromatography in an attempt to determine the sodium compound.

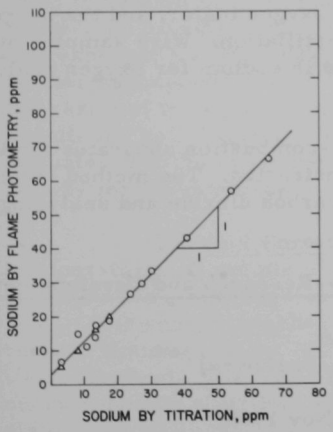

Fig. III.B.2 Comparison of Sodium Analyses of Vacuum Distillation Residue

Since calcium in the distillation residue could cause an error in the oxygen analysis, the presence of calcium in several hydrolyzed residues was measured by flame photometry. No calcium was detected in any of the samples tested (the detection limit is below 1 ppm calcium). The presence of calcium in the form of CaO in the residue would decrease the oxygen in sodium, as measured by flame-photometric analysis based on Na_2O. Several of the hydolyzed residues were also analyzed for sodium by flame photometry. Figure III.B.2 is a plot of the total sodium obtained by the flame-photometric analysis versus the total sodium obtained by titration. The curve indicates that the flame-photometric analysis gives 3 ppm more sodium at each concentration.

*Kelley, K. J., et al., CNLM-6337 (1965).

This would indicate that a sodium compound, unaffected by the cold-trap temperature, is present in the residue and that the compound is not detectable by titration of the hydrolyzed residue.

b. Corrosion Inhibition by Dissolved Getters in Liquid-sodium Environment (K. Natesan, C. A. Youngdahl, and W. McFall)

Last Reported: ANL-7500, p. 99 (Sept 1968).

(i) Calcium Additives. Dissolved getters in sodium are being investigated as a means of controlling the oxygen activity in sodium. Since elements such as calcium interact with oxygen to form an oxide (CaO) more stable than Na_2O, both the activity and the concentration of oxygen in sodium is decreased. Calcium additives will be studied to determine quantitatively the effect of calcium on the solubility of oxygen in sodium and to determine experimentally the Gibbs free-energy-interaction coefficients in the Na-O-Ca system.

For these studies, sodium with different calcium concentrations will be equilibrated in a molybdenum crucible at 500, 600, and 700°C for 3 hr, and the oxygen will be analyzed by vacuum distillation. At present, analytical and recovery techniques for Ca are being developed.

An apparatus for detailed studies of the Na-O-Ca system is being constructed. The apparatus consists of a high-purity molybdenum pot (of $5\frac{1}{4}$-in. OD by 9 in. long) containing about 0.6 gal of sodium. The oxygen activity in sodium will be measured by a UNC oxygen meter, and the oxygen concentration will be determined by vacuum distillation. Wire samples of vanadium or tantalum will also be equilibrated in sodium for oxygen analysis by internal-friction techniques.

(ii) Carbon Determination. A dry-combustion apparatus for the analysis of total carbon in sodium is being constructed. The method involves conversion of all the carbon in the sample to carbon dioxide and analyzing the evolved gas by chromatography.

3. Radiation Damage on Structural Materials--Research and Development--In-Reactor Creep Studies

a. Void Formation and Growth (S. D. Harkness)

Last Reported: ANL-7518, p. 91 (Nov 1968).

(i) Void Size Distributions. A number of size-distribution measurements of voids in fast-neutron-irradiated austenitic stainless steel have been completed. The most obvious generalization is that the size

distributions are quite narrow. The standard deviation of the plots measure only from 0.3 to 0.4 of the mean. Table III.B.1 includes a summary of the size-distribution data and the results of immersion density for comparison. The samples analyzed in this study were obtained from a control-rod thimble and from Mark-IA driver-fuel cladding.

TABLE III.B.1. Void Formation in Type 304 Stainless Steel

Sample	Irradiation Temperature (°C)	Neutron Exposure ($n/cm^2 \times 10^{-22}$)	Average[a] Void Diameter (Å)	Standard Deviation (Å)	Number[b] of Voids per Unit Volume ($\times 10^{-15}$)	Immersion Density Change (%)
Control-rod Thimble	375	2.4	101	38	1.06	0.53
Control-rod Thimble	410	4.5	101	46	2.16	1.26
Control-rod Thimble	450	4.1	118	51	4.08	1.67
Control-rod Thimble	463	3.1	198	70	1.71	1.15
Control-rod Thimble	470	2.4	160	c	2.0	0.39
Cladding	462	1.3	117	32	2.5	c
Cladding	465	1.4	105	c	4.0	c
Cladding	492	1.1	140	c	1.5	c

[a] ±10%.
[b] ±30%.
[c] Not measured.

(ii) Swelling in XG02 Shroud Tubes. In an effort to separate the effects of flux and time, immersion-density measurements were made with an XG02 shroud tube that had been exposed to a relatively low flux (~0.9×10^{15} n/cm^2-sec) for over three years. This long exposure resulted in an integrated neutron flux of 3.2×10^{22} n/cm^2. The measured change in immersion density at the peak flux position was 0.7 ± 0.2%, a value near that expected for this integrated exposure at high fluxes. The large scatter associated with the immersion-density measurements is primarily the result of the tubular geometry of the shroud. The agreement of swelling results for both high- and low-flux irradiations at constant neutron fluence indicates that the reporting of irradiations only in terms of fluence is satisfactory for the purposes of characterizing void formation.

(iii) Void Formation after Irradiation at an Elevated Temperature. A sample of Type 304 stainless steel from an encapsulated structural subassembly has been studied by transmission electron microscopy. This sample reached a temperature of 600 ± 50°C and received a neutron exposure of 2×10^{22} n/cm^2. No voids or Frank dislocation loops were observed. The only observable defect structure consisted of a low number density of prismatic dislocation loops and an occasional polygonized dislocation wall.

The fact that no voids were observed emphasizes the temperature dependence of the phenomenon.

4. Techniques of Fabrication and Testing--Research and Development

a. Nondestructive Testing--Research and Development

(i) Development of Nondestructive Testing Techniques (C. J. Renken)

Last Reported: ANL-7518, pp. 92-96 (Nov 1968).

(a) Filters for Electromagnetic Test Systems. Investigations are continuing to provide improved filtering methods for electromagnetic test systems. Filtering in scanning nondestructive test systems is a problem that could have significant consequences on the cost of future fast reactor components, particularly jacket tubing and heat-exchanger pipe. Proper filtering can reduce the chance of a defect being overlooked by the test system and can drastically reduce the number of false alarms due to unimportant variations in specimen parameters.

A general block diagram of an electromagnetic test system is shown in Fig. III.B.3. The transducer (usually some type of inductor or set of inductors) induces a time-varying current in the specimen and detects the field established by the specimen current. The information developed in the transducer is always delivered to the electronic-processing circuitry by a time-varying current termed "the carrier." This carrier is usually a sinusoid of the same frequency as that driving the transducer, but the carrier may be a train of pulses, as in the case of pulsed electromagnetic test equipment. The carrier is electronically processed to separate useful test information from extraneous signals. After processing, the carrier may be displayed on an oscilloscope for readout, but the carrier is usually demodulated so that its amplitude may either be displayed on an ordinary low-frequency recorder or used to operate various logic devices. Demodulation is the removal of essentially all of the frequency components that are independent of the presence of the specimen.

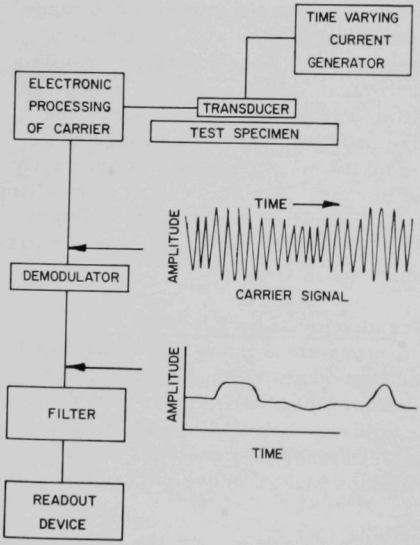

Fig. III.B.3. General Block Diagram of an Electromagnetic Test System

The frequency spectrum of the demodulated output signal is influenced by many variables, including those of the test specimen, the scanning speed, and the design of the transducer. However, all information must be transmitted through the transducer, so its design inevitably influences the whole spectrum. The transducer can be considered as a type of filter.*

One of the ways of determining the transfer function of a filter is to measure its response to an impulsive driving function and then to calculate the Fourier transform of the result. Subject to certain qualifications, the effect that an infinitely small discontinuity within the transducer field exerts on the response of the transducer can probably be calculated. (This problem is being actively pursued.) The effect of such a discontinuity can be experimentally simulated by passing a very small discontinuity through the field, for example, a small hole in a specimen. An example of the response of a transducer to such an experimental "impulse defect" is shown in Fig. III.B.4. To avoid confusion, remember that the responses of this type of transducer appears at the output of the demodulator, and is caused by a change in either the amplitude, phase, or frequency of the carrier. In one sense, Fig. III.B.4 would ideally show a spike, except that such a transducer response would demand infinite scanning time of the specimen; but, the shorter the response of a transducer to an impulse defect, the higher the resolution associated with the transducer. The calculated spectrum of Fig. III.B.4 is shown in Fig. III.B.5. Ideally, this response should be flat to infinity; instead, the transducer is a type of low-pass filter.

In the past, the transfer function (in space) of a transducer has been largely neglected when filters were designed for electromagnetic test systems. Specifically, current commercial

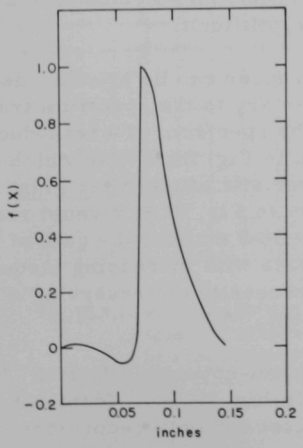

Fig. III.B.4

Spatial Response of a Certain Electromagnetic Transducer to an Experimental Impulse Defect Passing through the Field. The abscissa represents distance along a line through the transducer field starting from an arbitrary zero point, and the ordinate has been normalized to a unit peak value

*Renken, C. J., Mater. Eval. 26(9), 191-195 (Sept 1968).

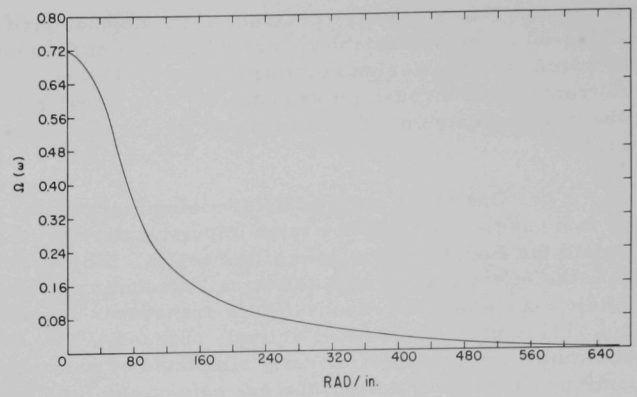

Fig. III.B.5. The Calculated Spectrum of the Spatial Response Function Shown in Fig. III.B.4

electromagnetic test gear systems suffer, with practically no exceptions, from one of the following faults. (1) No filtering exists. This causes the test system to be too sensitive to low-frequency sources of noise, for instance, tube-reducer marks in jacket tubing. (2) A narrow bandpass filter is used to remove practically all of the low-frequency response of the system--that portion of the spectrum below perhaps 160 rad/in. with reference to Fig. III.B.5. This type of filter eliminates a great deal of the noise, but at the risk of low sensitivity to long defects with gradual beginnings and ends, as for example, a long crack in a jacket tube. A narrow bandpass filter also makes the system hypersensitive to very short defects such as small pits, scratches, and inclusions. (3) A differential transducer is used. This creates a zero at zero frequency, and makes the remainder of the transducer spectrum so complicated that interpretation of defect signals becomes very difficult.

The response of a transducer can be broadbanded within limits by designing a filter complementary to the spectrum transfer function of the transducer. An example of the spectrum of a transducer-broadbanding complementary filter is shown in Fig. III.B.6, in which only the amplitude is plotted. The phase characteristic of the filter must also be considered. A filter truly complementary to Fig. III.B.5 would require infinite gain at infinite frequency. As a practical matter, the gain of the complementary filter must eventually decrease with increasing frequency because of stability considerations and the necessity of preserving a reasonable signal-to-noise ratio of the system.

The effect of this less-than-optimum filter of Fig. III.B.6, as a tube is scanned, is shown in Fig. III.B.7. Identical overall system gain at zero frequency was used for both recordings.

The amplitude of the response of the system to the moderately short defect is increased by almost a factor of two with filtering, but more importantly, amplitude is not increased beyond the response that would be produced by a defect with the same depth, but a very long length.

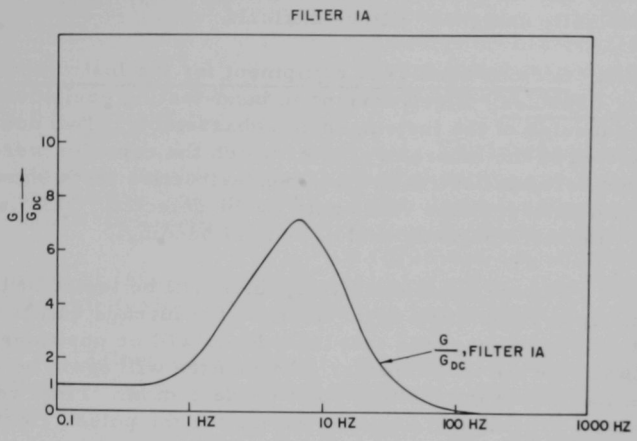

Fig. III.B.6. The Absolute Magnitude of the Spectral Response of a Transducer-broadbanding Complementary Filter. The abscissa shows frequency in hertz, and the ordinate is filter gain normalized to the zero frequency value.

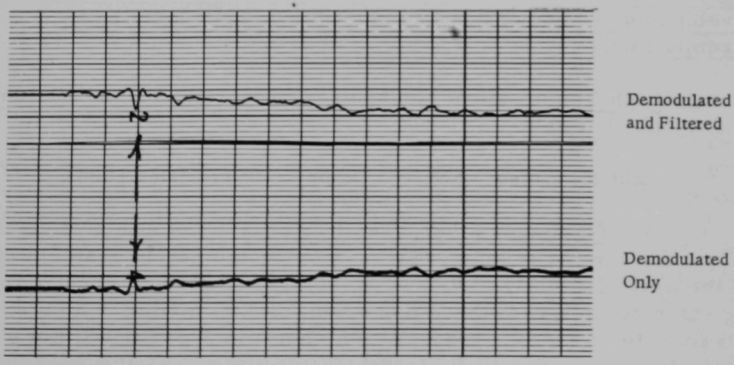

Fig. III.B.7. Recordings Showing the Effect of the Filter of Fig. III.B.6 at a Scanning Speed of 1.27 cm/sec. The signal marked by an arrow was produced by a longitudinal electromachined notch on the inner surface of a Type 304 stainless steel tube. (Relevant dimensions are tube OD: 7.63 mm; wall thickness: 0.382 mm; notch length: 1.7 mm; width: 0.127 mm; depth: 0.038 mm.)

Work is underway on the design of better filters than the one illustrated. This is essentially a problem in network synthesis, but the design is complicated by the fact that the transfer functions of filters are available only as data and not in analytic form. An additional complication is the very low frequencies involved, which make the practical realization of "classically designed" filters difficult.

(ii) Sodium-bond Test Equipment for the Instrumented Subassembly Capsules. Electromagnetic bond-testing equipment is now in use for the capsules of the instrumented subassembly. Two dummy capsules have been tested in the laboratory, after which the capsules were decanned. A comparison between destructive and nondestructive tests showed that non-wet areas with no associated void could not be detected. This is considered normal for an electromagnetic test of sodium bonding.

Future subassembly capsules will be tested at the site of fabrication. Upon completion of fabrication, the furnace will be removed and the pulsed electromagnetic test transducer will be positioned on the furnace to encircle the fuel capsule. The furnace will again be raised to heat the capsule above the melting point of the sodium. Final removal of the furnace will provide the scanning motion for the pulsed electromagnetic transducer.

A standby transducer will be fabricated to insure the continuous readiness of the pulsed electromagnetic equipment.

5. Engineering Properties of Reactor Materials--Research and Development--High Temperature Mechanical Properties of Ceramic Fuels

a. High Temperature Mechanical Properties of Fuel Oxides (R. J. Beals)

Last Reported: ANL-7513, pp. 110-111 (Oct 1968).

(i) Maximum Fiber Tensile Stress. The effect of strain rate upon the maximum fiber tensile stress of stoichiometric uranium dioxide with a theoretical density of 97% is presently being determined (on the Instron testing machine) at a crosshead movement of 0.5 cm/min, which corresponds to a strain rate of 3×10^{-3} cm/sec. As shown in Fig. III.B.8, the maximum fiber tensile stress increased steadily from an average value of 1369.4 kg/cm^2 at 500°C to an average peak value of 1695.2 kg/cm^2 at 1600°C; at least five determinations of maximum stress were used in computing each average.

A comparison of previous data (see ANL-7513, Fig. III.B.9, p. 110) with Fig. III.B.8 shows that both the peak value of maximum fiber stress and the temperature at which the peak occurred have shifted markedly

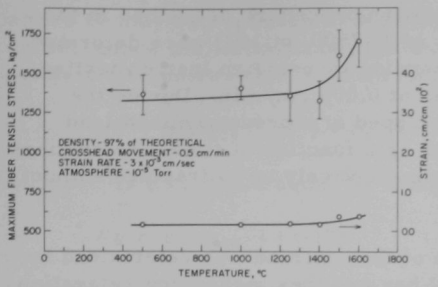

Fig. III.B.8. The Effect of Temperature on the Maximum Fiber Tensile Stress and Strain of Stoichiometric UO_2

as the strain rate was increased by two orders of magnitude. At a strain rate of 3×10^{-5} cm/sec, peak stress occurred at 1400°C and then decreased rapidly. At the present strain rate of 3×10^{-3} cm/sec, the maximum occurs at ~1600°C; the precise temperature will be determined in subsequent tests.

The increase in total strain is slight at the rapid strain rate. Total strain for the specimen tested in four-point cross bending was 0.00176 cm/cm at 500°C and 0.00363 cm/cm at 1600°C. This behavior also differs from that of the slower strain rate (appreciable total strain was evident at 1400°C).

Effort will continue to determine the effect of temperature on the maximum fiber tensile stress and the total strain of stoichiometric uranium dioxide.

(ii) Compressive Creep. Specifications are being assembled for equipment necessary to determine the compressive creep of the mixed oxides of uranium and plutonium at temperatures up to 2500°C in environments of vacuum, inert gas, and reducing gas.

(iii) High-temperature Stress Relaxation of UO_2
(J. T. A. Roberts)

Not reported previously.

A study of the stress relaxation of UO_2 at high temperatures has been initiated to provide data for fuel-element design. In the past, stress-relaxation measurements were used successfully to study some aspects of the plastic deformation of metals at low temperatures.* Because of its simplicity, this technique is adaptable to the study of plastic flow in ceramic fuel materials. The occurrence of any diffusion-assisted recovery conflicts with the basic hypothesis that α_i, the long-range internal stress, is constant during relaxation. If, however, measurements are made over short times before recovery can start, then the same principles used for metals at low temperatures should hold for ceramics at high temperatures. A preliminary study of stoichiometric UO_2 (95% of theoretical density) was undertaken to test the feasibility of this argument. Tests were performed at 1326 and 1511°C.

*Feltham, P., Phys. Status Solidi 3, 1340 (1963); Sargent, G. A., Acta Met. 13, 663 (1965); Feltham, P., and Spears, C. J., Met. Sci. J. 2, 183 (1968).

The specimens (fabrication procedure described in the Progress Report for September 1968, ANL-7500, p. 102) were deformed under conditions of four-point cross bending by using an Instron testing machine operated at a crosshead speed of 0.005 cm/min. During the load-deflection test the machine was stopped at a predetermined load value and the load relaxation measured as a function of time. Relaxations under several loads were performed consecutively up to fracture without intermediate unloading to zero.

The stress relaxation of the machine was determined by replacing the tooling with a rigid steel bar and then measuring relaxation at various loads and strain rates. Since relaxation was only 0.5 kg at an initial load of 100 kg and at crosshead speeds of up to 0.02 cm/min, machine relaxation was therefore neglected.

Typical relaxation curves obtained at 1511°C are plotted in Fig. III.B.9. The same data are plotted in Fig. III.B.10 as the stress relaxation versus a logarithmic function of the time t following the

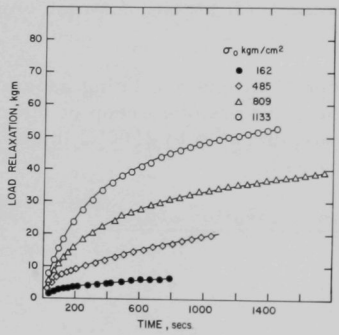

Fig. III.B.9. Relaxation Curves for UO_2 at 1511°C

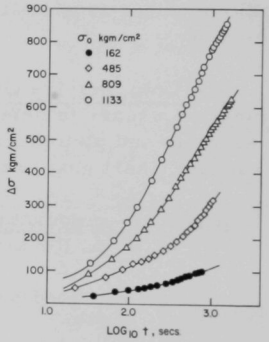

Fig. III.B.10. Logarithmic Representation of Relaxation Curves of Fig. III.B.9

arrest of the Instron crosshead. Initially, the relaxation is nonlogarithmic, but at longer times the relaxation may be described by

$$\sigma_0 - \sigma = \Delta\sigma = s \log_{10} t, \qquad (1)$$

where σ_0 is the stress at start of relaxation, σ is the stress sometime thereafter, and s is the slope of the linear portion of the curve. Clearly, Eq. (1) must be modified to describe the nonlinear relation at short times; thus,

$$\Delta\sigma = s \log_{10} (t + t^*), \qquad (2)$$

where t^* may be regarded as a parameter defining the initial shape of the curve. Since the initial condition that the curve pass through the origin is not satisfied unless $t^* = 1$, a further modification is necessary:

$$\Delta\sigma = s \log_{10} (t+t^*) + c, \tag{3}$$

where c is a constant equal to $-s \log_{10} t^*$. Then by rewriting Eq. (3),

$$\Delta\sigma = s \log_{10} (1+t/t^*). \tag{4}$$

Equation (4) is identical to the equation used to describe stress relaxation in metals at low temperatures.† The slope $s\ (\partial\Delta\sigma/\partial \log_{10} t)$ is the strain rate sensitivity, and t^* is the relaxation time.

Table III.B.2 lists values of s and t^* for the two temperatures, obtained from a least-square regression analysis, applied to the linear part of the curves. Figure III.B.11 shows that there is a linear relation between s and the initial stress σ_0, and that s is higher at the higher temperature. This behavior is in good agreement with that observed for metals. No clear relation was found between t^* and σ_0, but an increase in temperature caused a large reduction in t^*, as shown in Table III.B.2.

TABLE III.B.2. Relaxation Data for UO_2 at Two Temperatures

Initial Stress σ_0 (kg/cm^2)	1326°C		1511°C	
	s (kg/cm^2)	t^* (sec)	s (kg/cm^2)	t^* (sec)
161.8	-	-	81.8	44.8
323.6	-	-	149.6	37.8
485.4	-	-	292.5	88.1
647.2	-	-	329.2	48.2
775	276.6	143.4	-	-
809	-	-	396.2	45
970.8	-	-	469.6	40.5
1132.6	-	-	534.8	35.7
1162.5	417.4	140.5	-	-
1504.2	-	-	700.3	31.44
1550	687.2	156.1	-	-
1937.5	875.95	178.74	-	-

†Feltham, P., Phys. Status Solidi 3, 1340 (1963); Sargent, G. A., Acta Met. 13, 663 (1965); Feltham, P., and Spears, C. J., Met. Sci. J. 2, 183 (1968).

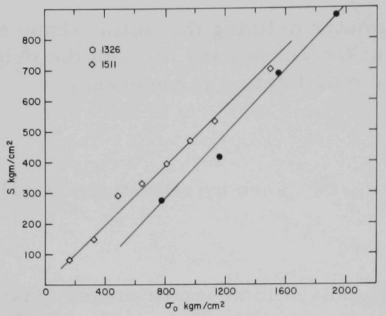

Fig. III.B.11

Strain-rate Sensitivity vs Applied Stress

Stress relaxation is now being measured at other temperatures to determine the range over which this logarithmic relaxation holds. This data should enable one to calculate activation energies and volumes for the yielding and flow processes. In order to determine when recovery begins, and to study the recovery process, relaxation should be measured over a longer period of time.

C. Engineering Development

1. Research and Development

a. Instrumentation and Control

(i) Boiling Detector (T. T. Anderson)

Last Reported: ANL-7500, pp. 104-105 (Sept 1968).

(a) Acoustic Method

(1) High-temperature Detector Development (T. T. Anderson and R. H. Selner)

Bonding the lithium niobate ceramic crystal to Types 304 and 304L stainless steel continues to be a major problem in the fabrication of a high-temperature acoustic sensor. The present ceramic-to-metal bonding method is performed in two steps. In the first step, platinum-palladium-gold paste electrodes are air-fired to the lithium niobate crystal. In the second step, the electroded crystal is vacuum-brazed to a metal surface of Type 304 or 304L stainless steel. The braze material for recent tests has been a high-purity eutectoid alloy of gold and nickel. Ceramic-to-metal bonds made by this method have had shear strengths varying from moderate to poor when compared to tear strength of the electroded film. During the high-temperature brazing, unprotected surfaces of the lithium niobate become opaque; this phenomenon may be due to migration and loss of oxygen at high temperature.*

*Personal communication from G. M. Loiacono, Isomet Corp., Palisades Park, N. J.

A study of alternatives of design and fabrication of high-temperature acoustic sensors has been initiated. A first objective of this study is to reduce the mechanical stresses at the ceramic-to-metal interface. Stresses transmitted from the sensor body to the crystal can be reduced through use of a diaphragm circularly corrugated between the crystal and the body; jigs have been made and from them experimental diaphragms have been produced. Silver-copper braze alloys are being investigated to obtain ductile lower-temperature brazed joints. It is hoped that use of these alloys will reduce oxygen loss from the lithium niobate.

A second objective of the study is to evaluate the effectiveness of high-bond-energy ceramic-to-metal bonding methods, such as (1) plasma spraying, flame spraying, or r.f. sputtering of electrode materials, and (2) one-step active-metal ceramic-to-metal bonding.

(2) Sound Measurements in EBR-II
(T. T. Anderson and B. B. Spillane)

A report* has been presented on radial resonances of cylinders: (1) as the resonances affect the acoustic spectra generated by boiling, and (2) as cylindrical geometries within the EBR-II reactor might affect sound transmission from the core region.

The sound and vibration levels around operating power reactors need to be measured to determine signal-to-noise effects on acoustic boiling detection. For that purpose, a test program has been established to monitor the EBR-II reactor system. Acoustic and vibration monitoring will be performed at the reactor operating-floor level on structural members that extend into the primary tank and thence onto or into the reactor vessel. Test procedures have been formulated, and the necessary equipment has been shipped to the reactor site.

To support the monitoring of the reactor, an out-of-pile test program is measuring the sound level from boiling sodium in a simulated reactor environment. A high-flux heater is being incorporated into a test rig to determine its effectiveness for boiling sodium.

b. Engineering Mechanics

(i) Structural Dynamics Studies--Parallel-flow-induced Vibrations (M. W. Wambsganss, Jr.)

Last Reported: ANL-7518, pp. 101-102 (Nov 1968).

(a) Transducer Development. To answer the need we have identified for a displacement-transducer assembly to measure the displacement

*Anderson, T. T., and Grate, T. A., Acoustic Boiling Detection in Reactor Vessels, presented at the IEEE 15th Nuclear Science Symposium, Montreal, Canada, October 23-25, 1968.

of a tubular test specimen without disturbing the flow field (it also could measure the displacement of an element within a bundle), we have been developing an eddy-current-type proximity transducer. The pickup coil is wound on a plastic capsule fixed to a thin-walled tube. The transducer tube is mounted concentrically inside the tubular test specimen. Ideally, the transducer tube would remain rigid and isolated from the test specimen, so that the transducer would measure the absolute displacement of the test specimen.

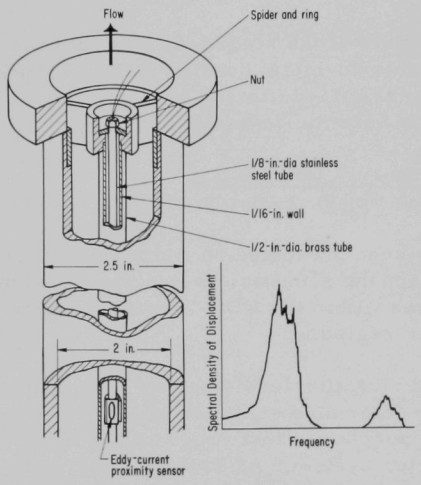

Fig. III.C.1. Displacement-transducer Assembly and Typical Spectral-density Output

Early attempts to construct such a transducer assembly were plagued by the close proximity of the natural frequencies of the transducer tube and test specimen; there was sufficient coupling at the supports to excite a resonant response of the transducer tube that would mask a portion of the test-specimen response. Satisfactory separation of the natural frequencies and reduced coupling were achieved by improving the mounting method, selecting the cross-sectional properties of the tube, and applying axial tension to the transducer tube. Figure III.C.1 shows the transducer and mounting method, as well as a typical spectral-density output. The lower-frequency response is the desired spectral density of the displacement of the tubular test specimen; the higher-frequency response is the unwanted resonant response of the transducer tube, which now is damped and separated sufficiently from the test-specimen response that it safely can be neglected.

The internally mounted transducers were evaluated by comparing their outputs with outputs from corresponding transducers mounted in the wall of the test section. Figure III.C.2 compares displacement-time histories. Correlations within a few percent were achieved for rms displacements over the 5-50-ft/sec range of flow velocities tested.

(b) Flowtest Single Cylinders. Displacement spectral densities for use in evaluating the internally mounted displacement transducers were obtained from flowtests on a single cylinder. RMS displacements were computed from the spectral-density curves and plotted against mean axial flow velocity; these results correlated very well those from an

earlier similar test (see ANL-7518, p. 102, Fig. III.C.1). For the more recent test, the tubular test specimen was soldered to the end supports rather than fixed with epoxy. The corresponding rms displacements in mutually orthogonal directions were approximately the same in this test, although they differed from results of the earlier test by a factor of two. This implies that we are obtaining a more ideally clamped end condition by soldering; theoretically, with clamped-clamped ends, one would expect the response to be the same in both directions.

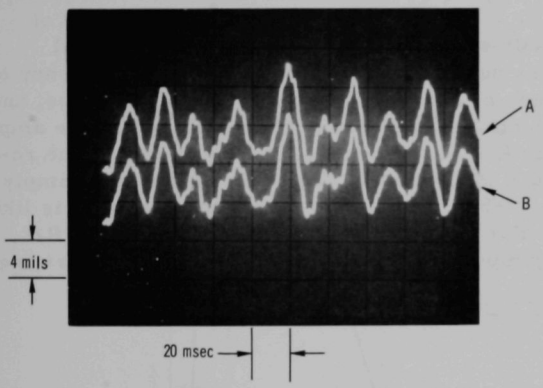

Fig. III.C.2

Displacement-Time Histories of Cylinders during 35-ft/sec Flowtest as Indicated by Eddy-current-type Proximity Transducers Mounted (A) within the Tubular Test Specimen and (B) in Wall of Test Section

(ii) Structural Dynamics Studies--Crossflow-induced Vibrations (M. W. Wambsganss, Jr. and S. S. Chen)

Last Reported: ANL-7518, p. 102 (Nov 1968).

(a) Analysis of Interaction and Tube-spacing Effects

New task; not reported previously.

The vibrations of a tube with motion-constraint stops have been analyzed for the general cases in which the tube can have any end conditions and the stops can be located at any section of the tube and with unsymmetric clearance. The motion is expressed in two states: motion between the stops and motion in contact with the stops. Because the motion is linear within each state, the response of the tube can be found by step-by-step analysis. However, if the local deformation at the contact area is included in the theory, it will be necessary to solve a nonlinear integral equation, which increases the complexity of the theoretical solution.

As a first approximation, the local deformation is neglected. By the conventional normal-mode approach, the free-vibration problem does not exhibit any special difficulty. Unfortunately, it is still very tedious to find the steady response of forced vibration. To understand the nonlinear behavior of the system, a one-mode approximation is employed

for the forced-vibration study. Under such an assumption, the problem is reduced to a bilinear system with a piecewise linear forcing function. Then the steady-state response is obtained by the method of van der Pol and Krylov-Bogoliubov.*

As an example, the steady-state response due to a uniformly distributed load, $F \cos \omega t$, of a simply supported tube with symmetric stops at midspan is shown in Fig. III.C.3, where $\Omega = (m/EI)^{1/2}\omega\ell^2$, $R = F\ell^3/EI$, $\epsilon = \delta/2\ell$, $\Omega_1 = \pi^2$ = nondimensional frequency of a simply supported tube, $\bar{\Omega}_1 = 6.25\pi^2$ = nondimensional frequency of a two-span continuous tube with simply supported ends, EI = flexural rigidity of the tube, m = mass per unit length of the tube, ω = frequency of the forcing function, ℓ = length of the tube, δ = clearance of the stops, and ζ = damping ratio. The deflection of the tube is characterized by the amplitude q/ϵ. When the amplitude R/ϵ of the forcing function is small, the response is in the range $-1 \leq q/\epsilon \leq 1$, which is the same as that of a simply supported tube without stops. When R/ϵ is very large, the response is like a two-span continuous tube. For an intermediate value of amplitude R/ϵ, the response possesses the jump phenomenon that occurs when the driving

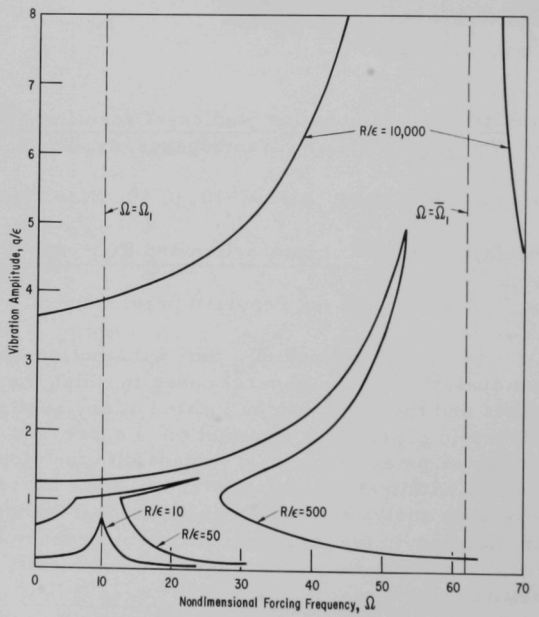

Fig. III.C.3. Amplitude Response Curves of a Simple Supported Tube for a Damping Ratio of 0.1

*Bogoliubov, N. N., and Mitropolsky, Y. A., Asymptotic Methods in the Theory of Non-linear Oscillations, Gordon and Breach Science Publishers, N. Y., N. Y. (1961).

frequency is in the range $\Omega_1 \leq \Omega \leq \bar{\Omega}_1$. This is illustrated in Fig. III.C.4 where the amplitude follows the curve ABC, then jumps down to E, and then on to F as the forcing frequency is increased. Conversely, when the forcing frequency is decreased slowly, the jump occurs at D.

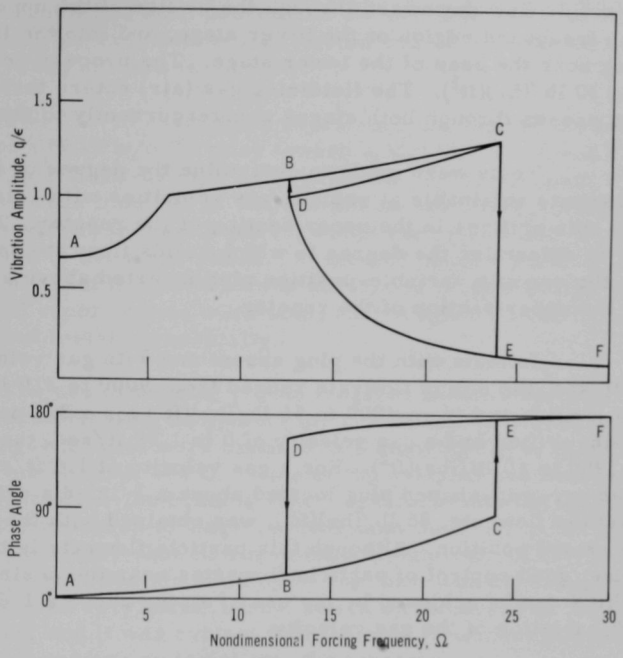

Fig. III.C.4. Phase Response Curve of a Simply Supported Tube for $R/\varepsilon = 50$ and a Damping Ratio of 0.1

Because the stresses and the impact are related to the second and third derivatives of the displacement, more modes must be included. Work has gotten underway to find the stresses and impact by refined analysis and to investigate the effect of local deformation.

D. Chemistry and Chemical Separations

1. Aqueous and Volatility Processes--Research and Development--Fluoride Volatility Process

a. Engineering-scale Development for FBR Fuels (N. M. Levitz)

Last Reported: ANL-7518, pp. 106-107 (Nov 1968).

(i) Continuous-feed, Two-stage Fluid-bed Reactor. Slab-shaped fluid-bed reactors of 4-in. thickness are being considered for the continuous fluorination of powdered fast reactor fuel material. Studies are

currently being conducted in a mocked-up 4-in.-square section of a two-stage reactor. The bottom of each 36-in.-high stage has the shape of an inverted pyramid, 7-in. deep, with an orifice at the apex. The particulate solids (48-100 mesh alumina) are fed into the fluidized bed in the upper stage; the solids flow downward through the orifice of the upper stage, through the freeboard region of the lower stage, and into the lower fluidized bed, exiting near the base of the lower stage. The process design particle flowrate is 30 lb/(hr)(ft^2). The fluidizing gas (air) enters through the lower orifice and passes through both stages countercurrently to the solids.

Tests were made to determine the degree of control of particle flowrate obtainable at various gas velocities with 1-in.-, 3/4-in.-, and 1/2-in.-dia orifices in the upper section of the reactor. Tests were also made to determine the degree to which solids flowrate could be controlled by the use of a variable-position plug inserted above a 1-in.-dia orifice of the upper section of the reactor.

In tests with the plug absent and with gas velocities of 0 to 1.45 ft/sec, the solids flowrate ranged from 9000 to 310 lb/(hr)(ft^2) for a 1-in. orifice and from 4000 to 56 lb/(hr)(ft^2) for a 3/4-in. orifice; for a 1/2-in. orifice and a gas velocity of 0 to 1.05 ft/sec, the solids flowrate was 3900 to 10 lb/(hr)(ft^2). For a gas velocity of 1.4 ft/sec and using a truncated pyramid-shaped plug located above a 1-in.-dia orifice, the lowest particle flowrate, 85 lb/(hr)(ft^2), was obtained with the plug 1/4 in. above the seated position. Although this particle flowrate is too high for process use, good control of particle flowrates near the desired rate of 30 lb/(hr)(ft^2) can be achieved by the use of a plug above a 1/2-in. orifice along with variation of the gas velocity.

b. Engineering Design, Analysis and Evaluation (N. M. Levitz)

Last Reported: ANL-7518, pp. 107-110 (Nov 1968).

Conceptual design studies of a large fluoride volatility plant for processing FBR fuels are in progress. A report on the conceptual process is in preparation. It includes a process flowsheet, an engineering flowsheet, a conceptual plant design and equipment layout, and a discussion of those areas that need further work.

2. Closed Cycle Processes--Research and Development--Compact Pyrochemical Processes

a. Process Engineering Studies (R. D. Pierce)

Last Reported: ANL-7518, p. 111 (Nov 1968).

Various materials are being tested to evaluate their suitability for use in pyrochemical-processing equipment. A graphite crucible coated

with vapor-deposited tungsten (see Progress Report for June 1968, ANL-7460, p. 115) was charged with zinc and a $CaCl_2$-20 m/o CaF_2 salt mixture, and heated for 48 hr at 800°C. The molten zinc-salt system was contained successfully, and no cracks were visible in the crucible wall after the melt had been poured and the crucible had cooled to room temperature. This crucible will be tested next with a Mg-44 a/o Cu alloy and a $CaCl_2$-CaF_2 salt phase.

Two 100-hr tests were performed to evaluate the corrosion resistance of a Nb-1 w/o Zr alloy toward a Mg-43.7 a/o Cu-0.17 a/o U/$MgCl_2$-30 m/o NaCl-20 m/o KCl system at 700°C. Coupons of the niobium alloy were mounted at various positions on an agitator shaft so that a coupon was in the metal phase, at the metal-salt interface, in the salt phase, and in the vapor phase. At the end of the test, a slight increase in hardness of all of the coupons was noted, and those that had been exposed to the salt and vapor phases were somewhat roughened. The coupons are being examined metallographically.

The use of brazing to join tungsten sheet is being investigated as a means of fabricating equipment for pyrochemical processes. Samples of brazed tungsten sheet were exposed to a zinc/$MgCl_2$-30 m/o NaCl-20 m/o KCl system for 48 hr at 800°C. Some of the samples had been heat treated after brazing to allow the brazing alloy* to diffuse into the tungsten. Neither type of sample appeared to have reacted with the zinc. After the specimens had been cleaned, they showed a maximum weight gain of 0.77%. Preliminary metallographic examination of samples that had been cut from the test specimens showed very little, if any, attack on the braze at the exposed edge of the tungsten, and it was evident that the heat treatment had been effective in diffusing the brazing material into the tungsten.

b. Experimental Flowsheet Investigations (R. D. Pierce)

Last Reported: ANL-7518, pp. 111-112 (Nov 1968).

Work is continuing on the design and construction of the Plutonium Salt Transport Facility (see Progress Report for September 1968, ANL-7500, p. 115). Piping of the helium-purification systems for boxes 2 and 3 is nearly complete, and helium leaktesting is underway. The ductwork for the refrigeration system in box 3 has been fabricated and is being installed. Work has been started on the ventilation system in box 3. An enclosure is being constructed to house vacuum pumps and other auxiliary equipment associated with box 3. The top flanges for the three main processing vessels in box 3 are being fabricated. These flanges contain agitator bearings, sample ports, and transfer line and thermocouple feed-throughs. The flanges are scheduled for completion by the end of December.

*Coast Metals #60, Coast Metals Co., Little Ferry, New Jersey; nominal composition: 22.7 a/o Si, 18.3 a/o Cr, 3.65 a/o Fe, balance Ni.

Drafting work was completed on the process piping system for box 3; procurement of valves for this system is nearly complete. Heating coils to provide a constant heat load for the refrigeration systems in boxes 2 and 3 have been designed and are being fabricated. Drafting work is underway on the process-pressure control system for box 3.

The water tanks, transfer pump, and two water chillers for the negative-pressure water-cooling system for box 2 have been received, and a table for a cutoff wheel to be located in box 10 has been completed.

c. Liquid Metal-Molten Salt Contactors (R. D. Pierce)

Last Reported: ANL-7518, pp. 112-113 (Nov 1968).

Testing of the solid-rotor agitator pump (see ANL-7518) with a Mg-42 a/o Cu alloy has been completed. The pump assembly was held at 670°C, and the pump was operated for a total of 55 hr at various speeds and submergence levels. The output of the pump was measured at submergences ranging from 0.96 to 2.35 in. and at speeds from 850 to 1050 rpm. The data obtained in these tests are in good agreement with data obtained previously with a water-acetylene tetrabromide mixture. This agreement indicated that these high-temperature pumps and their associated components can be calibrated at low temperatures with aqueous-organic systems.

d. Decladding and Fuel Resynthesis (R. D. Pierce)

Last Reported: ANL-7500, pp. 117-118 (Sept 1968).

The objective of the fuel-resynthesis studies is to investigate possible methods for resynthesizing oxide fuel from the metallic plutonium and uranium products of a pyrochemical process. The reaction of uranium metal with CO_2 has been reported to form UO_2 as the principal product with a carbon content of 0.1 w/o.* Although the rate of reaction of CO_2 with uranium metal is relatively low, the rate can be increased by hydriding the metal to form a finely divided powder.

Preliminary studies of the uranium-CO_2 reaction were conducted in a $1\frac{1}{2}$-in.-dia fluidized bed. The feed material was hydrided uranium in the form of a fine powder. A H_2-CO_2 mixture was used as the fluidizing gas, and the effluent gas was analyzed for CO_2, CO, and CH_4 by means of a process-gas chromatograph. Seven experiments were performed at several different temperatures ranging from 400 to 740°C. The superficial velocity of the fluidizing gas (H_2-9 or 18 v/o CO_2 at 2 atm pressure) was 15 cm/sec.

These preliminary results indicate that the CO_2-H_2 reaction can be used in a fluidized bed to resynthesize oxide fuels from the metallic

*Stobbs, J. J., J. Electrochem. Soc. 112, 916 (1965).

products of a pyrochemical process. However, further investigations are needed to select process conditions that will minimize carbon contamination of the product, which ranged from 0.3 to 1.5 w/o in these experiments.

3. General Chemistry and Chemical Engineering--Research and Development

a. Studies on the Formation and Stabilization of Carbon-bearing Dispersions in Sodium (F. A. Cafasso)

Last Reported: ANL-7500, p. 118 (Sept 1968).

Attempts are being made to prepare stable, well-characterized dispersions of carbon-bearing materials in sodium. These dispersions will be used to determine whether particulates play a role in the transport of carbon through sodium, e.g., in the carburization of austenitic steels.

It was reported previously (see ANL-7500) that, under an ultrasonic field, dispersion of up to 1 w/o Carbolac 1* (a 90-Å carbon black) in eutectic NaK (a liquid at room temperature) was possible. The dispersions, however, have been shown to be unstable upon dilution. Effort is now being concentrated on producing stable dispersions in liquid sodium at temperatures above 400°C. A controlled-atmosphere furnace with capability for ultrasonic treatment and sampling of liquids at temperature** has been assembled. In a preliminary experiment with this device, a small quantity of Carbolac 1 was slowly heated in sodium to 800°C under ultrasonic irradiation. Analyses of various samples of the liquid showed that dispersion was not achieved. Alternative methods of introducing carbon into sodium are being investigated, in particular, by surface graphitization of ferritic steel and the cracking of organic material such as tetralin.

b. Determination of the Solubility of Helium in Sodium (F. A. Cafasso)

Last Reported: ANL-7500, p. 118 (Sept 1968).

Since helium is a potential cover gas for sodium in fast breeder reactors, its solubility in sodium is being measured. Information on the temperature and pressure dependence of the solubility is needed to determine whether or not problems of gas transfer and cavitation may accompany its use.

---

*Cabot Corp., Boston, Mass.

**Bromberg, M. L., Thomas, J. G., and Tarpley, W., Ultrasonically Produced Dispersions of Thorium Bismuthide in Molten Bismuth, NYO 7924 (March 1958); Bromberg, M. L., and Tarpley, W. B., Feasibility Study on Ultrasonic Dispersion of Uranium Dioxide in Molten Metals, NYO 7929 (May 1958).

An existing solubility apparatus has been modified for this purpose. The solubility will be measured by saturating reactor-grade sodium at a preselected temperature with helium, stripping the dissolved helium from the sodium with argon, separating the argon from the helium by trapping the former on liquid-nitrogen-cooled molecular sieves, collecting the helium, and analyzing it mass spectrometrically. The solubility of helium is expected to be so low that the helium concentration in the argon sparge gas is anticipated to be only 1 ppm. To gain analytical sensitivity, the helium used for saturating the sodium has been enriched in the uncommon isotpe ^{3}He. The recoverability of known amounts of ^{3}He introduced into the stripping section is currently being tested, and if the procedure proves reliable, the solubility measurements will follow.

c. Preparation of Nuclear Materials (P. A. Nelson)

Last Reported: ANL-7500, pp. 119-120 (Sept 1968).

A 25-kW, inductively heated plasma torch has been installed for studying a continuous process for producing UC from uranium oxides. A schematic diagram of the installed equipment is shown in Fig. III.D.1. Small, agglomerated particles (~100 mesh) of UO_2 and carbon will be heated above the melting point of the UC product by passing the particles concurrently through the plasma-flame (argon or helium, possibly with a small amount of hydrogen or nitrogen). The reaction should take place very rapidly, and it is expected that the product will be spherically shaped particles. The product particles will have solidified prior to striking the walls or bottom of the water-cooled reaction chamber. The CO produced by the reaction will be removed from the reaction chamber along with the inert plasma-forming gas. This plasma-torch process should be capable of continuous production of UC in the facility being constructed, and the process is expected to be applicable to the continuous production of (U,Pu)C if the equipment is installed in an alpha-tight enclosure.

A safety review of the facility has been completed, and the manufacturer has provided startup assistance for the plasma-torch equipment. Shakedown tests are now in progress. In the initial experimental runs, attempts will be made to form spherical particles from Al_2O_3 powder which will be used as a stand-in for the uranium oxide-carbon particles.

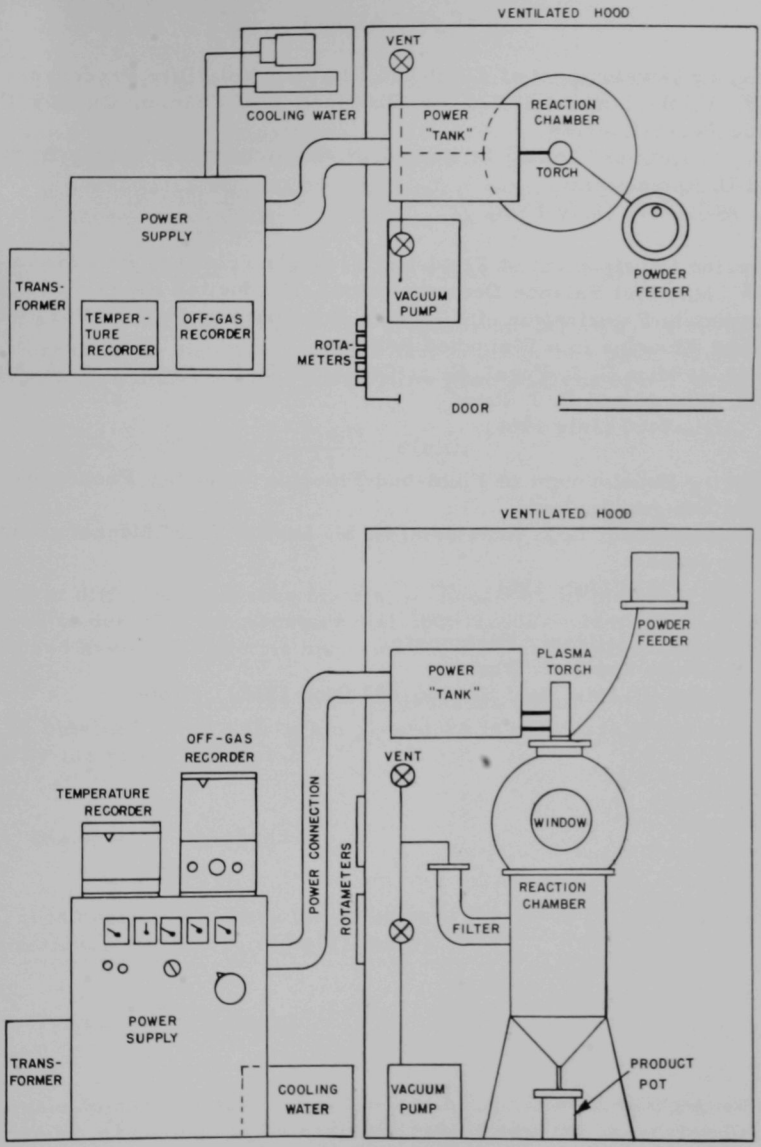

Fig. III.D.1. Plasma-torch Installation for Studying the Conversion of Uranium Oxide to Uranium Carbide

PUBLICATIONS

Engineering Development of Fluid-bed Fluoride Volatility Processes. Part 13. Pilot-plant Studies of the Fluorination of Uranium Oxide with Bromide Penetafluoride

John T. Holmes, Lowell B. Koppel, N. Saratchandran, James B. Strand, and D. Ramaswami

ANL-7370 (May 1968)

Engineering Development of Fluid-bed Fluoride Volatility Processes. Part 15. Material Balance Demonstrations, Production Rates, and Fluorine Utilizations in Fluorination of Kilogram Quantities of PuF_4 to PuF_6 with Elemental Fluorine in a Fluid-bed Reactor

N. M. Levitz, G. J. Vogel, E. L. Carls, D. E. Grosvenor, W. A. Murphy, B. J. Kullen, and D. J. Raue

ANL-7468 (July 1968)

Engineering Development of Fluid-bed Fluoride Volatility Processes. Part 11. Off-gas Analysis

D. Ramaswami, L. J. Anastasia, N. M. Levitz, W. J. Mecham, and A. A. Jonke

ANL-7339 (July 1968)

Dry Pressing of a Urania Pycnometer

D. E. White and R. J. Beals

J. Am. Ceram. Soc. 51, 666-667 (Nov 1968) Note

IV. NUCLEAR SAFETY

A. Reactor Kinetics--Other Reactor Kinetics--Research and Development

1. Reactor Control and Stability

a. Transfer Function Techniques to Measure Large Fast Reactor Stability (L. Habegger)

Last Reported: ANL-7518, p. 119 (Nov 1968).

(i) Spatial Effect. The methodology for analysis of space-dependent transfer functions in large fast reactors has been extended to systems whose mathematical description has equations of the form

$$\frac{\partial T(z,t)}{\partial t} = aT(z,t) + b\frac{\partial T(z,t)}{\partial z} + \phi(z,t);$$

$$T(o,t) = \frac{\partial T(o,t)}{\partial z} = 0, \qquad (1)$$

coupled to diffusion equations for $\phi(z,t)$. Equations of the form of Eq. (1) are used to describe temperature distributions of coolants flowing along the z-axis and having volumetric heat sources with distribution $\phi(z,t)$.

The transfer function from the diffusion equation for $\phi(z,t)$ is to be obtained using a Galerkin procedure in which $\phi(z,s)$* is approximated by the modal expansion

$$\phi(z,s) \simeq \sum_{k=1}^{N} a_k(s)\psi_k(z). \qquad (2)$$

Thus, it is desirable to have the solution of Eq. (1) in terms of a mode-to-mode transfer function $\tau_i(s)/a_k(s)$, where

$$T(z,s) = \sum_{i=1}^{N} \tau_i(s)\psi_i(z). \qquad (3)$$

This mode-to-mode transfer function can be obtained by two procedures: (a) solve Eq. (1) using the Galerkin procedure with the expansion Eq. (3), or (b) solve Eq. (1) analytically and expand the result into the form of Eq. (3).

*A function with argument s represents the Laplace transform of that function.

These two procedures were compared by using values of a, b, and H typical of a large LMFBR design. It was assumed that

$$\psi_i(z) = (2/H)^{1/2} \sin (i\pi z/H),$$

where H is the extrapolated core height.

Method (a) for computing the mode-to-mode transfer function is more convenient computationally because it allows computation of the transfer function of the diffusion equation and Eq. (1) simultaneously by using the Galerkin procedure. However, the results from this method, when compared to analytical results, suffer from loss of accuracy at high frequencies and in spatial regions close to the boundaries.

The transfer function from method (b) is

$$\frac{\tau_i(s)}{a_k(s)} = \frac{-1}{\left(\frac{s-a}{b}\right)^2 + \left(\frac{k\pi}{H}\right)^2} \left\{ \left(\frac{s-a}{b}\right)\delta_{ik} + \frac{4}{H} \begin{bmatrix} 0, & i+k \text{ even} \\ \frac{ik}{i^2-k^2}, & i+k \text{ odd} \end{bmatrix} \frac{2ik\pi^2}{H^3} \frac{\left[-(-1)^i \exp\left(\frac{s-a}{b}H\right) + 1\right]}{\left(\frac{s-a}{b}\right)^2 + \left(\frac{i\pi}{H}\right)^2} \right\}.$$

Coupling this form of transfer function to the diffusion equation is computationally difficult because of the exponential term and, to a lesser degree, because of the fourth-order denominator. However, it was determined that dropping the exponential term has negligible effect. Furthermore, if the entire term within the second set of square brackets is dropped, the accuracy will still compare favorably with that of method (a) and the computational difficulty will be at an acceptable level. Thus method (b) is more desirable than straightforward application of the Galerkin procedure as in method (a).

2. Coolant Dynamics

a. Coolant Dynamics (R. M. Singer and R. E. Holtz)

Last Reported: ANL-7518, pp. 120-121 (Nov 1968).

(i) Sodium Superheat Experiments. The incipient boiling tests conducted out-of-pile have indicated that an increase in the oxide content of the sodium slightly decreases the superheat. All the pool boiling data are being reviewed, and a topical report is being prepared to summarize that work.

The theoretical study of the effects of inert gas on incipient pool boiling has revealed several interesting features of the phenomena. One of the results is the ability to predict either an increase or decrease of the incipient boiling superheat as the heat flux is increased, depending

on the exact sequence of events between experimental runs. Apparently, much of the past confusion in incipient boiling studies can be ascribed to phenomena caused by inert-gas diffusion.

(ii) Coolant-expulsion Experiments. The sodium-expulsion apparatus has been filled with sodium. The electron-bombardment gun has been installed, and the installed instrumentation has been calibrated. Preliminary expulsion tests have been conducted with no inert gas in the system and before establishing any meaningful pressure-temperature history. As expected, the sodium nucleated at essentially zero superheat, and stable steady boiling was achieved with no net expulsion.

(iii) Transient Experiments. Assembly of the system has begun. Analytical studies of incipient boiling superheats in forced-convection systems is continuing. Attempts are being made to characterize a system sufficiently so that the incipient boiling conditions can be predicted for any postulated accident (in which boiling occurs prior to fuel melting). It now appears that the type of accident (such as loss of flow, flow coastdown, or gradual power increase) can significantly affect the incipient boiling conditions.

b. Convective Instability (R. M. Singer)

Last Reported: ANL-7518, p. 121 (Nov 1968).

(i) Flow-coastdown. The heat exchanger for the NaK loop is being redesigned. Control and instrumentation equipment is being selected.

3. Fuel Meltdown Studies with TREAT (C. E. Dickerman)

a. Development of Experimental Methods

Last Reported: ANL-7518, pp. 122-123 (Nov 1968).

Reactor physics calculations have been reported by Iskenderian* for an idealized model of a fast-neutron converter section for TREAT. By use of the Iskenderian model, it was calculated that small clusters of fast reactor fully enriched oxide fuel pins could be given an energy input equal to about three times the energy required to melt the fuel adiabatically, with tolerable cluster flux depressions (maximum to minimum radial power ratio of about 1.1).

The current object of this project is to transform the physics model of the neutron converter presented by Iskenderian into a hardware design which can be inserted into the TREAT reactor.

*Iskenderian, H. P., Study on Conversion of TREAT Facility for Testing of Fast Reactor Subassemblies, Trans. Am. Nucl. Soc. 11, 643 (1968).

The model proposed by Iskenderian is an idealized cylindrical geometry. It consists of an "inner converter" which surrounds the test section and is composed of two regions of UO_2 (or similar ceramic fuel enriched in ^{235}U) and an "outer converter" which surrounds the "inner converter" and couples it neutronically to the lightly loaded TREAT core. The "outer converter" is composed of two regions of graphite-UO_2 fuel similar to the present TREAT fuel but with higher concentrations of ^{235}U than in the core. The two regions of the inner converter are each 5 cm thick; those of the outer converter are each 2.5 cm thick. The actual TREAT core arrangement which this model approximates is as follows:

It is composed of a 10- by 20-cm experimental space surrounded by two, 5-cm-thick rings of ceramic fuel corresponding to the two regions of the inner converter of the model. Surrounding these are two rings, each 2.5 cm thick, composed of regular TREAT graphite fuel with increased ^{235}U content in two steps. Layers of tungsten, each approximately 0.1 cm thick, have been provided on the inside of the inner converter, between the regions of the inner converter, between the inner and outer converters, and on the outside of the outer converter. Thin borated liners are located at the inside and the outside of the outer converter to reduce neutron-flux peaking at interfaces.

The engineering interpretation of this model will have to provide for posttransient cooling, protection of structural strength against overheating the core, and subdivision to facilitate insertion and removal from the reactor.

For ease of handling the most convenient form for the converter would be 10- by 10-cm elements similar to the present square elements. Provisions for handling experimental sections that are 10 by 20 cm exist at TREAT, and converter sections up to this size might be utilized if required.

Two alternative systems* for insulating the converter fuel from the core are being considered. One system would be to construct the converter region of 10- by 10-cm elements, each of which would contain a central fuel region surrounded by insulation on all four sides sufficient to prevent overheating of the cladding material. This system has the advantage of ease of handling, but causes dilution of the converter by the insulation material.

A second system would utilize fuel elements which contain minimal insulation and fuel material clad with a material which would resist oxidation at relatively high temperatures. These elements would be separated from the test section on the inside and from the Zircaloy-clad TREAT

*Gavin, A. P., to be published.

fuel on the outside by separate insulator sections. This arrangement would require deviation from the regular fuel-element shape and size, but would decrease dilution of the converter by eliminating the need for insulation between the elements of the converter section.

Since the former arrangement seems the most flexible and convenient, we are proceeding with heat-transfer calculations and preliminary design configurations to establish the feasibility of this approach. We are striving for a combination of materials and spacing that will provide sufficient internal insulation to allow cooling with the present TREAT air system and still prevent overheating of the cladding or of the exhaust air.

Present indications are that an element clad with a 0.15-cm-thick metal can that is separated from a second, inner can by a gas space filled with low-pressure (approximately 1/4 atm) argon and thermal radiation shielding will possess the required insulation. This will leave a cross section approximately 8.9 cm square for fuel.

The best present guess as to a configuration which might be feasible for the overall design is as follows:

A ring of ten 10- by 10-cm elements insulated as described would compose the inner converter. Each fuel-section element would contain the two sections of different enrichments of ceramic fuel that form the inner converter. The outer converter would be composed of a ring of 14 elements insulated similarly to those described above but with TREAT-like graphite fuel having $^{235}UO_2$ contents corresponding to those required by the physics calculations. Since this arrangement would allow much more fuel material in the outer converter than the model, it is possible that it may not be necessary to divide the outer converter into two separate regions of different $^{235}UO_2$ content.

When this rough design has been checked from an engineering point of view, it will be reduced to a second physics model which will more closely approximate a working design. It is planned to supplement the final physics calculations with mockup experiments in TREAT.

One difficulty which must be considered is posttransient cooling of the converter in the event of loss of power to the TREAT blowers. The present core requires no cooling in this event because the cladding will not reach a high enough temperature to cause excessive corrosion. We propose to use Inconel cladding on the converter elements. This material will probably resist oxidation at the temperatures which will be reached in the event of failure of the cooling air. It will be necessary to check adequacy of natural-convection cooling and of heat loss by conduction into the reflector sections of the converter fuel. The axial reflector sections of the converter elements will probably be clad with the same material as the fuel portion of these elements.

Based on discussions with Metallurgy Division ceramicists, it is expected that the ceramic fuel sections of the inner converter would probably be manufactured as thin (0.6 to 1.5 cm) plates that would be stacked either flat or on edge to fill the fuel portion of the assemblies. The manufacture of these plates will require some development effort.

4. Materials Behavior and Energy Transfer

a. High Temperature Physical Properties (M. G. Chasanov)

Last Reported: ANL-7500, p. 129 (Sept 1968).

(i) Heat Capacity of Liquid UO_2. Measurements of the heat content of UO_2 sealed in tungsten capsules are continuing. Data obtained below the melting point of UO_2 were reported in the Progress Report for June 1968, ANL-7460, pp. 121-122. Data above the melting point (to 3329°K) have now been obtained; these are shown in Fig. IV.A.1 along with the data for solid UO_2. These results extend the range of UO_2 enthalpy data by about 70°K and are generally in excellent agreement with values previously reported.* Of particular interest is the value of approximately 18 kcal/mol found for the heat of fusion of UO_2, which is in good agreement with the value 18.2 kcal/mol reported by Hein and coworkers. However, this result is significantly lower than the value of 25.3 kcal/mole obtained by Grossman and Kaznoff,** who used cooling-curve techniques. No explanation can be offered at present for this difference.

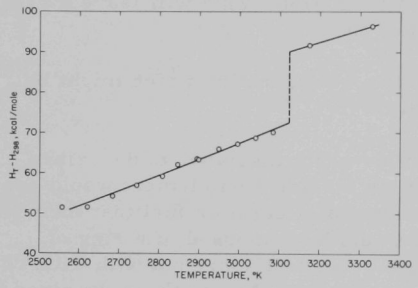

Fig. IV.A.1. Enthalpy of UO_2

Additional experiments are currently being carried out to extend further the temperature range of measured UO_2 enthalpies.

5. Fast Reactor Safety Test Facility Study (C. N. Kelber)

Last Reported: ANL-7518, p. 125 (Nov 1968).

The preliminary report due in March 1970 is in rough draft stage. About 30% of the first draft has been received, and the remainder is on schedule.

---

*Hein, R. A., and Flagella, P. N., Enthalpy Measurements of UO_2 and Tungsten to 3260°K, GEMP-578 (1968); Hein, R. A., Flagella, P. N., and Conway, J. B., J. Amer. Ceram. Soc. 51, 291 (1968).

**Grossman, L. N., and Kaznoff, A. I., J. Amer. Ceram. Soc. 51, 59 (1968).

B. TREAT Operations

1. Reactor Operations (J. F. Boland)

Last Reported: ANL-7518, p. 126 (Nov 1968).

A series of nine temperature-limited transients were run with a dummy experimental capsule in the reactor to obtain additional data on the operating characteristics of the reactor with fuel temperatures above 400°C (see Progress Report for August 1968, ANL-7487, p. 109). Seven transients were run with a core without a viewing slot, and a maximum fuel temperature of 575°C was recorded following the final transient. This temperature was judged to be close enough to the 600°C operating limit that further tests with the unslotted core configuration were unnecessary at this time. Two transients were run with a slotted core configuration, and a maximum fuel temperature of 540°C was recorded following the second transient. Additional transients will be conducted with the slotted core configuration.

Neutron radiographs were made of two groups of EBR-II driver fuel elements. Several neutron radiographs were also made of unirradiated EBR-II driver fuel elements as part of a program to determine the precision of pin-diameter measurements made from neutron radiographs.

2. Development of Automatic Power Level Control System (J. F. Boland)

Last Reported: ANL-7518, p. 126 (Nov 1968).

Following negotiations with the only vendor that submitted a positive response to the bid request for the hydraulic control-rod-drive system, revised specifications were issued and a purchase order for the system was being processed at the end of this reporting period. Delivery is scheduled 180 days after the order is placed.

System installation, originally scheduled for the fourth quarter of FY 1969, will be delayed until the first quarter of FY 1970 by the longer-than-anticipated bidding period.

C. Chemical Reaction--Research and Development--Chemical and Associated Energy Problems (Thermal)

1. Analysis of Loss-of-coolant Accidents (J. C. Hesson)

Last Reported: ANL-7500, pp. 131-133 (Sept 1968).

a. Simulation Experiments to Define Effect of Metal-Water Reaction on Fuel Failure during Emergency Core Cooling. To determine the effect of the environment on the integrity of Zircaloy-2-clad UO_2-core fuel rods following a loss-of-coolant accident in a water-cooled power reactor, 18 steam-oxidation runs were made to assess the extent of cladding failure as a function of cladding oxidation, heating rate, steam flow, and quench temperature. The results were summarized previously (see ANL-7500). For comparison, the effect of hydriding of the cladding by hydrogen produced by the reaction of the cladding with the steam was briefly investigated in four hydriding runs. The results have been interpreted principally on the basis of the relative cladding damage due to hydriding as compared to oxidation.

The hydriding runs were conducted in the same apparatus as the oxidation runs. In these runs, a 3-in.-long induction coil was used to heat a section of the rod; there were about 16.67 g or 0.182 g-mole of zirconium in the 3-in. length of cladding, which had a 31-mil-thick wall and a 0.567-in.-OD cladding density was 6.5 g/cm^3; ZrO_2 density was 5.7 g/cm^3. The cladding temperature was measured at the midpoint of the 3-in.-long coil.

Table IV.C.1 shows the results of these limited hydriding tests. In Run H1 at 1650°C, the lower solubility of hydrogen at high temperatures* accounts for the lesser hydriding and damage to the cladding at the center of the heated zone of the rod. On the other hand, as shown by Run H2 at

TABLE IV.C.1. Hydriding Tests of Single Inductively Heated Zircaloy-2-clad Simulated Fuel Rods

Run No.	Rod Temp (°C)	Duration at Temp (min)	Atmosphere	Cladding: Hydrogen Absorbed (moles)	Cladding: Hydrogen Concentration (av a/o)	Cladding: Oxidation (%) Max	Cladding: Oxidation (%) Av	Results
H1	1650	9	H_2	0.049	34	-	-	Failed[a]
H2	1400	6	Flowing 50% H_2-50% Steam	-	-	9.7	6.1	Intact
H3	1400	6	H_2	0.016	15	-	-	Intact
H4	1400	6	H_2	0.0018	2	~2	~1.5	Intact

[a]Near ends of heated zone because of hydriding.

*Hansen, M. [in Constitution of Binary Alloys, 2nd Ed., McGraw-Hill (1958), p. 809] reports the solubility of hydrogen in zirconium as 62 a/o at 850°C, 50 at 900°C, 46 at 950°C, and 44 (extrapolated) at 1000°C.

1400°C, the greater solubility of hydrogen at lower temperatures is offset by the lower solution rate (kinetics). Thus, for relatively short times (~6 to 9 min) at the conditions of these tests, greatest damage by hydriding apparently occurs between 1400 and 1650°C. From comparison of these hydriding tests with the previous oxidation tests, we conclude that heating the rods in a hydrogen atmosphere at 1400-1650°C for 6 to 9 min causes less cladding damage due to hydriding than heating in a steam atmosphere would cause due to oxidation. It also should be noted that, before Run H4, the rod was preoxidized at 1100°C for 7 min in steam flowing at 2 g/min; thus, as shown by Runs H2 and H4, the presence of steam in hydrogen or preoxidation of the rod greatly reduces the hydriding effects. Therefore, in the loss-of-coolant accident, oxidation of cladding by steam is considered to be the dominant factor in cladding failure, and any destructive effects by hydriding would result only after significant oxidation had already occurred.

2. Pressure Generation due to Particle-Water Energy Transfer (R. O. Ivins)

a. Pressure-pulse Column Study--Molten Particles and Hot Spheres

Last Reported: ANL-7403, pp. 156-163 (Dec 1967).

To analyze adequately the consequences of an accident in a water-cooled thermal reactor in which hot fuel materials might be injected and dispersed into the water coolant, knowledge is needed of the manner in which large amounts of energy are transferred from these particles to the liquid coolant; such a process could occur in either an excursion or a loss-of-coolant accident and could result in an explosive generation of steam.

Previous experiments have measured transient heat transfer from hot spheres to water. Results of experiments to measure pressure pulses and forces generated due to heat transfer from hot materials dropped into a water column are reported here.

The apparatus used for the experiments consisted of a vertical glass cylinder filled with distilled water heated by an electrical-tape heater that maintained the water at temperatures from 30°C to boiling. A piezoelectric-crystal transducer in the bottom of the tube sensed dynamic pressure pulses; the signal was displayed on an oscilloscope and was recorded photographically. An electrically heated furnace, mounted directly above the water column, heated the spheres and molten metals before they were dropped into the water. In some cases, the entire water column was supported by the transducer for reaction-force measurements in which a hot 1/4-in.-dia platinum sphere was dropped into the water (see ANL-7403).

In the current experiments, hot 1/2-in.-dia silver and stainless steel (Type 304) spheres, attached to 1/8-in.-dia sheathed thermocouples,

and quantities of ~1-40 g of molten bismuth have been dropped into water at various temperatures in columns of several different diameters. Screen analyses of the bismuth residue were made.

The theoretical model presented previously indicated that the dynamic pressure pulses developed due to the formation or collapse of vapor bubbles beneath the surface of a noncompressible liquid would be proportional to the density of liquid, the depth of the bubbles, and the second derivative of the bubble volume with respect to time, and inversely proportional to the cross-sectional area of the liquid column.

To verify the variation of dynamic pressures with bubble depth and column cross section, a 0.5-in.-dia stainless-steel sphere, which was attached to a 1/8-in.-dia thermocouple and initially at 500°C, was rapidly positioned at depths of 3 and 5 in. in a 3.06-in.-dia water column, and at depths of 3.5 and 7.5 in. in a 1.84-in.-dia water column. The results showed that maximum dynamic pressures occurred at the transition from quiet film to violent boiling (greatest values of d^2V_i/dt^2), and that these maximum pressures were approximately proportional to the water depth (at the transition to violent boiling) and inversely proportional to the cross-sectional area of the water column, as predicted by the simple theory.

The temperatures at which the transition from quiet film to violent boiling occurred were determined for 0.5-in. silver spheres (initially at 555°C) and at several water temperatures. The transition was observed visually and also noted as a change in slope of the cooling curve. In these tests, the hot spheres were rapidly submerged into the water and held stationary until the completion of observation. In other tests, the initial temperature of the sphere was varied and whether or not film boiling occurred immediately upon dropping the sphere into water was noted. The principal difference between the two tests was that, in the second case, the sphere was in motion during the observation, and the effect of this motion on the transition was ascertained. The results are shown in Fig. IV.C.1. It was observed that the onset of violent boiling occurs at slightly higher temperatures for moving spheres than for stationary spheres.

The results of dropping ~10-g quantities of molten bismuth at 500°C into a 3.06-in.-dia column from a height of 8.5 in. above the water surface are shown in Fig. IV.C.2. It should be noted that in the case of dropping molten bismuth into the water it is not possible to suspend the bismuth at a predetermined depth as was done with the solid sphere attached to a thermocouple. At the transition from quiet film boiling to violent boiling, the molten bismuth usually broke into fine particles, which caused a dynamic pressure pulse. This transition occurred at greater depths for warmer water; in water near the boiling point, the transition actually may not occur

at all before the bismuth has solidified. As shown in Fig. IV.C.2, the maximum pressure pulses were observed at water temperatures between 70 and 80°C. The greatest breakup of the molten bismuth into fine particles occurred under conditions that resulted in the generation of the largest pressure pulses.

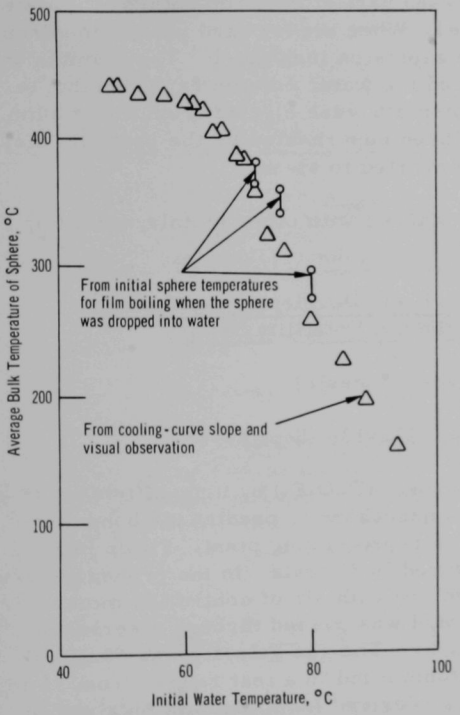

Fig. IV.C.1. Average Bulk Temperature of 0.5-in. Silver Sphere in Water at Transition from Quiet Film to Violent Boiling

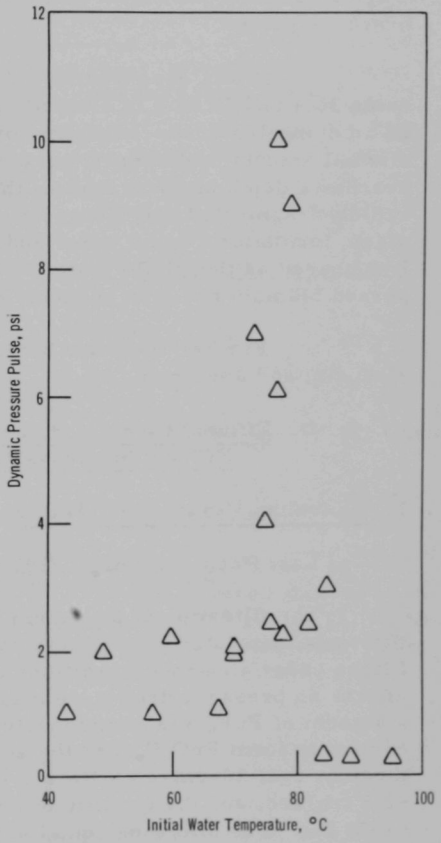

Fig. IV.C.2. Maximum Dynamic Pressure Pulses due to Dropping 10 g Molten Bismuth at 500°C from 8.5 in. above the Surface of the Water into a 3.06-in.-dia Water Column

The effect of the quantity of molten bismuth on dynamic pressure generation was observed in a series of four tests in which bismuth at 500°C was dropped from a height of 6 in. into water at 60°C. The weights of bismuth for the four tests were 8.48, 11.80, 20.72, and 32.98 g, and the dynamic pressures were 22, 20, 32, and 60 psi, respectively. When ~3 g or more of

molten bismuth at ~500°C were dropped into water in the vicinity of 75°C, mild explosions occurred and the bismuth rapidly fragmented. The explosions became more violent as the quantity of bismuth was increased. With about 20 to 30 g of bismuth, water was ejected from the column by the explosion and dynamic pressures of 40 to 60 psi were generated. Greatest fragmentation of the metal into fine particles is associated with the largest pressure pulses.

It was observed, from high-speed motion pictures of two tests using 36.4 and 39.98 g of bismuth, that the liquid bismuth entered the water as an elongated drop. When the forward part of the drop entered the water, a small amount of dispersal occurred. When the forward part of the drop reached a depth of about 3.5 in., the explosion took place. The bismuth was rapidly fragmented and dispersed, and the water column expanded due to steam formation. Some water and bismuth were ejected from the column. It appeared as though the water had been superheated by the partially dispersed bismuth and then suddenly converted to steam.

Further tests are being planned with other metals, including zinc, tin, and aluminum.

D. Effluent Control--Research and Development--Gaseous Effluent Studies--Plutonium Volatility Safety

1. Plutonium Hexafluoride Safety (R. W. Kessie)

Last Reported: ANL-7500, pp. 135-136 (Sept 1968).

The filtration of plutonium aerosol (PuO_2F_2) by high-efficiency fiber filters is being studied to obtain data necessary to predict the behavior of filters under abnormal conditions in a reprocessing plant. Filter loading effects on pressure drop were measured in 21 tests. In the procedure used, a stream of PuF_6 was continuously mixed with air of controlled moisture content to form PuO_2F_2, and the aerosol was passed through a series of three or four 10-cm-dia filters for 1 hr. The gas velocity was ~0.25 or ~2.5 cm/sec, and the quantity of plutonium fed in a test ranged from ~1 to ~1950 mg. The following equation was derived from the data obtained in the small-scale experiments:

$$S = 2.93 \times 10^{-6} u^{1.58} F^{1.49}, \qquad (1)$$

where S is the slope of the pressure drop-vs-time curves (in. H_2O/min), u is the air velocity incident to the surface of the filter (cm/sec), and F is the PuF_6 feed rate (mg Pu/hr).

Equation (1) was scaled up to allow estimation of the pressure drop for a 1000-cfm-rated filter at various gas velocities and filter loadings

(based on PuF_6 released from a containment vessel). These estimates are given in Table IV.D.1. For conditions similar to those used in these experiments, the confidence limits for pressure drop are within a factor of 2 of the stated values.

TABLE IV.D.1. Estimated Filter Loading Capacity
(Filter Size: 1000-cfm-rated Air Flow)

Increase in Pressure Drop (in. H_2O)	PuF_6 Release (kg Pu) That Gives Indicated Increases in Pressure Drop at Indicated % of Rated Air Flow			
	10% Air Flow	20% Air Flow	50% Air Flow	100% Air Flow
1	3.4	1.6	0.62	0.29
2	5.4	2.6	0.98	0.47
4	8.6	4.1	1.6	0.75

E. Engineered Safety Features

1. Safety Features Technology--Containment

a. Hydrodynamic Response to High-energy Excursion (Y. W. Chang and G. Cinelli, Jr.)

Last Reported: ANL-7500, pp. 136-138 (Sept 1968).

(i) Selection of Equations of State of Materials. The two-dimensional hydrodynamic analysis and computer code were extended to include the plenum and the breeding blanket surrounding the core. The blankets can be either in vaporized state or in their pre-excursion state. The equation of state of the blankets in the vaporized state is assumed to have the form

$$P = B \exp\left(-\frac{A}{E+E_0}\right),$$

where P is the pressure, E is the internal energy, and A, B, and E_0 are constants. The equation of state of the blankets in their pre-excursion state and that of plenum are the Mie-Gruneisen-type equation of state

$$P = P_H + \frac{\gamma}{V}(E - E_H),$$

where P_H and E_H are the pressure and internal energy along the Hugoniot curve, γ is the Gruneisen ratio, and V is the specific volume. The Hugoniot (P_H - V) curve of the blankets is constructed according to the method described in ANL-7500. The Hugoniot curve for the plenum is constructed according to

$$P_H(V, V_{00}) = \left[1 + \frac{1 - \frac{V_0}{V_{00}}}{\frac{V}{V_{00}}\left(\frac{2}{\gamma} + 1\right) - 1} \right] P_H(V, V_0),$$

where V_{00} is the initial specific volume of the plenum including the fission gas, V_0 is the initial specific volume of the solid plenum (without the fission gas and voids), and $P_H(V, V_0)$ is the Hugoniot curve of the solid plenum. As a first approximation, fission gas is treated as internal voids. A sample problem is being run on the computer to study the effects of the blankets and plenum on the propagation of shock waves emanating from the core.

b. Inelastic Response to High-energy Excursion (G. Cinelli, Jr.)

Last Reported: ANL-7500, pp. 138-139 (Sept 1968).

(i) Analysis of Shock-wave Propagation. The analysis of shock-wave propagation has been completed. The next step in the process is to derive a rezoning technique that will enable computing to longer times.

(ii) Programming Finite-difference Equations in Fortran. The programming of the finite-difference equations has been completed. Good results obtained on a sample problem indicate that the program is working satisfactorily. The results of the calculations are being set up to produce pictorial results.

(iii) Select Multiaxial Equations of State. Work is continuing on the selection of the best multiaxial equation of state. There seems to be no discernible way of selecting between a number of results except by experiment. Thus consideration is being given to devising experiments.